DEVELOPMENT OF A FDTD SIMULATION OF IONOSPHERE PROPAGATION FOR EARTHQUAKE PRECURSOR OVER THE SUMATERA-MALAYSIA REGION

by

SITI HARWANI MD YUSOFF

Thesis submitted in fulfilment of the requirements for the degree of Doctor of Philosophy

September 2018

ACKNOWLEDGEMENT

First and foremost, praises and thanks to the God, the Almighty, for His showers of blessings throughout my research work to complete the research successfully.

I would like to express my deep and sincere gratitude to my research supervisor, Assoc. Prof. Dr. Yoon Tiem Leong, for giving me the opportunity to do research and providing invaluable guidance throughout this research. His dynamism, vision, sincerity, and motivation have deeply inspired me. It was a great privilege and honour to work and study under his guidance. I would like to say thank you for my co-supervisor, Assoc. Prof Dr. Lim Hwee San for his advice and support throughout this research work.

I am extremely grateful to my husband, Mohd Ikhwan, who has helped to ease some of the burdens and pressures of the Ph.D. Without his love and continuing support, I would not able to complete my Ph.D. journey. He has always been there to offer reassurance during the difficult times and to celebrate my successes. I appreciate the sacrifices he has made so I could attain this degree. Also, I express my thanks to my 3 adorable children, the reason why I am not giving up in the middle of the journey. I would like to thank my parent, mother-in-law, and my siblings for their prayers and borderless love.

I am extending my acknowledgment to my colleagues and staff in School of Aerospace Engineering, Universiti Sains Malaysia for all the support. Special thanks to Dr. Norilmi Amilia and Dr. Aslina, for their support and valuable advices during my ups and downs, my Dean, Prof Ir. Dr. Mohd Zulkifly Abdullah, and my Program Chairman, Ir. Dr. Nurulasikin for their understanding.

Finally, my thanks go to all the people who have supported me to complete the research work directly or indirectly. For those who answer the call for help in the middle of the day and night, near and from far, with no expectation of personal gain. This thesis would not have been possible without them.

I would like to acknowledge the Ministry of Higher Education (MOHE) and Universiti Sains Malaysia for granted scholarship under the Academic Staff Higher Education Scheme (ASHES).

TABLE OF CONTENTS

LIST OF TABLES

LIST OF FIGURES

LIST OF SYMBOLS

Ap index	Planetary A-index
B	Magnetic Flux Density
B_0	Earth's natural magnetic field
c_0	Speed of light
C_{ax}, C_{bx}	Coefficients for electric field
D_{ax}, D_{bx}	Coefficients for magnetic field in x-direction
D_{ay}, D_{by}	Coefficients for magnetic field in y-direction
Dst index	Disturbance Storm Time index
E	Electric Field
E_0	E_z component at source
E_{ref}	Values of E_z measured in the reference domain
$E_{ref,max}$	Maximum values of E_z measured in the reference domain
E_z	Electric Field in z-direction
f_0	Frequency
foF2	Critical frequency of the F2 layer of the ionosphere
h	Height
H	Magnetic Field
H_x	Magnetic Field in x-direction
H_y	Magnetic Field in y-direction
h	User-defined rate of growth
i,j	Temporal and spatial discretization
J	Electric Current Density
J_z	Electric Current Density in z-direction
k	Spatial index
Kp index	Planetary K-index

m	Particle Mass
m_e	Electron mass
n	time step
N	Positive real or positive integer of n
N_e	Electron Density
N_{PML}	PML thickness
q	Particle Charge
R_0	Reflection coefficient
t	Temporal Variable
ϑ	Velocity
β	User-defined difference in the exponent rates
Δ	Spatial width
δk	Thickness of the PML in the grid index by
ΔQ	Root Mean Square of Ez
Δx	Spatial width in x-direction
Δy	Spatial width in y-direction
ε_0	Permittivity of free space
ε_{max}	User-defined parameter to control the rate of evanescent mode attenuation
μ_0	Permeability of free space
ν	Electron Collision Frequency
ρ_k	Depth in PML
σ, σ^*	Conductivity
ω_b	Gyro Frequency or Cyclotron Frequency
ω_p	Plasma Frequency
ω_r	Angular Conductivity

LIST OF ABBREVIATIONS

2D	2-Dimensional
ABC	Absorbing Boundary Condition
ADE	Auxiliary Differential Equation
AGW	Acoustic Gravity Wave
CHAMP	Challenging Minisatellite Payload
CFL	Courant-Friedrich-Lewis
COSPAR	Committee of Space Research
EEJ	Equatorial Electrojet
EIA	Equatorial Ionization Anomaly
ELF	Extreme Low Frequency
EM	Electromagnetic
FDTD	Finite Difference Time Domain
GPS	Global Positioning System
GPS-MET	Global Positioning System/Meteorology
GPS-TEC	Global Positioning System - Total Electron Content
GRACE	Gravity Recovery and Climate Experiment
HF	High Frequency
IAGA	International Association of Geomagnetism and Aeronomy
IGRF	International Geomagnetic Reference Field
IRI	International Reference Ionosphere
ISDC	Information System and Data Centre
LEO	Low Earth Orbit

PLCDRC	Piecewise Linear Current Density Recursive Convolution
PML	Perfectly Matched Layer
RAM	Random Access Memory
RC	Recursive Convolution
RO	Radio Occultation
SAC-C	Satellite de Aplicaciones Cientificas-C
S-FDTD	Stochastic Finite Difference Time Domain
TEC	Total Electron Content
TM	Transverse Magnetic
ULF	Ultra Low Frequency
URSI	International Union of Radio Science
UTC	Coordinated Universal Time
VLF	Very Low Frequency
VLF-LF	Very Low Frequency-Low Frequency

PEMBANGUNAN SIMULASI FDTD BAGI PERAMBATAN IONOSFERA UNTUK PREKUSOR GEMPA BUMI DI RANTAU SUMATERA-MALAYSIA

ABSTRAK

Gangguan di dalam medan eletrik menegak di ionosfera sebelum berlakunya gempa bumi yang besar sangat kurang dikaji. Maklumat medan eletrik menegak yang diperolehi daripada gelombang eletromagnetik (EM) yang merambat melalui ionosfera boleh diaplikasikan untuk membina prekusor gempa bumi. Kajian ini dijalankan melalui pembangunan kod 2D Perbezaan Terhad Domain Masa (FDTD) untuk simulasikan perambatan EM di dalam ionosfera yang anisotropic. Untuk meniru keadaan ionosfera yang anisotropik dan menyebar, profil ketumpatan elektron (N_e) yang dikutip daripada satelit CHAMP digunapakai di dalam kod sebagai parameter untuk medium. Data yang digunakan di dalam kod ini adalah 5 hari sebelum berlakunya gempa bumi Lautan Andaman di Aceh pada 26 Disember 2004. Lapisan Padan Sempurna (PML) sebagai sempadan penyerapan digunakan di dalam kod ini untuk memastikan gelombang yang memantul daripada sempadan adalah minimum. Berdasarkan data yang dihasilkan daripada simulasi FDTD ini, satu protocol untuk prekusor gempabumi, dikenali sebagai ΔQ dibina. Keputusannya, gangguan di dalam profil ketumpatan electron dikesan 3 hari sebelum berlakunya gempa bumi besar, ditunjukkan melalui nilai N_e yang tinggi di dalam profil. Sebagai tambahan, ada 1 hari sebelum kejadian gempa bumi menunjukkan profil yang terganggu. Medan elektrik menegak daripada perambatan electromagnet menggunakan kaedah FDTD dibangunkan dan menunjukkan tahap kepekaan yang tinggi terhadap perubahan medium di ionosfera. Kejituan PML juga diukur melalui

pengiraan ralat relative. Keputusan menunjukkan 25 sel untuk PML boleh menahan pantulan gelombang 48% lebih baik dari 5 sel untuk PML. Kemudian, kerana kekurangan data N_e, tiada kesimpulan ramalan yang boleh dilakarkan daripada pengiraan ΔQ. Walaubagaimanapun, ciri-ciri daripada plot ΔQ memberi petanda satu puncak ditunjukkan sebelum berlakunya gempa bumi. Kesimpulannya, secara teknikalnya kita berupaya untuk mengunapakai parameter ionosfera ke dalam komputasi electromagnet sebagai cubaan untuk menghasilkan prekusor gempa bumi.

DEVELOPMENT OF A FDTD SIMULATION OF IONOSPHERE PROPAGATION FOR EARTHQUAKE PRECURSOR OVER THE SUMATERA-MALAYSIA REGION

ABSTRACT

The perturbation on the vertical electric field in the ionosphere before large the large earthquake is a poorly investigated problem. The information obtaining from the electromagnetic (EM) wave propagated through the ionosphere can be applied to construct an earthquake precursor. This study conducted through the development of a home-grown 2D Finite Difference Time Domain (FDTD) code to simulate the EM propagation in the anisotropic ionosphere. To imitate the anisotropic and dispersive condition of the ionosphere, the electron density (N_e) profile collected from the CHAMP satellite is applied in the code as the medium parameter. The data used in this code is from 5 days before Aceh 2004 Andaman Sea earthquake, occurred on 26th December 2004. Perfectly Matched Layer (PML) as an absorbing boundary condition is implemented in the code to ensure minimum wave reflected from the boundary of the computational grid. Based on data generated from the FDTD simulation, a protocol for an earthquake precursor, known as ΔQ is constructed. As results, some perturbations in electron density profile are observed 3 days before the large earthquake occurred, shown in the high value of N_e in the profile. In addition, a day shows a distorted profile. The vertical electric field from EM propagation using FDTD simulation is developed and shows good sensitiveness to the change of the medium in the ionosphere. The PML efficiency is measured through the relative error calculation. The results show 25 cells of PML can suppress

the reflective wave 48% better than 5 cells of PML. Due to the lack of data on N_e, no conclusive prediction can be drawn from the measurement of ΔQ. However, the feature of ΔQ plot alone hinted a peak before at the occurrence of the earthquake. As a conclusion, it is technically viable to couple ionospheric parameter into the computational electromagnetic simulation as an attempt to develop an earthquake precursor.

CHAPTER 1

INTRODUCTION

1.1 Overview

Earthquake is a phenomenon where the tectonic plate of Earth moves either horizontally or vertically due to the activity of Earth's crust or volcanic activity and release sudden energy known as seismic waves. This incident called seismic event, and when the tectonic plates move, the Earth's surface is shaking and cause ground displacement. The earthquake magnitude can be measured using a seismometer, and the unit is on the Richter scale. Large earthquakes with more than 7 Richter magnitude scale potentially cause damages of buildings, injury or loss of life, landslides, fires and some studies show earthquake with 7 and more magnitude that occurred on the seabed, the movement of the seabed can produce sudden movement of large volumes of water called the tsunami.

In past 20 years, the earthquake event with magnitude 6 and more occurred in average 30 events per year as shown in Figure 1.1, prompting good motivation to conduct a research on modelling earthquake precursors. One of the approaches is via computational modelling of electromagnetic wave signal propagating in the ionosphere.

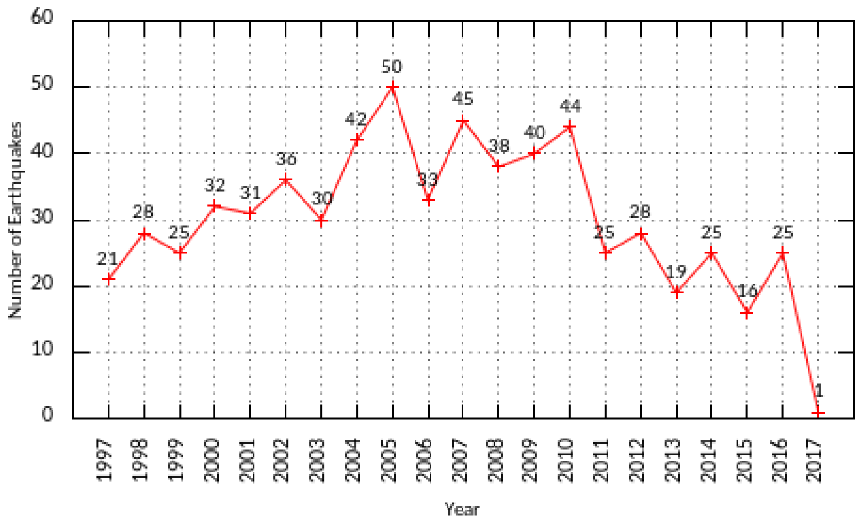

Figure 1.1 The earthquake with magnitude 6 and more occurred in South East Asia from 1997 until 2017

(Page URL: https://earthquake.usgs.gov/earthquakes/search/ , downloaded on 31st Jan 2018)

The idea of seismo-ionospheric coupling is to study the connection between ionospheric perturbation and seismic activity during earthquake preparation process. This study is multidisciplinary and needs a wide range of knowledge in very specific disciplines, covering areas ranging from Earth plate tectonics deep down to Earth's magnetosphere high up.

Referring to Figure 1.2, the epicentre areas in the Andaman Sea focuses on the northern region of Sumatra. It demonstrates how easily this plate can be ruptured. Before 2004, the seismologist community did not positively anticipate the region to be hit by a massive earthquake of such a scale. This event is chosen as our case study since it left major impacts on the socio-economy of Malaysia.

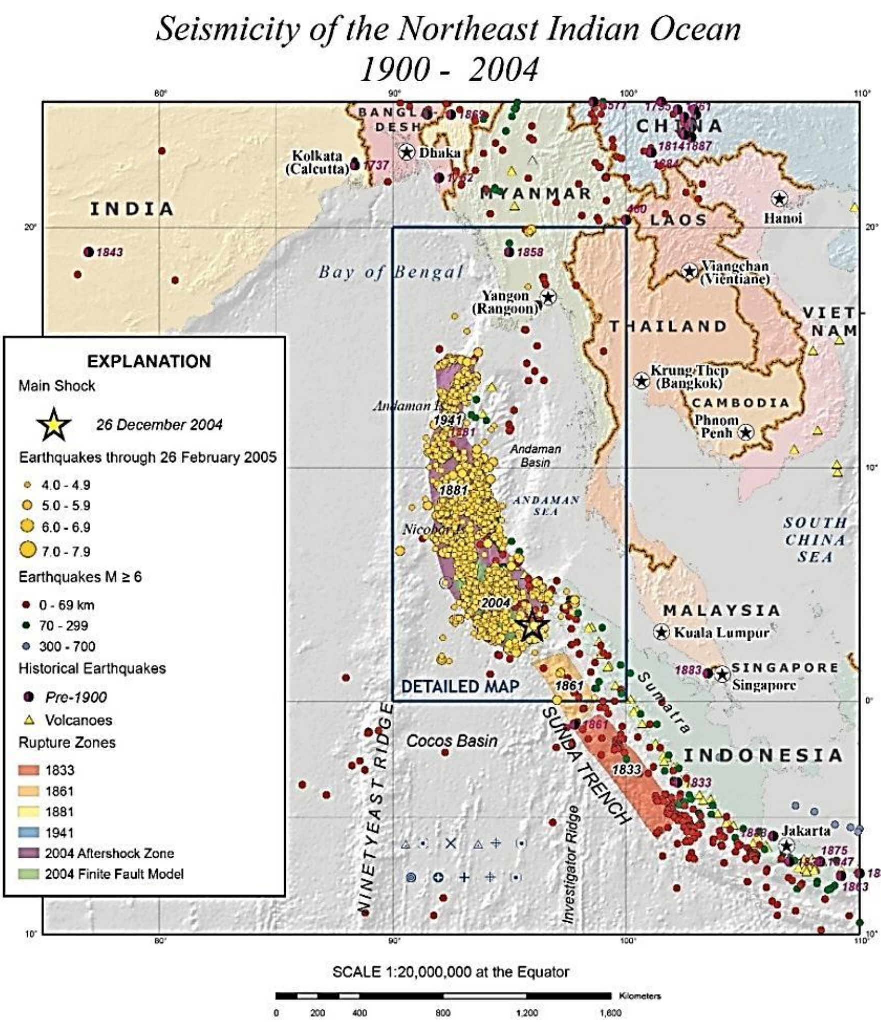

Figure 1.2 The location of the earthquake epicentre in the Sumatera region.

(Page URL: http://earthquake.usgs.gov/earthquakes/eqarchives/poster/2004/20041226.php ,

downloaded at 4th Dec 2016)

1.2 Ionospheric Physics

The ionosphere in the Earth-atmosphere system is thE-layer where ionized particle dense in a region between 90 km to 120 km. From a modelling point of view, this layer can be considered as an atmospheric electro-magnetic system consists of ion, proton, and electron comprises of low plasma density, in which electrodynamics processes involving charged particles interactions are dynamically happening. Studies in the literature show that the equatorial and low-latitude ionosphere has high plasma density which is sensitive to electric field perturbation. For example, Fang, Xi, Wu, Liu, and Pu (2016) proposed that electric field and neutral wind can be the essential factors that contribute to the equatorial and low-latitude ionospheric dynamics.

Previous studies investigating the sources of ionospheric disturbances due to seismic activity conclude that two main mechanisms cause the disturbance: 1) electromechanical and 2) acoustic wave. Data from both ground-borne and space-borne observations can be used to investigate the electrodynamics activities in the ionosphere before, during and after strong seismic activities. A recent work discovered that acoustic gravity waves that were generated by strong seismic activity propagate actively in the dynamo region (Oyama et al., 2016). On the other hand, ionospheric disturbances can be caused by solar flares, lightning, and geomagnetic storm. To ensure that the source of disturbance is caused by seismic activity merely, the data collection should be conducted during low solar activity and low geomagnetic storm activity (Ondoh, 2009).

1.3 The Electromagnetic Signal

The electromagnetic (EM) waves that propagate from the surface of the Earth vertically to the ionosphere are known as Earth-ionosphere waveguide. The composition of ionosphere plays a major role when modelling the propagation of electromagnetic waves as earthquake precursor. The numerical pattern of electromagnetic signal propagating through the ionosphere by Extreme Low Frequency (ELF, 3 Hz to 30 Hz), Ultra Low Frequency (ULF, 300 Hz to 3000 Hz) and Very Low Frequency (VLF, 3 kHz to 30 kHz) radio waves can serve as a probe for abstracting the relationship between ionosphere and seismic activity. Radioactive gases, for example, radon, emanating from strong earthquake preparation zone and ionization in the air become significant, hence increasing electron number density and electric conductivity to generate anomaly to the ionosphere. The dynamical behaviour of an electromagnetic wave propagating in the ionosphere is completely governed by Maxwell's equations. To completely solve Maxwell's equations for this system can be a daunting numerical task. The details of numerical modelling vary greatly depending on the specifics of a numerical scheme and the kind of model adopted.

Electromagnetic phenomena observed prior to and during seismic activity due to the strengthening of the electric field in the ionosphere and have been reported by Sorokin, Yashchenko, and Hayakawa (2007). The modelling of electromagnetic wave propagation to investigate the possibility of earthquake precursor associated with ionospheric disturbance may verify the disturbance observed by the ground station and satellite sensor that occurred before the large earthquake.

There have been several missions launched into orbit using VLF to monitor earthquake as well as the ground-based station (Ho, Jhuang, Su, & Liu, 2013; Ono et al., 2012). These are useful apparatus that can be exploited to investigate, observe and monitor earthquake activity for the precursor. Satellite data on South East Asia region can be used as raw data to model earthquake precursor computationally.

1.4 FDTD Modelling

There are many approaches and techniques to model and simulate vertical electric field in the ionosphere, e.g., waveguide mode theory, frequency-domain mode theory and Finite Different Time Domain (FDTD) method. FDTD is a reliable and robust method that can be applied in a wide area of physical systems, covering from nano-technology to planetary environment modelling. FDTD method is capable of solving large, complicated physical problems, provided sufficient computational sources, both regarding time and hardware, and is available. The computational resources issues become less pressing with the availability of powerful computers, large data storage and a large amount of Random Access Memory (RAM). The theoretical fundamental of the FDTD method is solidly established and can be easily understood. All these considerations make FDTD a very popular tool for simulating electro dynamical systems.

Common techniques used in ground-based and space-borne observations only provide short-term and discontinuous monitoring of the lower ionosphere and often impractical to implement in many regions of the world. To date, there is no model of simulation of the vertical electric field to study electromagnetic waves propagation via FDTD over Sumatera-Malaysia region. In this thesis, FDTD has been chosen as a technique to model propagation of vertical electric field in the ionosphere with the anomaly in electron density profile that is believed to occur before some large earthquake.

In this study, Sumatra-Andaman Island earthquake that occurred on 26th December 2004 is chosen for our case study simulation of electromagnetic wave propagation in the ionosphere above Aceh, Sumatera and Peninsular Malaysia. The idea is to simulate electromagnetic wave propagation from a VLF source on the ground through the ionosphere up to a vertical height of 120 km. The EM wave moving through its propagation course will undergo interactions with the atmospheric medium, and be detected at various sites on the ground separated at distances within 600 km. Figure 1.3 shows the relationship between pre-earthquake activity on the ground and appearance of disturbance in the lower part of the ionosphere and the electromagnetic wave propagation. A most definite aspect of this disturbance is caused by deviations in ionospheric parameters.

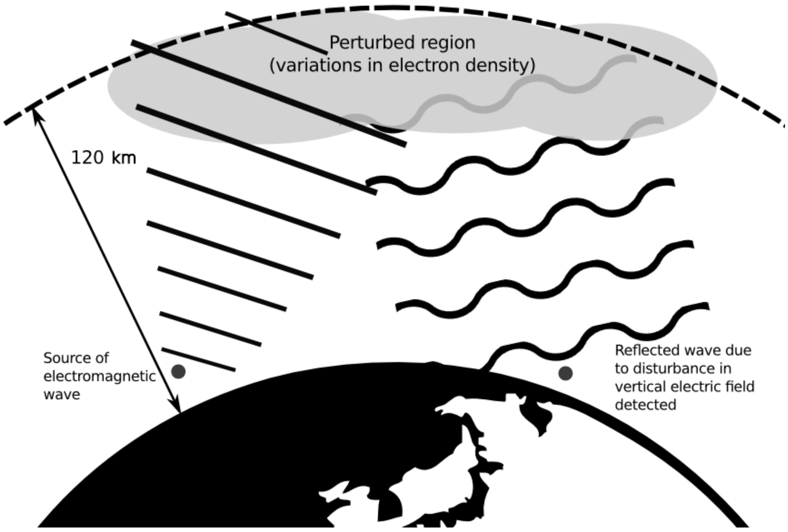

Fig 1.3 The electromagnetic wave propagation from a ground source through the atmosphere up to a height of 120 km where the ionosphere resides.

1.5 Research Questions

This thesis aims to model electromagnetic wave propagation in the ionosphere to study the vertical electric field behaviour under seismically perturbed conditions. Researches on the earthquake, though a common endeavour in many parts of the world, is not common in Malaysia owing to the fact that earthquake rarely occurs in this part of the world. In addition, relevant data is limited. Development of models to study electromagnetic wave propagation in ionosphere for earthquake precursor over the Malaysia-Sumatera region in particularly not only has practical relevance but itself a novel research topic in the Malaysian context.

The research is conducted to answer the following questions:

1. Can the perturbation in the electromagnetic signals in the Earth-ionosphere waveguide caused by a large earthquake be effectively simulated via computational means coupled with measured data?
2. Can the computational simulation serve as an effective earthquake precursor?

This thesis revolves the main theme of developing a two dimensional finite difference time domain (2D FDTD) computational model by solving the full Maxwell's equations for VLF band. In this study, simulation for the vertical electric field, before and during an earthquake will be performed. The main aim is to use the model to analyse the variations in the vertical electric field propagating in the background medium (atmosphere) which electron density various as a function of height. By feeding in empirical data on the height-varying electron density profile of the atmosphere, this approach allows us to investigate the ionosphere anomalies, in an *in-silico* manner, over the Malaysia-Sumatera region near to Aceh 2004's earthquake epicentre. The electron density profile is extracted from database of Challenging Minisatellite Payload (CHAMP) satellite.

1.6 Problem Statements

Human activity on the ground and conductive ionosphere of the Earth and gamma-ray from outer space influence the signal propagation from the ground. The observations of the vertical electric field, E_z at the Earth's surface within an earthquake epicentre zone under quiet and perturbed conditions have been conducted significantly (Bhattacharya, Sarkar, Gwal, & Parrot, 2009; Błeçki, Parrot, & Wronowski, 2010; Itoh, Ando, & Hayakawa, 2013; Naidu, Latha, Rao, & Devi, 2017) . The physical mechanism of such perturbations on the vertical electric field, E_z prior to the earthquakes is a poorly investigated problem. Seismic waves can be detected in the Earth's atmosphere and ionosphere; however, the mechanism of how seismic waves modified the ionosphere in the dynamo region is still an unresolved issue that has no general consensus. Obtaining an earthquake precursor has an obvious practical appeal but is pragmatically yet an unachieved goal. In particularly, to obtain an earthquake precursor based on electromagnetic information in the ionosphere is a viable approach many have tried but more research into this area is still required. Numerical and computational study using 2D FDTD model of ionospheric anomalies to simulate vertical electric field around earthquake epicentres have been performed in many parts of the world. However, for Malaysia-Sumatera region, there is hardly any. Malaysia-Sumatera is a seismically active region known as 'Pacific Ring of Fire'. Modelling earth-quark-induced electromagnetic anomaly in the atmosphere of this region is hence warranted.

In addition, depending on the environment (a.k.a. medium) of a particular system to investigate, the complexity of the FDTD code varies tremendously. For example, it is relatively simple to develop a 2D FDTD numerical code for linear, isotropic, non-dispersive medium in a rectangular coordinate system with space-varying medium characteristics. However, for an anisotropic, dispersive medium such as ionosphere, the numerical algorithm to achieve a robust output based on the spirit of FDTD can be non-trivial due to the inherent numerical complexity of Maxwell's equations in such a medium. The variation in the physical properties of the ionospheric as a function of altitude is also a source that compounds the numerical complexity of the problem.

1.7 Research Objectives

This research is aimed to achieve the following objectives:

1) To identify the variation in the atmospheric electron density profile near the epicentre region in South East Asia during the 2004 Sumatra earthquake using CHAMP satellite data.
2) To develop a home-grown 2D FDTD algorithm and an absorbing boundary condition for the propagation of EM wave in the anisotropic and inhomogeneous ionosphere.
3) To apply the 2D FDTD algorithm of electromagnetic wave propagation in the ionosphere that extends to an altitude of 120 km from the Earth's surface and a total horizontal distance of 600 km to construct a protocol for earthquake precursor.

1.8 Scope of Study

The 2D DFTD simulations performed in this thesis are limited to model only the ionosphere conditions during the quiet and perturbed time for the South East Asia region during the 2004 Sumatra earthquake. Data on the electron density profile of the atmosphere taken by a satellite operated during the earthquake time span will be applied. The simulation grid will cover from the ground up to the lower E-layer of the ionosphere (90 – 120 km). In the FDTD simulations, the wave source is an EM spherical wave of low-frequency, f = 30 kHz and wavelength λ = 10 000 m. The simulation region has a fixed space grid of size Δx = 1000 m, covering a total horizontal distance of 600 km and altitude of 120 km. The electron density, N_e data, as a variable parameter in FDTD codes, is the data from the CHAMP satellite. Perfectly Matched Layer (PML) is used to set up an absorbing boundary condition (ABC) at the boundaries of the computational grid.

The curvature of the Earth is assumed to have no influenced the sky wave propagation and hence neglected. This is a reasonable approximation as the radius of the Earth, $R_E = 6400$ km, is an order of magnitude larger than the largest length scale in the simulation. The computational grid is set as a flat, vertical, 2D plane. Rectangular (Cartesian) coordinate system is adopted. The area studied in this thesis is not easily investigated using ground-based data due to poor resolution and large error inflicting ground sensors. Rocket or sounding rocket experimental set-up provides data with a better accuracy but limited in temporal and geographical distribution. Hence the simulations done in this thesis shall not make use of the data taken from these sources.

1.9 Significance of the Study

Very strong earthquakes of magnitude above 7 Richter scale can destroy cities or densely populated areas. The damage could be very significant. The devastation of the building, loss of life and fires may lead to the loss as major as a nuclear explosion. In 26th December 2004, a large earthquake occurred near Aceh, Sumatera in epicentre 3.36˚N 95.85˚E at 00:58 UTC followed by a large tsunami and caused complete destruction of Aceh. It was reported that almost 230 000 are dead and more than 500 000 people are missing. The country nearby such as Malaysia, Thailand, Sri Lanka, India, Maldives and Somalia also affected by this earthquake. The study of the earthquake in Southeast Asia region as important as any study conduct all over the world because the earthquake and tsunami will give effect to Indonesia, Malaysia, Thailand, India and leave impacts to socio-economic to the country respectively.

In Malaysia, a study about the earthquake is still at infancy level because the earthquake is not a significant disaster as compared to flood. However, what happened in Kuala Muda, Kedah and Batu Ferringhi, Pulau Pinang during Aceh Earthquake on 2004 as well as the current event of the earthquake in Ranau, Sabah on 2015 should be a motivation to enhance research activities on the earthquake in Malaysia. It is very important and remarkable to study the earthquake activity in Sumatera-Malaysia region for the future to help and develop the human capacity to handle earthquake impact and to mitigate future earthquake as well as the tsunami. This study will give significant impact to the socio-economic well-being of the region. Recently there have been some researches on earthquake study in the Malaysia-Sumatera region. These are mostly research activities centred on data obtained from GPS-TEC and radiosonde station (Bagiya et al., 2017; Devi et al., 2018; A. M. Hasbi, Mohd Ali, & Misran, 2011; Alina Marie Hasbi et al., 2009; Shinagawa, Iyemori, Saito, & Maruyama, 2007; Tao et al., 2017) However, numerical and computational approaches of the ionospheric anomalies phenomena prior to earthquake over the south-east Asia region has been scarce if not totally absent.

The modelling of an electromagnetic anomaly in ionosphere before large earthquake using pure numerical technique can be a useful tool to predict the behaviour of earth magnetic and vertical electric field a few days or hours before the earthquake occurs. A computational approach to model localized region around the epicentre of the earthquake is relatively easy and cheap to implement. The results from this study can possibly lead to an improvement and advancement of research for earthquake precursor and disaster monitoring over the South-east Asia region, specifically.

1.10 Originality Contribution

This thesis presents novel contribution in the following areas:

1. FDTD simulation for electromagnetic propagation in ionosphere during the 2004 Sumatra earthquake using the electron density data recorded from the Challenging Minisatellite Payload (CHAMP) satellite during the seismic event.
2. Code development and implementation of current density, J and electric field, E (J-E) convolution technique to realise FDTD simulations and implementation of a working Perfectly Matched Layer (PML) algorithm in the FDTD code that is specifically tailored for the anisotropic condition found in the ionosphere with inhomogeneous parameters
3. Development of a protocol to construct an earthquake precursor based on FDTD simulations coupled with satellite data on atmospheric electron density profile.

1.11 Organization of Chapter

Chapter 1 of this thesis provides a concise introduction to this research. In addition, this chapter addresses the background, problem statements, research objectives and the significance of the study. Chapter 2 provide a literature review on the research-related works, such as seismo-ionospheric coupling, vertical electric field study and FDTD modelling of the ionosphere. Chapter 3 describes the methodology and the principles of the FDTD technique in detail. The techniques used to simulate the wave propagation through the ionospheric medium via FDTD are also elaborated. Data collection, measurement and processing for further analysis will also be detailed in this chapter. Chapter 4 consists of a discussion on the analysis of the electron density data in the South-East Asia region before, during and after the earthquake event. The data analysis from the satellite is presented, and results are discussed. Chapter 5 discusses resolve around the implementation of absorbing boundary condition (ABC) in the 2D FDTD code to propagate electromagnetic wave in the anisotropic ionosphere. The performance of the ABC implemented in the FTDT code is then analysed and accessed. Chapter 6 presents the results generated by the home-grown 2D FDTD code that models the EM propagation in the local Earth-ionosphere using satellite data obtained during the 2004 Sumatra earthquake period. The results of the simulations are then examined and analysed. Finally, the conclusion and suggestions for future work are presented in Chapter 7.

CHAPTER 2

LITERATURE REVIEW

2.1 Ionosphere and Ionospheric Disturbance

The ionosphere is a region where the highly ionized particle is developed as a result of the solar radiation ionized the particle within this region. This region has 3 main layers, which are D layer (50 – 90 km), E-layer (90 – 120 km) and F layer (120 – 300 km). ThesE-layers are divided according to the chemical composition, temperature and level of ionization of the region. The ionospheric disturbance is defined as any anomaly in the ionization level occurred in the ionosphere either in day or night, and detected using high frequency (HF) Doppler sounding, ground-based sensor and satellites.

Previous research have found that ionized particle, ion and electron profile in the ionosphere can be easily disturbed due to solar activities (Buresova, McKinnell, Lastovicka, & Boska, 2011; Guyer & Can, 2013; Sergeenko, Rogova, & Sazanov, 2009) and geomagnetic storm (Hamzah S.Z., 2018; Kumar & Parkinson, 2017; Laštovička, 1996; Polekh et al., 2017; Rees, 1995). However, a few other findings also suggest that despite low solar activity and minor geomagnetic storms, ionospheric disturbance can still be detected by ground-based sensors and satellites (Kherani, Lognonné, Kamath, Crespon, & Garcia, 2009; Kon, Nishihashi, & Hattori, 2011; J. Liu et al., 2010; Oyama et al., 2016; S. A. Pulinets & Legen'ka, 2003; Zakharenkova, Krankowski, & Shagimuratov, 2006)

In addition, in the equatorial and low latitude regions, the existence of Equatorial Ionization Anomaly (EIA), which is highly influenced by solar activity effects, can provide a more refined observation on the electron density in the ionosphere, from which disturbance due to seismic activity can be accessed (Pundhir, Singh, Singh, & Gupta, 2017). Atmospheric tides in E-layer moves ion, but electron remains in ionosphere because of their high gyro-frequency/collision frequency ratio. Thus makes electron fixed to magnetic and induced current. A polarization electric field is formed immediately to preserve the non-divergent flow of total electric current in agreement with Maxwell's equation. This event is known as E-layer dynamo region and then generates an electrically conductivE-layer (J. M. Forbes et al., 2008). Electrically conductive masses of air interact with Earth's magnetic field, producing intense current in the E-layer of the ionosphere (at the altitude of 85-120 km). This is known as equatorial electrojet (EEJ) (Jeffrey M. Forbes, 1981). The electric field in this region is generated day and night, moves perpendicular to the magnetic field, and produce $\vec{E} \times \vec{B}$ drift. A particle of charge q, mass m, and with velocity $\vec{\vartheta}$, moving in the presence of an external magnetic field, $\vec{B}$ and electric field, $\vec{E}$, experiences an electromotive force, via

$$m\frac{d\vec{\vartheta}}{dt} = q\vec{E} + q\left(\vec{\vartheta} \times \vec{B}\right). \tag{2.1}$$

In steady state motion, the time derivative of the velocity is small, and in Earth's magnetic field, the electric field $\vec{E}$ is perpendicular to both $\vec{\vartheta}$ and $\vec{B}$. Thus Eq. (2.1) is reduced to

$$\vec{\vartheta} = \frac{\vec{E} \times \vec{B}}{\left|\vec{B}\right|^2}. \tag{2.2}$$

By referring to (2.2), when the magnetic field is horizontal, the plasma moves in vertical and eastward ionospheric produced, this formation known as equatorial fountain effect (Wu, Liou, Shan, & Tseng, 2008). This effect is causing an anomaly on the ionospheric behaviour, known as Equatorial Ionization Anomaly (EIA). In the last few years, there has been a growing interest in the study to investigate the correlation between EIA in low-latitude ionosphere and seismo-ionospheric coupling for earthquake monitoring (Depueva, 2012; Devi, Medhi, Sarma, & Barbara, 2013; Devi et al., 2018; Klimenko, Klimenko, Zakharenkova, & Pulinets, 2012; Pundhir et al., 2017).

2.2 The Ionospheric Parameter

The main parameters that characterize the ionosphere are electron density, N_e $(\mathrm{electron/m^3})$ and the electron collision frequency, ν $(\mathrm{s^{-1}})$ (Nicolet, 1953). N_e is the electron concentration at a point in space, and is normally in the function of height, h, and electron collision frequency ν, which is the rate of collision between single charged particle and neutrally charged atmospheric molecules. The latter defines the conductivity profile in this layer, and is directly related to another parameter, the plasma frequency, ω_p (see Eq. 2.4). The plasma frequency is the natural frequency of plasma oscillation. In addition, the other main parameters are Earth's natural magnetic field B_0 $(\mathrm{Tesla, T})$ and the gyro-frequency, or cyclotron frequency, ω_b. The frequencies are in unit of Hertz, $\mathrm{s^{-1}}$(Wiesemann, 2014).

The conductivity profile of the ionosphere is a function of electron density and collision frequency. The conductivity parameter, ω_r is defined as

$$\omega_r = \frac{e^2 N_e(h)}{\varepsilon_0 m_e \nu(h)}, \tag{2.3}$$

Plasma frequency, ω_p is defined as

$$\omega_p = \sqrt{\frac{N_e(h)e^2}{m_e \varepsilon_0}}, \tag{2.4}$$

where e is electron charge, m_e is electron mass and ε_0 is permittivity of free space. ν describes the collision rate at which the ions and electrons collide among themselves in a weakly ionized plasma. Electromagnetic waves is related to electron's mass, it will be assumed that the ionosphere to be modelled, the ionic collisions will be neglected, and the collision frequency is contributed mainly by the electronic component (Carlson & Gordon, 1966; Titheridge, 1972). In this thesis, the theoretical model of the collision frequency in the ionosphere by Budden (1985), which assumes a dependence on the altitude via the following relation, is adopted:

$$\nu(h) = 1.816 \times 10^{11} \exp(-0.15\mathrm{h}), \tag{2.5}$$

where h is altitude in km and $\nu(h)$ is in unit of Hertz (s^{-1}). Meanwhile, theoretically, the electron density $N_e(h)$ is assuming the following form,

$$N_e(h) = 1.4276 \times 10^7 \exp[\beta(h - h') - 0.15h] \tag{2.6}$$

with β in unit of km^{-1} and h' in unit of km and $N_e(h)$ is in unit of cm^{-3}. The parameter h' control the altitude and β control the sharpness of the profile. During the nighttime Bickel, Ferguson, and Stanley (1970) discovered $h' = 85$ km and $\beta =$

$0.5\ \mathrm{km}^{-1}$gave a good agreement for the observation and Thomson (1993) found that for daytime observation, $h' = 70\ \mathrm{km}$ and $\beta = 0.3\ \mathrm{km}^{-1}$ is consistent for measurement.

The conductivity and plasma frequency are related via

$$\omega_r = \frac{\omega_p^2}{\nu(h)}. \tag{2.7}$$

In the anisotropic medium of the ionosphere, the cyclotron, or gyro-frequency, ω_b, is defined as the angular frequency of the circular motion of an electron. Free electron, ions and charged particles are attracted by the Earth's magnetic field, and they move in spiral lines along the magnetic field lines in certain velocity (Schunk & Nagy, 2009). The gyro-frequency determine by the following equation:

$$\omega_b = \frac{eB_0}{2\pi m_e}. \tag{2.8}$$

The data of Earth's natural magnetic field B_0 can be obtained from International Geomagnetic Reference Field (IGRF) (http://wdc.kugi.kyoto-u.ac.jp/igrf/point/index.html) provided by International Association of Geomagnetism and Aeronomy (IAGA). IGRF provides global Earth Magnetic Field model data for all locations on Earth. The natural magnetic field for this thesis is based on that located at 3.31° N, 95.85° E, the epicenter of the Sumatra 2004 earthquake.

By referring to the equation in Eq. (2.4), the plasma frequency ω_p depends only on the variable N_e, whereas the other parameter in the equation (e, m_e and ε_0)

are all constants. Thus, N_e will be the essential variable parameter for modeling electromagnetic wave propagation in the ionosphere. The acquirement and processing of electron density data will be explained in the following subsection.

2.3 Seismo-Ionospheric Coupling

The history of seismo-ionospheric coupling started in 1971 when Antselevich (1971) observed critical frequency of E-layer and its variation prior to the Tashkent 1966 earthquake. Large nuclear explosion, large volcanic eruption, earthquake with magnitude of 7.0 or larger, as well as rocket launcher are found to excite atmospheric waves that reach the ionospheric layers, leading to coupling between neutral atmosphere and ionized plasma that result in the variations in the electron density. For large earthquake, seismic movement of Earth plate generates acoustic and gravity oscillations that propagate upwards to the ionosphere, which disturbance can be detected up to 1000 km (S. Pulinets & Boyarchuk, 2004). Since then an extensive research effort has been devoted to the seismo-ionospheric coupling phenomena and related problems (Eftaxias et al., 2003; Golubkov, Golubkov, Ivanov, Bychkov, & Nikitin, 2010; Molchanov et al., 2004; S. Pulinets, 2004; Zhao, Zhang, Zhao, & Shen, 2014). Figure 2.1 suggests the processes involved in the physical mechanism of seismo-ionospheric coupling as proposed by S. Pulinets (2004). Figure 2.1 shows ionosphere disturbance originates from radioactive radon gases emanation released during an earthquake. Kelley (2009), Miklavčić et al. (2008) and (Ryu et al., 2016) found similar observation on anomalous radon concentration in soil and water near the active region of earthquake a few weeks or months before large earthquake. It was observed that the concentration level of radon was high, indicating some fault activities were occurring underground.

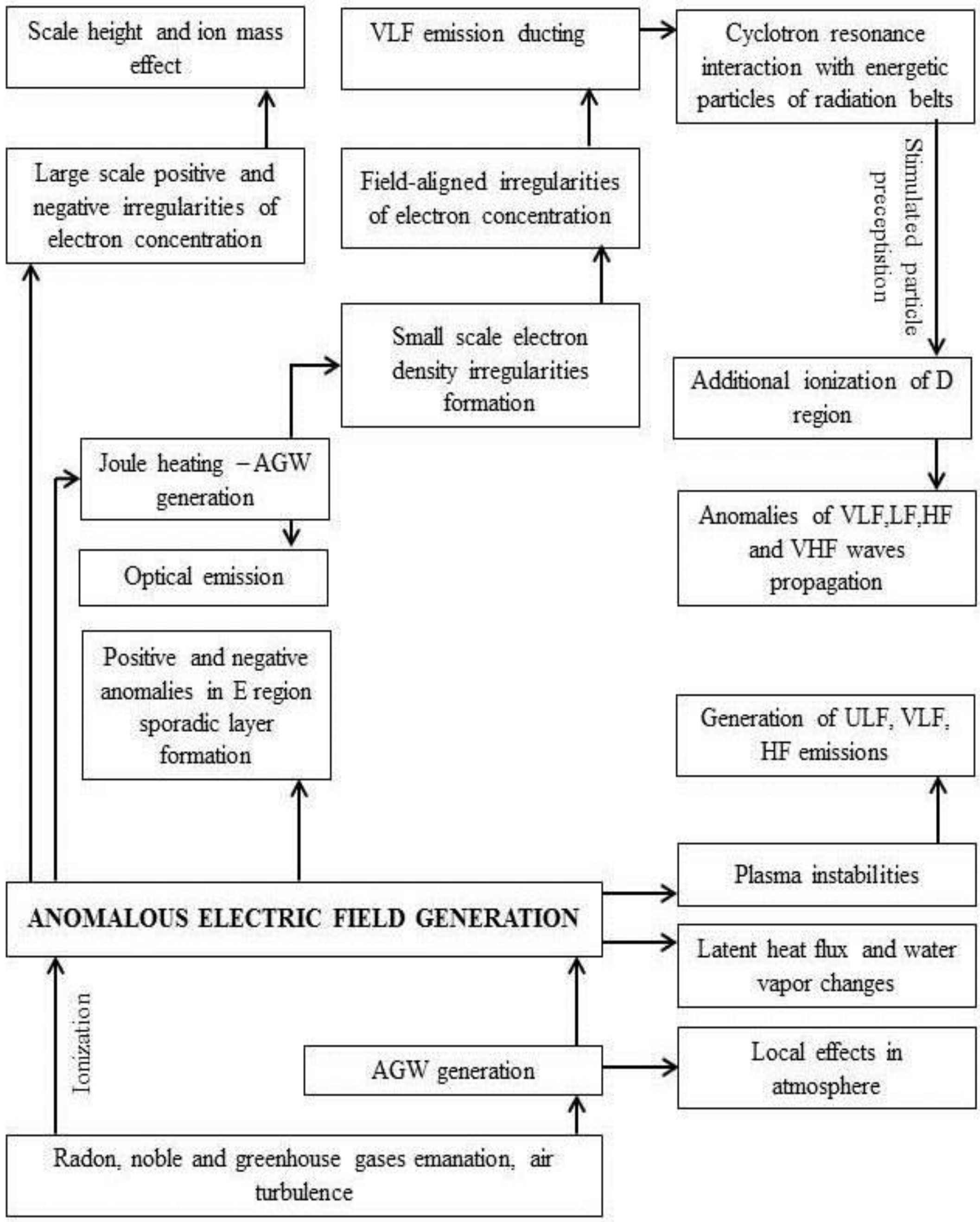

Figure 2.1 Physical mechanism of seismo-ionospheric coupling (S. Pulinets, 2004)

However, the physical mechanism of seismo-ionospheric still has not been completely clarified and needs more detailed study. So far, the most popular idea is acoustic gravity wave (AGW). Several studies have found acoustic gravity wave generated near the earthquake preparation zone prior to and during the large earthquake (Afraimovich, Perevalova, Plotnikov, & Uralov, 2000; Kherani et al., 2012; Sun et al., 2016). The AGW can be observed and detected through a few methods such as Total Electric Content (TEC) measured by Global Positioning System (GPS) receiver (A. M. Hasbi et al., 2011; Tao et al., 2017; Vita, Putra, Subakti, & Muslim, 2017), space-borne Extremely Low Frequency/Ultra Low Frequency/Very Low Frequency (ELF/ULF/VLF) transmitter (Bhattacharya et al., 2009; Błęçki et al., 2010; Ho et al., 2013; Ibanga, Akpan, George, Ekanem, & George, 2017; Sarkar, Choudhary, Sonakia, Vishwakarma, & Gwal, 2012; Zeng, Zhang, Fang, Wang, & Yin, 2009), HF Doppler sounding (Chum et al., 2016; J. Liu et al., 2006), ionosonde (J. Liu, Chen, Pulinets, Tsai, & Chuo, 2000; Maruyama, Tsugawa, Kato, Ishii, & Nishioka, 2012; Maruyama, Yusupov, & Akchurin, 2016) and ground based VLF transmitter (Chakraborty, Sasmal, Chakrabarti, & Bhattacharya, 2018; Hayakawa et al., 2012; Potirakis, Contoyiannis, Asano, & Hayakawa, 2018; Singh, Singh, & Pundhir, 2017).

One of the common ionospheric parameters that are used to characterize the variations in ionosphere due to the AGW is known as Total Electron Content (TEC). It is the electron density measured by GPS receiver that integrates the signal sources from both satellite and ground receiver (Devi et al., 2018; A. M. Hasbi et al., 2011; Heki et al., 2006; Kathuria, Grover, Ray, & Sharma, 2017; Kon et al., 2011). These sources include satellite probes such as Detection of Electro-Magnetic Emissions Transmitted from Earthquake Regions (DEMETER) and CHAMP, as well as HF

Doppler Sounder from ground based (Artru, Farges, & Lognonné, 2004; Gwal, Jain, Panda, & Gujar, 2011; Sun et al., 2016). The findings demonstrate that the variation of ionospheric parameters and ionization level can be detected a few hours to a few days before the large earthquake (with magnitude > 6.0) occurs. As a conclusion, electron density is a prime parameter required for ionosphere modelling.

2.4 The E-layer of Ionosphere

The E-layer in the ionosphere is characterized by means of electron concentration (Appleton, 1927). The E-layer can be described by the Chapman layer (Chapman, 1931) and located at heights between 90 to 120 km. In E-layer, the ionization is caused mainly by Extreme Ultra Violet (XUV) from 80 nm to L-beta and X-rays in the 8-10.4 nm range (Schunk & Nagy, 2009). The dominant ionized particle are O_2^+ and NO^+. Typically the electron concentration of the E-layer vanished after sunset, leaving very low electron concentration at night. Whitehead (1961) named this layer as sporadic E-layer or Es that remains weakly ionized during at night (Zolesi & Cander, 2014). The convergence of the vertical flux of metallic ions that are believed origin from the meteor, such as Fe^+ and Mg^+ caused the formation of Es layer (S. Pulinets, 2004).

The E-layer also very sensitive to the atmospheric gravity waves (Kaladze, Tsamalashvili, & Kaladze, 2011). Since the 1960s, the scientists discover vertically propagating ionospheric disturbances before the great Alaskan earthquake, detected by HF Doppler (Davies & Baker, 1965; Leonard & Barnes, 1965; Row, 1966). The acoustic gravity waves appear in the long time period, about 15 minutes and can travel up to 500 km (Koshevaya, Makarets, Grimalsky, Kotsarenko, & Enríquez, 2005).

The ionospheric E-layer study related to the earthquake must take into account all possible solar and geomagnetic to ensure any anomaly can be measured for hours to days before the earthquake, precisely. In this study, the solar flux index, F10.7, Kp, Ap and Dst indices are analysed. The F10.7 index is an indicator of solar activity by measuring the noise level generated by the Sun at a wavelength of 10.7 cm at the Earth's orbit (Schmidtke, 1976). The Ap index is a daily coverage for geomagnetic activity and Kp index is 3 hour average for geomagnetic activity. Both index measured by magnetometer at the ground and depend on E-layer Pedersen and Hall conductivities in local ionosphere (Clilverd, Clark, Clarke, & Rishbeth, 1998). The Dst index is a direct measure of the strength of the intensity of the globally symmetrical electrojet in the equatorial plane (Jakowski, Borries, & Wilken, 2012). Dst index is derived from the hourly scaling of low latitude horizontal magnetic variation. Unit for Dst, Kp, and Ap indices are unit of nanoTesla (nT).

In F-layer, both day and night ratio of ion concentration is smaller than E-layer. For the purpose to limit the scope of this research, we selected the electron density profile in E-layer only.

2.5 The CHAMP Satellite

CHAMP is the acronym for the Germany satellite known as CHAllenging Minisatellite Payload which was launched from Cosmodrome Pbsetsk on July 15, 2000. This satellite occupies the low earth orbit (LEO) in a circular and near polar orbit. The satellite in polar orbit pass over the North and South and cross over South

East Asia 4 times per day, making it suitable to study ionospheric ionization on a global scale. The CHAMP applied the Global Positioning System (GPS) radio occultation technique to profile ionospheric electron density from satellite orbit's height. The on-board payload of CHAMP measures Earth's gravity and magnetic field data. The information of global magnetic field model, temperature and electron density distribution are then derived from the raw data (Jakowski et al., 2002). The GPS data of CHAMP's and the result of data analysis download from the Information System and Data Centre (ISDC) website (http://www.gfz-potsdam.de/en/home/).

2.5.1 The CHAMP Radio Occultation Technique

The Earth surfaces that move suddenly in vertical can excite seismo-traveling ionosphere disturbance to cause anomaly in the vertical profile of the electron density, N_e. This vertical movement is detected up to tens to several thousand kilometres height (Nguyen, Furse, & Simpson, 2015; Sun et al., 2016) and monitored from the ionosonde and satellite. The electron density (N_e) data is obtained based on the Radio Occultation (RO) technique. This technique has been applied by the Global Positioning System / Meteorology (GPS/MET) constellation satellite which main mission is to profile the Earth's atmosphere. RO technique is developed for the mission to study atmosphere in Mars in 1960. The potential to use RO technique for atmosphere profiling show in GPS/MET mission that consists of CHAMP, SAC-C (Satellite de Aplicaciones Cientificas-C), GRACE (Gravity Recovery and Climate Experiment), Metop-A and TerraSAR-X (Anthes, 2011).

In the RO technique, signal passes through the vertical gradient of the refractivity in the atmosphere based on time path delays. This occurs when GPS satellites crossed the Earth atmosphere at lower orbit on a LEO satellite that is located on the opposite sides of the planetary limb (Ware et al., 1996). The diagram in Figure 3.1 illustrates the RO technique, showing a GPS satellite, a LEO satellite and a ray path of a transmitting signal through the atmosphere. The vertical electron density profile from the above-mentioned source has been acquired to model ionosphere above earthquake epicentre in Aceh, Sumatera in this thesis.

2.6 The IRI Model

The IRI model is a popular model for ionosphere study. It is a project sponsored by the Committee of Space Research (COSPAR) and the International Union of Radio Science (URSI) (Bilitza et al., 2014). This model provides the ionosphere parameters (electron density, total electron content (TEC), electron and ion temperatures, ion composition and ions drift) which are updated on a monthly basis. The data sources are from the ionosonde, incoherent scatter radars, topside sounders, and in situ instruments mounted on satellites and sounding rockets.

2.7 FDTD Modelling of Earth-Ionosphere

The FDTD method was introduced by K.S Yee in 1966 (Kane, 1966). The method was later named FDTD by Taflove (1980). It was implemented on a cubic-unit-cell space lattice to solve the Maxwell's equations. FDTD is the method of choice for numerically modelling of complicated electromagnetic systems in many areas, including engineering and atmospheric sciences. The robustness of the FDTD technique lies in its ability to adapt continuously varying parameters throughout the propagation path, and hence suitable for modelling the ionospheric problem. In this thesis, the FDTD algorithm is implemented by developing a home-grown source code using Fortran 90 in the Linux-based system. The FORTRAN code is attached in the Appendix 1. Graphical visualization and some post processing are performed using the open source software, Gnuplot (Janert, 2010).

The modelling of the electromagnetic signal may correlate to the extensive study on ionospheric disturbance as earthquake precursor. The study in earthquake precursor by observing the electromagnetic signal has been initiated since a few decades ago, where the focus is on the lithosphere-atmosphere-ionosphere prior to the large earthquake (Chmyrev et al., 2013; Harrison, Aplin, & Rycroft, 2010; Molchanov et al., 2004; Oyama et al., 2016).

The vertical electric field during seismic activity, when underground gases emanation is occurring, can be modelled based on Maxwell's equation that governs the general propagation of electromagnetic waves. The most popular way to time-step Maxwell's equations is via the FDTD method. To date, as far as we are aware of, no simulation work has been done on vertical electric field modelling using FDTD over Malaysia-Sumatera region. The closest is perhaps the work by Santosa, Hobara, and Munir (2014), which is a 2D FDTD modelling at lower stratosphere in horizontal to detect VLF anomaly due to seismic activity in Indonesia region.

The literature on the development of FDTD model to study electromagnetic waves perturbation in ionosphere shows a variety of approach, depending on the subject of study in the ionosphere. The E-region in the ionosphere is anisotropic, dispersive and comprised of magnetized plasma layer. Generally speaking it is a complicated system to model. Literature on FDTD modelling for ionosphere in prior studies has focused on isotropic ionosphere in D layer (Bérenger, 2002; Cummer, 2000; J. J. Simpson & Taflove, 2006a, 2007; Thevenot, Berenger, MonediÈre, & Jecko, 1999; Wenyi & Cummer, 2006). Electromagnetic wave propagation through ionosphere using FDTD method has been conducted to investigate such a wide area, including lightning observation (Wenyi & Cummer, 2006), Schumann resonances (Simões et al., 2008; Soriano, Navarro, Morente, & Portí, 2007), pre-seismic emission and remote sensing of localized radar (Jamesina J. Simpson & Taflove, 2005; J. J. Simpson & Taflove, 2006a, 2006b), ionospheric electricity study from lightning source (Azadifar et al., 2016), sky wave propagation for communication system (J. P. Berenger, 2006), and others.

FDTD modelling of anisotropic, magnetized plasma of ionosphere was initially reported byNickisch and Franke (1992). Later, Thevenot et al. (1999) presented Very Low Frequency-Low Frequency (VLF-LF) radio waves propagation in ionosphere waveguide using spherical coordinates in two-dimensional. In addition,Wenyi and Cummer (2006) has applied two-dimensional FDTD method in cylindrical coordinates to model lightning electromagnetic pulse in anisotropic, magnetized ionosphere. Samimi and Simpson (2015) has improved the model in three-dimensional. Nguyen et al. (2015) have proposed a technique called Stochastic FDTD (S-FDTD) in three dimensional to solve a problem with irregularities of electron density profile in ionosphere.

Several numerical schemes have been introduced a few decades ago for modelling anisotropic and magnetized medium based on the FDTD framework. These techniques have been applied to a wide range of applications, ranging from integration circuit modelling, metamaterial, antenna propagation, magneto active plasma, radar to the ionosphere modelling. These numerical schemes include recursive convolution (RC) (Ding, Zhao, Yang, Liu, & Nie, 2017; Shaobin Liu, Mo, & Yuan, 2004; Mounirh, Adraoui, Charif, Yaich, & Khalladi, 2015; Shaobin, Naichang, & Jinjun, 2003), auxiliary differential equation (ADE) (Al-Jabr, Alsunaidi, Tien, & Ooi, 2013; Duan, Yang, Liu, & An, 2009; Nickisch & Franke, 1992; Takayama & Klaus, 2002; Zhou, Wang, & Cao, 2015), frequency dependent Z-transform (Huang & Li, 2004; Dennis M Sullivan, 1992; Weedon & Rappaport, 1997) and J-E convolution (Fang et al., 2016; Lijun, Jinjun, & Naichang, 2005; Lijun & Naichang, 2005; Qing, Katsurai, & Aoyagi, 1998; Roh, 2013; Ph Shubitidze et al., 1999; Yang, Xie, & Yu, 2011)

As a relevant concern to this thesis, there is a list of parameters that needs to be taken into account for modelling anisotropic, magnetized and inhomogeneous medium. One version of the RC method, Piecewise Linear Current Density Recursive Convolution (PLCDRC) demands a high computational cost (S Liu, Liu, & Hong, 2008); while ADE and Z-transform methods are too complex. These models have problems with stability condition because they require time-steps orders of magnitude smaller than permitted stability limit. This condition will cost on hard-disk storage. The J-E convolution method, which integrates both frequency dispersion and anisotropy, is able to handle dynamic and inhomogeneous medium. This method is independence from medium properties thus the stability condition applies in this method is same with free-space (Yu & Simpson, 2009). In this thesis, the J-E convolution method will be adopted and extended for modelling the ionosphere.

Modelling of anisotropic and magnetized ionosphere is a non-trivial, complicated task, involving mathematical reformulation on the details of how the FDTD procedure is implemented, and a high cost in computational storage. In addition, many of the FDTD modelling techniques offered in the literatures are only suited for global Earth modelling, and not so suitable for modelling of localized ionosphere, which is the focus of this thesis.

2.8 Absorbing Boundary Condition

In the implementation of FDTD scheme for time-stepping Maxwell's equations, absorbing boundary condition (ABC) is critical for absorption of electromagnetic waves propagated through any medium. Before Perfectly Matched Layer (PML) is introduced, ABC is implemented via the analytical ABC (Engquist & Majda, 1977; Mur, 1981) scheme, or the other scheme known as differential ABC (Taflove & Hagness, 2005).

PML is extensively and efficiently proven for homogeneous, inhomogeneous, linear, nonlinear, isotropic and anisotropic domains. The most popular PML version is that makes use of splitting the electric and magnetic fields, proposed by Berenger (J.-P. Berenger, 1994). This technique imposes fictitious conductivities in both electric and magnetic field to minimize reflection from the boundary. An extension of Berenger work, the unsplit field PML is introduced for anisotropic medium with complex permittivity and permeability. This idea is discussed in Yang et al. (2011), D. M. Sullivan (1996), Roh (2013), P. Shubitidze et al. (1999), Jianxiong, Luhong, Jinghong, and Jing (2009) and Kumar and Parkinson (2017).

2.9 Summary on Literature Review

In the literature, several theories have been proposed and studies have been conducted to explain the correlation between ionospheric disturbance and seismo-ionospheric coupling in terms of ionospheric perturbation, and its mechanism. Despite much research efforts in the past have, there is still a lack of a consensual, solid evidence for the mechanism of the coupling of electric field disturbance in the ionosphere with seismic sources. Further studies are still needed to establish a reliable methodology for modelling short-term earthquake precursor (Oyama et al., 2016). For the sake of modelling, observational data are required. These data are acquired from satellites and ground-based stations that periodically or constantly monitor the atmosphere. Since works on computational electromagnetic wave propagation are minimal in numbers for Sumatra-Andaman Island earthquake epicentre, modelling and simulation on this topic is deemed necessary for filling up the research gap, in which the investigation of electric field anomaly for earthquake precursor in this region will be conducted using FDTD. In addition, only a few researchers develop FDTD simulations for localizing electromagnetic wave propagation. Thus it is hard to find references similar to this work. The codes constructed previously simplify a few ionospheric parameters. The development process of the 2D FDTD codes for the anisotropic, dispersive and inhomogeneous condition is complex.

CHAPTER 3

METHODOLOGY

3.1 The Data Collection

The CHAMP satellite made several passes over South East Asia per day, and the data were collected during that period. The data is collected in the range of latitude of -10˚ and 10˚ and longitude 80˚ and 110˚ for the period 21st December 2004 until 26th December 2004. The data collected for the altitude between 90 km to 120 km. The days and time when the data were collected are as shown in Table 3.1.

Table 3.1 The days and time when the satellite data were collected

Date	**Time (LTC)**
21st Dec 2004	13:03
22nd Dec 2004	00:35
23rd Dec 2004	11:00
24th Dec 2004	00:01
24th Dec 2004	23:03
25th Dec 2004	10:31
	23:29
26th Dec 2004	12:33

The location for this case study was chosen around the Sumatera-Andaman Island Earthquake area, where the impact of this earthquake affected the local in Malaysia. Table 3.2 shows detail occurrence of the Sumatera-Andaman island earthquake.

Table 3.2 Information of the Sumatera-Andaman Island earthquake

Location	Date	Time of earthquake (UTC)	Latitude	Longitude	Depth (km)	Magnitude (Richter scale)	Earthquake preparation radius, R (km)
North Sumatra	26th Dec 2004	00:58	3.32° N	95.85° E	30	9.3	9977

3.2 FDTD Formulation

In general terms, in Taflove's version of FDTD, Maxwell's equations are solved using a strategically designed grid point method in the time domain, where the spatial grid is used to discretize the derivatives of Maxwell's curl equations in a finite difference spirit. The numerical solutions are then time-stepped sequentially, simulating the dynamical propagation of EM wave in the time domain through the medium defined in the simulation grid. The time-dependent partial differential form of Maxwell's equations is discretised using a central differencing scheme known as the leap-frog method. In the leap-frog scheme, the electric field and magnetic field components are placed on a lattice grid point, with the field components shifted by half a grid step both in the spatial and temporal index. For a simple illustration of discretization in the 1D case (involving only the x-component), the derivatives of a field $f(x)$ in the Maxwell's equations with respect to a variable r are discretized in a central difference manner (with a step size Δ), where O is a shorthand notation for the remainder term, which approaches zero as the square of the space increment (Taflove & Hagness, 2005)

$$\left.\frac{\partial f(x)}{\partial r}\right|_{r=r_0} = \lim_{\delta \to 0} \frac{f\left(r_0 + \frac{\Delta}{2}\right) - f(r_0 - \frac{\Delta}{2})}{\delta} + O(\Delta^2). \tag{3.1}$$

Within a semi-implicit approximation, where Δ is assumed to be sufficiently small, the following term becomes

$$\left(\frac{\Delta f}{\Delta r}\right)_m = \frac{f_{m+1/2} - f_{m-1/2}}{\Delta r}, \tag{3.2}$$

where the notation f_m denotes $f_m \equiv f(m\Delta)$. This expression can be easily generalized to 2D and 3D cases, and is used when numerically evaluating the partial differentiation of a field f with respect to a variable r (r can be either a temporal or spatial variable), while Δr is either spatial or temporal width.

The source of the EM wave in the FDTD simulation in this thesis is a 2D sinusoidal point source. 2D plane wave source is, in principle, possible to be generated and simulated in the FDTD simulation, but it is technically much more complicated. This thesis limits its scope to only the point source as it is sufficient to serve its main objectives, which is to simulate and measured the responses of an EM wave propagating through the perturbed ionosphere, and to propose a model for an earthquake precursor. The 2D point source of the EM wave will be located at the simulation grid with grid index ($i = 2, j = 2$).

The FDTD algorithm makes use of both $\boldsymbol{E}$ and $\boldsymbol{H}$ elements in Maxwell's curl equations concurrently to provide a robust numerical solution rather than solving them using either $\boldsymbol{E}$ or $\boldsymbol{H}$ alone (Taflove & Hagness, 2005). The leap-frog arrangement, which is the basic strategy of this algorithm, requires the information of previous time steps of $\boldsymbol{E}$ and $\boldsymbol{H}$. The components of $\boldsymbol{E}$ are computed and stored in memory by using previously stored data of $\boldsymbol{H}$. The cycle is continuous until the scheduled time-stepping is completed.

In the following, the detailed procedure to implement the FDTD algorithm in such an environment to time-step a 2D spherical EM wave is presented in the rectangular coordinate system. The algorithm is adopted from Qing et al. (1998) which has reported a working example to model similar system using FDTD and known as J-E convolution. The choice of this algorithm is a result after testing, in a trial-and-error manner, many numerical schemes reported in the literature to implement FDTD for anisotropic, dispersive medium. A dispersive medium is one which is field-dependent, direction-dependent and frequency-dependent electric and magnetic properties. The J-E convolution scheme has been exhaustively tested and found to deliver robust output after many pre-tests to practically implement it during the process of this thesis research.

In an anisotropic, dispersive medium, Maxwell's equation can be written as

$$\nabla \times \boldsymbol{E} = -\mu_0 \frac{\partial H}{\partial t}, \tag{3.3a}$$

$$\nabla \times \boldsymbol{H} = \varepsilon_0 \frac{\partial E}{\partial t} + \boldsymbol{J}, \tag{3.3b}$$

$$\frac{d\boldsymbol{J}}{dt} + \nu \boldsymbol{J} = \varepsilon_0 \omega_p^2 \boldsymbol{E} + \omega_b \times \boldsymbol{J}, \tag{3.3c}$$

where $\boldsymbol{J}$ is electric current density in unit of A/m^2, $\boldsymbol{E}$ is electric field intensity in unit of V/m, $\boldsymbol{H}$ is magnetic field intensity in unit of A/m, ε_0 and μ_0 are the permittivity and permeability of free space (Taflove & Hagness, 2005). The numerical solutions of the Maxwell's equations will be discussed in the light of transverse magnetic

(TM) mode, where the solutions are sufficiently represented in terms of the E_z, H_x and H_y components of the electromagnetic fields. These field components are to be treated as functions of the temporal variable (t) and a 2D spatial coordinate (x, y). Assumes that the incident wave is uniform and has no dependence on the spatial variable z, $\boldsymbol{B}_0$ is paralleled to the z-axis with angular frequencies $\omega_{bx} = 0, \omega_{by} = 0, \omega_{bz} = \omega_b$, Equation (3.3c) can be expressed as

$$\frac{dJ_z}{dt} = \varepsilon_0 \omega_p^2 E_z - \nu J_z. \tag{3.4}$$

Equation (3.4) is then Laplace transformed into the s-domain via the following expressions,

$$\frac{d\boldsymbol{J}(t)}{dt} \Leftrightarrow s\boldsymbol{J}(s) - \boldsymbol{J_0} \tag{3.5}$$

$$\varepsilon_0 \omega_p^2 \boldsymbol{E}(t) \Leftrightarrow \varepsilon_0 \omega_p^2 \boldsymbol{E}(s) \tag{3.6}$$

$$\Omega \boldsymbol{J}(t) \Leftrightarrow \Omega \boldsymbol{J}(s) \tag{3.7}$$

In the s-domain, equation (3.5) becomes

$$\boldsymbol{J}(s) = (s\boldsymbol{I} - \Omega)^{-\mathbf{1}} \boldsymbol{J_0} + \varepsilon_0 \omega_p^2 (s\boldsymbol{I} - \Omega)^{-\mathbf{1}} \boldsymbol{E}(s) \tag{3.8}$$

where $\boldsymbol{I}$ is the identity matrix. Here $\Omega = \begin{pmatrix} -\nu & -\omega_b \\ \omega_b & -\nu \end{pmatrix}$. The inverse matrix $(s\boldsymbol{I} -$

$\Omega)^{-\mathbf{1}}$ is expressed in terms of

$$\boldsymbol{A} = (s\boldsymbol{I} - \Omega)^{-\mathbf{1}} = \frac{1}{(s+\nu)^{\mathbf{2}} + \omega_b^2}\begin{pmatrix} s+\nu & -\omega_b \\ \omega_b & s+\nu \end{pmatrix}. \tag{3.9}$$

Equation (3.8) can be rewritten as

$$\boldsymbol{J}(s) = \boldsymbol{A}(s)\boldsymbol{J}_{\mathbf{0}} + \varepsilon_0\omega_p^2\boldsymbol{A}(s)\boldsymbol{E}(s). \tag{3.10}$$

By Laplace transforming Equation (3.10) back to the t-domain, $\boldsymbol{J}(t)$ becomes

$$\boldsymbol{J}(t) = \boldsymbol{A}(t)\boldsymbol{J}_{\mathbf{0}} + \varepsilon_0\omega_p^2\boldsymbol{K}(t), \tag{3.11}$$

where

$$\boldsymbol{A}(t) = e^{-\nu t}\begin{pmatrix} \cos\omega_b t & -\sin\omega_b t \\ \sin\omega_b t & \cos\omega_b t \end{pmatrix} \tag{3.12}$$

and

$$\boldsymbol{K}(t) = \boldsymbol{A}(t)\boldsymbol{E}(t). \tag{3.13}$$

J_z is only dependent on ν and ω_p, and independent on ω_b (Yang et al., 2011).

In the special case of $\omega_{bx} = 0, \omega_{by} = 0$, Equation (3.4) is discretized into the form (Δt is the size of the time step, n)

$$J_z|_{i,j}^{n+1/2} = e^{-\nu\Delta t} J_z|_{i,j}^{n+1/2} + \varepsilon_0 \omega_p^2 \Delta t e^{\frac{-\nu\Delta t}{2}} E_z|_{i,j}^{n}. \tag{3.14}$$

ω_p in Eq. 3.14 is defined by electron density N_e and derived in section 2.2. The relationship between ω_p and N_e is showed in Eq. 2.4.

Figure 3.1 shows the interface of the electric and magnetic field in the 2D FDTD formulation in TM mode. The current density J_z propagates in the same direction as that of the electric field E_z. The magnetic field components, H_x and H_y are necessary to update the electric field component, E_z.

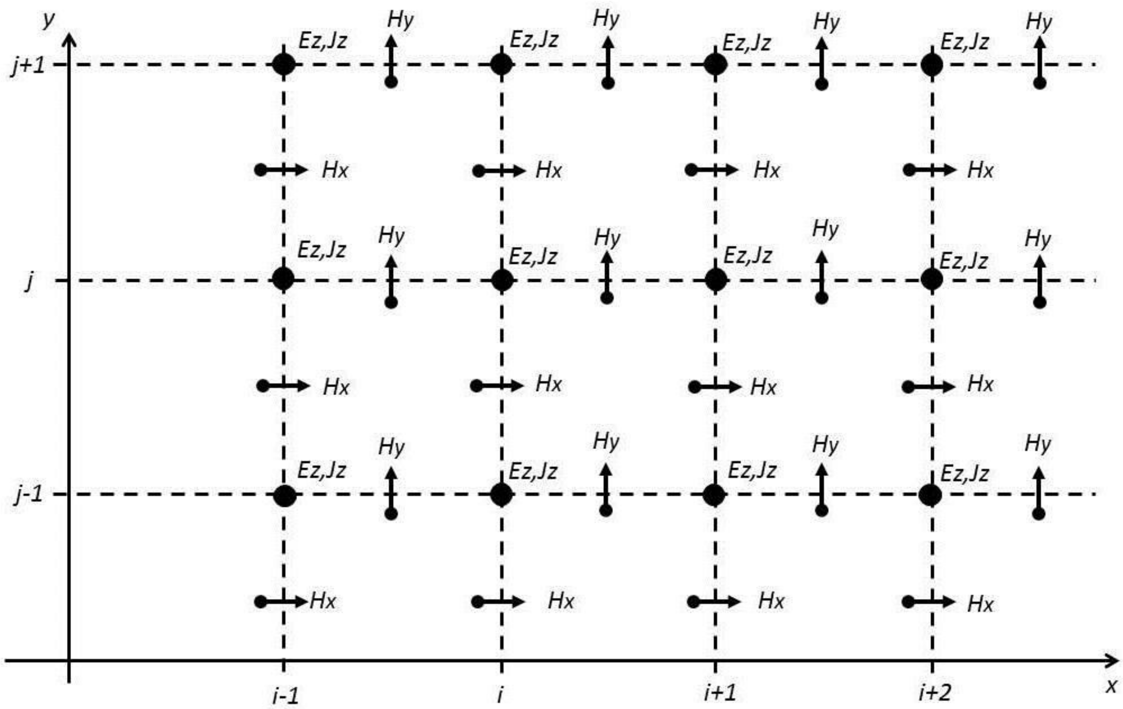

Figure 3.1 The electric field, E_z , current density, J_z and magnetic field, H_x and H_y in interface of the fields

The fields in the TM mode, E_z, H_x and H_y, are obtained by discretizing Equations (3.3),

$$H_x\Bigg|_{i,j+\frac{1}{2}}^{n+\frac{1}{2}} = D_{ax}(i,j)$$

$$* H_x\Big|_{i,j+1/2}^{n-1/2} - D_{bx}(i,j) * \left[E_z\Big|_{i,j+1}^{n} - E_z\Big|_{i,j}^{n}\right] \tag{3.15a}$$

$$H_y\Bigg|_{i+\frac{1}{2},j}^{n+\frac{1}{2}} = D_{ay}(i,j)$$

$$* H_y\Bigg|_{i+\frac{1}{2},j}^{n-\frac{1}{2}} + D_{by}(i,j) * \left[E_z\Big|_{i+1,j}^{n} - E_z\Big|_{i,j}^{n}\right] \tag{3.15b}$$

$$E_z\Big|_{i,j}^{n} = C_{ax}(i,j) * E_z\Big|_{i,j}^{n} - J_z|_{i,j}^{n+1}$$

$$+ C_{bx}(i.j)\left[H_y\Big|_{i+\frac{1}{2},j}^{n+\frac{1}{2}} - H_y\Big|_{1-\frac{1}{2},j}^{n+\frac{1}{2}} - H_x\Big|_{i,j+\frac{1}{2}}^{n+\frac{1}{2}} - H_x\Big|_{i,j-\frac{1}{2}}^{n+\frac{1}{2}}\right] \tag{3.15c}$$

$$J_z|_{i,j}^{n+1/2} = e^{-\nu\Delta t} J_z|_{i,j}^{n+1/2} + \varepsilon_0 \omega_p^2 \Delta t e^{\frac{-\nu\Delta t}{2}} E_z|_{i,j}^{n} \tag{3.15d}$$

C_{ax}, C_{bx} are the coefficients for electric field and $D_{ax}, D_{bx}, D_{ay}, D_{by}$ are the coefficients for magnetic field, which are define as

$$C_{ax}(i,j) = \frac{\left(1 - \frac{\sigma\Delta t}{2\varepsilon_0}\right)}{\left(1 + \frac{\sigma\Delta t}{2\varepsilon_0}\right)} \tag{3.16}$$

$$C_{bx}(i,j) = \frac{\left(\frac{\Delta t}{\varepsilon_0 \Delta}\right)}{\left(1 + \frac{\sigma \Delta t}{2\varepsilon_0}\right)} \tag{3.17}$$

$$D_{ax}(i,j) = D_{ay}(i,j) = \frac{\left(1 - \frac{\sigma^* \Delta t}{2\mu_0}\right)}{\left(1 + \frac{\sigma^* \Delta t}{2\mu_0}\right)} \tag{3.18}$$

$$D_{bx}(i,j) = D_{by}(i,j) = \frac{\left(\frac{\Delta t}{\mu_0 \Delta}\right)}{\left(1 + \frac{\sigma^* \Delta t}{2\mu_0}\right)} \tag{3.19}$$

where $\sigma = \sigma^*$ is conductivity of the material. In this case, σ is applied in electric field element and σ^* is applied in magnetic field element. $\Delta = \Delta x = \Delta y$ is the spatial width, and is expressed in terms of the fragment of the wavelength λ via $\Delta = \lambda/N$, where N either a positive real or positive integer n and (i,j) represent the temporal and spatial discretization indices respectively. The convergence of FDTD (i.e., the time-stepping evolution of the EM profile after many steps remains finite and stable) depends on the choice of Δt which has to be sufficiently small to ensure the wave has enough time to propagate through the spatial grid. This requirement is known as Courant-Friedrich-Lewy (CFL) stability factor (Courant, Friedrichs, & Lewy, 1967). The limit for time increment to ensure stability in 2D FDTD is given by

$$\Delta t \leq \frac{1}{c_0 \sqrt{\frac{1}{(\Delta x)^2} + \frac{1}{(\Delta y)^2}}} \tag{3.20}$$

where c_0 is the speed of light. We define CFL number as

$$\mathrm{CFL} = c_0 \Delta t \sqrt{\frac{1}{(\Delta x)^2} + \frac{1}{(\Delta y)^2}} \tag{3.21}$$

and the stability condition may write as

$$\mathrm{CFL} < 1. \tag{3.22}$$

As for simplification, time increment to satisfy CFL stability requirement in 2D can be written as

$$\Delta t = \frac{\Delta}{2c_0} \tag{3.23}$$

The wave source for the FDTD modelling in this thesis is implemented by generating a point sinusoidal source at the grid site $i = 2, j = 2$, via

$$E_z \Big|_{i,j}^{n} = A_0 \sin(2\pi f_0 n \Delta t), \tag{3.24}$$

where f_0 is frequency which is 30 kHz, A_0 is amplitude which is set to 10 m. At source of grid site $i = 2, j = 2$, E_z is equal to 3.09017 V/m.

3.3 Implementation of Absorbing Boundary Condition

The wave propagation cannot be simulated infinitely in an active grid hence it needs to be terminated at the edges. Absorbing boundary condition (ABC) is based on the mechanism where fields are dampened as they propagate into an absorbing medium. In any FDTD simulation, absorbing boundary condition must be set up in all edges enclosing the active simulation grid.

Two kinds of ABC have been implemented in the FDTD code developed in this thesis. The first is the first order ABC (Cela, 2012) and the second is the PML absorbing boundary condition proposed by J.-P. Berenger (1994). It is not known *a prior* which kind of ABC will work best before their implementation. In this thesis, two different types of ABC are implemented as a means to decide which ABC works best for time-stepping the EM fields in the anisotropic ionosphere, and at the same time, compare the effectiveness of both. The 2D computational grid for the present FDTD modelling is as shown in Figure 3.2. This computational grid is a rectangle with a dimension of 600 km $\times$ 120 km along the x- and y-directions. This is to be known as the active simulation grid, represented by the unshaded area in the middle Figure 3.2. The shaded stripes along the edges are grid layers where ABC is to be implemented. The width of these stripes is common on all sides, and in general, varies according to the parameters used in the ABC implemented.

As it turns out, in the ionospheric case considered in this thesis, it is found that, after various simulation attempts to implement ABC in the anisotropic environment, reflection from the boundary is not suppressed entirely but only to a certain extent. The quantitative performance of two types of ABC, to be discussed below, will be presented in better detail in the following chapters.

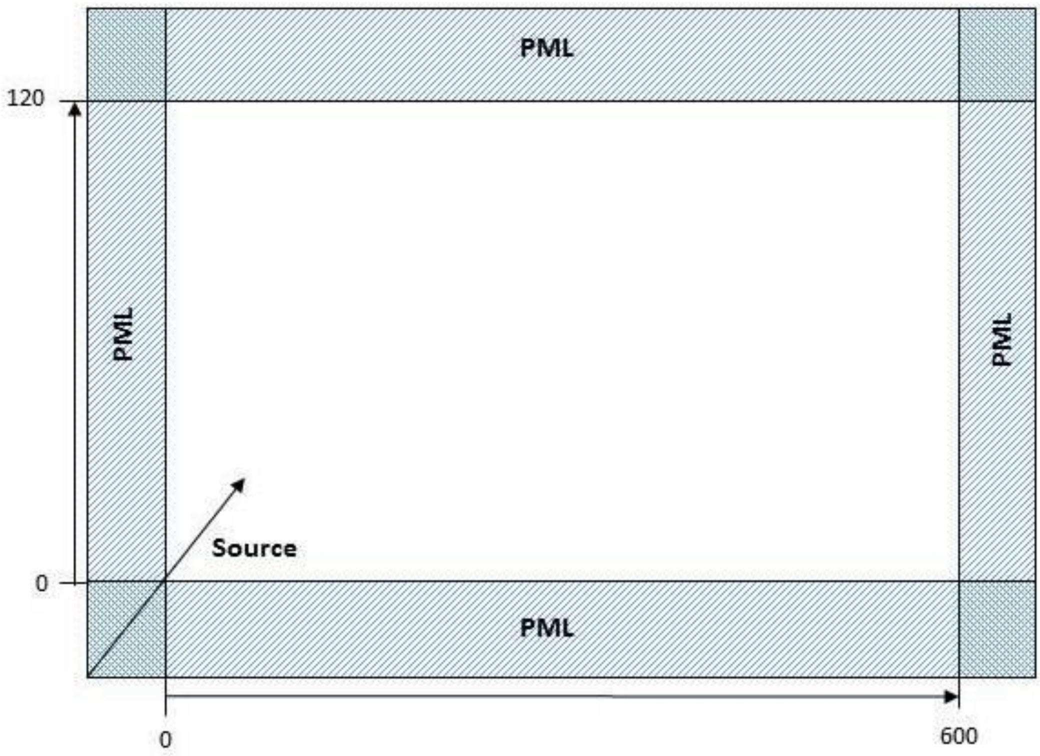

Figure 3.2 Two-dimensional computational grids for wave propagation. The shaded stripes along the edges are grid layers where ABC is to be implemented.

In ABC, the electric fields travel at one time steps and magnetic field travel at halftime steps, so to terminate the propagated wave, two-time steps are necessary. Equation 3.25 shows how the ABC is implemented.

$$E_z\Big|_{0,j}^{n+1} = E_z\Big|_{1,j}^{n} \tag{3.25a}$$

$$E_z\Big|_{1,j}^{n+1} = E_z\Big|_{ie-1,j}^{n} \tag{3.25b}$$

$$E_z\Big|_{i,je}^{n+1} = E_z\Big|_{i,je-1}^{n} \tag{3.25c}$$

where $i = 1,2,3, \dots \dots \dots ., ie$, $j = 1,2,3, \dots \dots \dots, je$, $ie = 600$ and $je = 120$. By implementing this condition, the wave will be absorbed by the termination at the edges.

The second kind of ABC, the PML type ABC, was first proposed by Kane (1966). A PML absorber layer which has a dumping profile is introduced at the edge of the simulation grid. The dumping profile of the absorber layer is characterised by a spatially varying function, comprised of a few independent variables such as conductivity, PML thickness and reflection coefficient. Rickard and Georgieva (2003) suggested that wave absorption performance can be improved over a wide range of frequency if the conductivity is made into a function σ_k that varies in a stepwise manner from one spatial grid point k to the next. In a 2D simulation grid, k refers to either the spatial i or j index. This will allow for the development of a loss at a different rate when waves (which incident from the active simulation grid section) propagate into this layer. In order to achieve almost reflection-free scenario, Rickard proposed a PML conductivity function that contains a loss factor, defined as $\alpha_k(\rho)$ in Eq. (3.26) that assumes the form of

$$\sigma_k(\rho) = \sigma_{\max} \left(\frac{\rho_k}{\delta_k} \right)^{k+\beta} \tag{3.26a}$$

$$\alpha_k(\rho) = 1 + \varepsilon_{\max} \left(\frac{\rho_k}{\delta_k} \right)^{k} \tag{3.26b}$$

The user-defined parameter, $\sigma_{\max}$ is to control the attenuation of propagating waves as below

$$\sigma_{\max} = -\left[(h + \beta + 1)\varepsilon_0 \cdot c_0 \cdot \ln R_0 / [2/\delta_k]\right] \quad (3.27)$$

where R_0 is the reflection coefficient, δ_k is the thickness of the PML in the grid index by k, h is the user-defined rate of growth, β is the user-defined difference in the exponent rates, ε_{max} is the user-defined parameter to control the rate of evanescent mode attenuation, ρ_k is the depth in PML (measured orthogonally from the boundary separating the active simulation grid and the PML), and c_0 is the speed of light. Table 3.3 shows the range for each parameters, as proposed by Rickard and Georgieva (2003)

Table 3.3 PML absorber parameters and the range

Parameter	User-defined range	Proposed value
$\boldsymbol{R_0}$	$[10^{-2}, 10^{-12}]$	10^{-5}
$\boldsymbol{\rho_k}$	$0 \leq \rho_k \leq \delta_k$	
$\boldsymbol{\varepsilon_{\max}}$	$[0,10]$	0
$\boldsymbol{h}$	$[2,6]$	4
$\boldsymbol{\beta}$	$[-3,3]$	0

In this thesis, a PML strip is appended at the edge of the simulation grid with a total width of 25 cells (each cell has a width of δ_k). The conductivity σ_k is applied in the FDTD code through the medium coefficient as below:

$$C_{ax}(i,k) = \frac{\left(1 - \frac{\sigma_k \Delta t}{2\varepsilon_0}\right)}{\left(1 + \frac{\sigma_k \Delta t}{2\varepsilon_0}\right)}, \tag{3.28}$$

$$C_{bx}(i,k) = \frac{\left(\frac{\Delta t}{\varepsilon_0 \Delta}\right)}{\left(1 + \frac{\sigma_k \Delta t}{2\varepsilon_0}\right)}, \tag{3.29}$$

$$D_{ax}(i,k) = D_{ay}(k,j) = \frac{\left(1 - \frac{\sigma_k^* \Delta t}{2\mu_0}\right)}{\left(1 + \frac{\sigma_k^* \Delta t}{2\mu_0}\right)}, \tag{3.30}$$

$$D_{bx}(i,k) = D_{by}(k,j) = \frac{\left(\frac{\Delta t}{\mu_0 \Delta}\right)}{\left(1 + \frac{\sigma_k^* \Delta t}{2\mu_0}\right)}, \tag{3.31}$$

where $\sigma_k^* = \sigma_k$. Table 3.4 summarizes the values of the FDTD and PML parameters used in the 2D simulation for the TM mode.

Table 3.4 Main parameters of the FDTD and PML parameters

Parameters		
Dimension of active simulation region	:	$600\ \times 120\ \Delta x$
No of PML layers	:	25
EM source	:	2-D sinusoidal point source
Source location	:	$i = 2, j = 2$
Frequency, $\boldsymbol{f_0}$	:	30 kHz
Courant factor for numerical stability, $\boldsymbol{S}$	:	$\Delta t = 1.6 \times 10^{-6}$ $\Delta x = \lambda/10$ $S = c_0 \Delta t/\Delta x$
Numerical dispersion	:	1 km
Relative permittivity,$\boldsymbol{\varepsilon_0}$	:	1
Relative permeability, $\boldsymbol{\mu_0}$	:	1

For the sake of comparing the effectiveness of the differential ABC and the PML, the electric field E_z is probed at 6 different sites in the active simulation region, denoted as A, B, C, D, E and F in Figure 3.3. All these points are selected randomly for the purpose of observation.

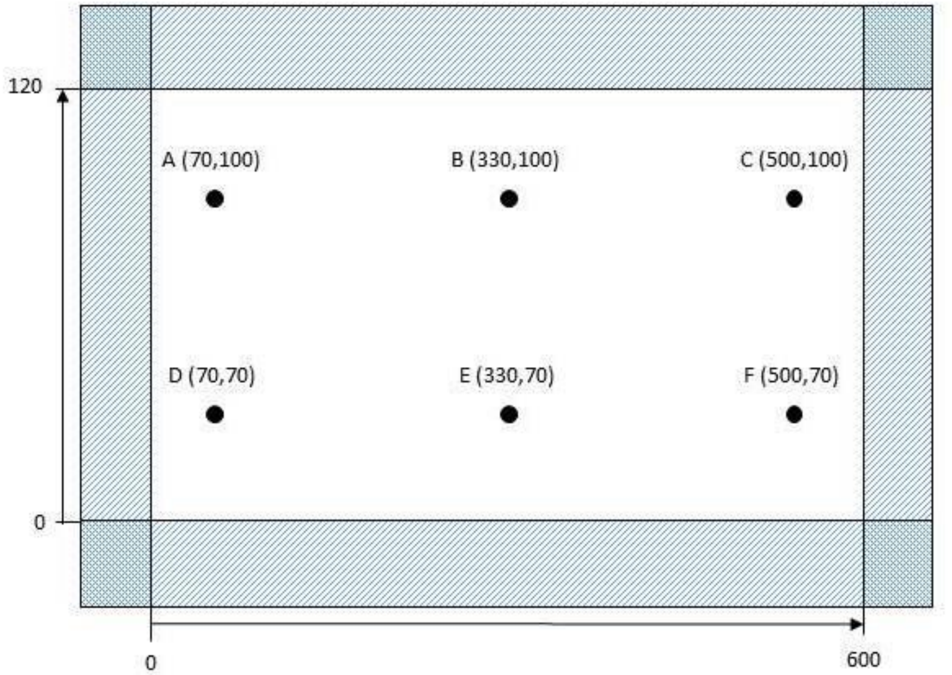

Figure 3.3 The location of the sites in which the relative error of the electric field is accessed.

The relative error calculation is conduct to report the accuracy of measurement quantitatively. As a definition, the relative error is the absolute error divided by the magnitude of exact value. The absolute error is referring to the magnitude of the difference between exact value and approximation. The lower relative error is considering better accuracy. At each site, the relative error at a given instant time-step n is measured as per

$$\text{Rel. error}|_{i,j}^{n} = \left|E_z|_{i,j}^{n} - E_{\text{ref}}|_{i,j}^{n}\right| \Big/ \left|E_{\text{ref,max}}\big|_{i,j}\right|, \tag{3.32}$$

where the reference value E_{ref} is an electric field at a probing site at time-step n in a reference domain which is an extra-large grid of the dimension 1000×360 (Taflove

& Hagness, 2005). The value $E_{\mathrm{ref}}|_{i,j}^{n}$ is the value of E_z independently measured in the reference domain at time n when reflections from the boundaries has not arrived at (i,j) during the time $E_z|_{i,j}^{n}$ (which may contain contamination from reflection from the edges) is being recorded. $E_{\mathrm{ref}}|_{i,j}^{n}$ is, by designed, free from the contamination of the edge-reflected waves throughout the whole course of simulation. $E_{\mathrm{ref,max}}$ is the maximum amplitude of the electric field in the reference solution E_{ref}, observed during the time-stepping time of interest (Taflove & Hagness, 2005).

The effectiveness of both kinds of ABC mentioned above is investigated by carrying out a numerical experiment and compares the relative error obtained in each case. To this end, the relative error is measured in each time step n for PML with varying cell number 5, 10, 15, 20 and 25. The results of this numerical experiment will be reported in the appropriate section in the subsequent chapters to quantitatively access the effectiveness of these two ABC.

3.4 Codes Verification

This process is to examine the sensitivity of the codes with the presence of electron density profile. The electromagnetic wave is propagating in 2D FDTD through 3 conditions. First, electromagnetic wave propagates in free space medium. This medium has no electron density profile. Then, the second condition is an anisotropic medium with electron density profile extracted from the theoretical Equation (2.6). The third condition is an anisotropic condition with experimental data from CHAMP satellite. The data is from 21st December 2004, 23:03 LTC. We monitor the behaviour of the waves and the graph plot in a collective manner.

As a concluding remark, the flowchart of the FDTD algorithm for the simulation done in this thesis is summarized in Figure 3.6. The input parameters which are medium properties $(\omega_p, \omega_b, \nu)$ are defined at first before calculated the coefficient. These medium properties are calculated from electron density, N_e data. The material coefficients $(C_{ax}, C_{by}, D_{ax}, D_{by})$ are calculated after defining the material properties. Then, the electric field element in z-direction, E_z is calculated followed by magnetic field elements from x and y directions. The absorbing boundary condition is set up before the propagated wave reaches the boundary.

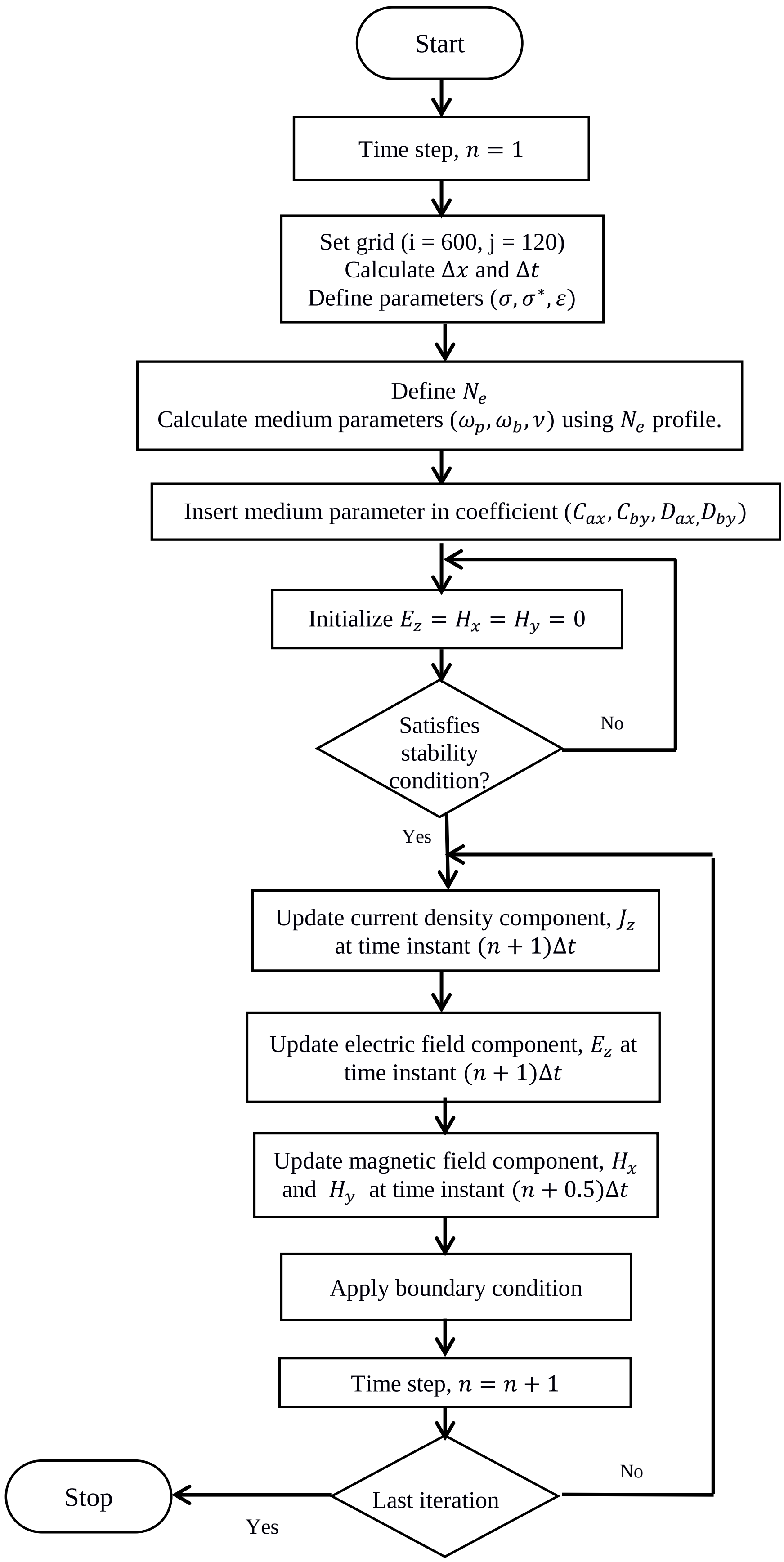

Figure 3.4 Flow-chart of the FDTD algorithm.

3.5 Summary

To use the FDTD methodology to simulate the intended system as mentioned above, a major ingredient required is the information of the atmosphere's electron density profile $N_e(h)$ as a function of altitude h. $N_e(h)$ at low altitude is low. At the (high) altitude range of ~ 90 km – 120 km, i.e., in the ionospheric region, $N_e(h)$ becomes significant. In this thesis, $N_e(h)$ is measured by the CHAMP satellite. The data from the CHAMP satellite were collected for a few days before and during the occurrence of the earthquake. Data of quiet and perturbed condition were analysed based on solar activity and geomagnetic storm indices.

Two absorbing boundary conditions, namely, differential ABC and PML have been implemented in the 2D FDTD code for the anisotropic, inhomogeneous and dispersive medium of the ionosphere. ABC is an integral ingredient in any FDTD code. It ensures the simulated EM propagation suffers a minimal amount of 'contamination' during simulation, i.e., interference originated from the reflection of the boundary, which is an undesirable numerical artefact not present in a realistic scenario. Numerical experiments designed to access the efficiency of both ABC reveal that the PML performs relative better than the differential ABC.

Another numerical experiment has also been conducted to check whether the codes made response sensitively to the variation in the $N_e(h)$ profile. In this experiment, the propagation of EM fields is simulated using three different atmospheric media, namely, free space, space filled with $N_e(h)$ measured from the CHAMP data, and $N_e(h)$ calculated based on the theoretical equation defined in Equation (2.6).

CHAPTER 4

ELECTRON DENSITY PROFILE IDENTIFICATION NEAR THE EARTHQUAKE ACTIVE REGION IN SOUTHEAST ASIA

4.1 Introduction

This chapter is devoted to present the identification of the electron density profile data which raw form was obtained from the available satellite sources. The results presented here constitute an integral part of the research work in this thesis. The numerical data of the electron density profile of the ionosphere analysed in this chapter will be fed in as the input information to the FDTD code for simulating the EM propagation in the ionosphere in the subsequent chapter.

The case study area for this thesis is located in the equatorial region, in which the ionosphere is observed to have the highest electron concentration peak because of the Equatorial Ionization Anomaly (EIA) effect. As such, the ionospheric electron density profile becomes relatively easy to be measured in this region compared to others. This chapter will present the electron density profile acquired near the 2004 Indonesia earthquake active region. To this end, the electron density profile five days ahead, during and after the earthquake was acquired from two different sources; one from satellite and the other from an empirical model will be discussed and compared.

4.2 Space Weather Condition for December 2004

The electron density could be perturbed due to causes such as strong solar and magnetic activity. Therefore, it is necessary to check the space weather condition on the respective date of investigation to ensure that the ionospheric disturbance was indeed caused by earthquake activity instead of solar activity or geomagnetic disturbance. To this end, we refer to the data for the solar flux (F10.7) magnetic field, Kp and geomagnetic storm, Dst indices, which are available in the Space Weather live website (http://www.spaceweatherlive.com/en/archive). Solar flux index is a solar activity level indicator and always refer to F10.7, a measurement of the total emission at a wavelength 10.7 cm in the unit of solar flux unit (s.f.u) (Tapping, 2013). The magnetic index, Kp is a 3 hour index of the level of geomagnetic activity and Dst index is an index of magnetic disturbances due to the ring current around the Earth (Rostoker, 1972) Figure 4.1 shows the solar flux F10.7, followed by Kp index in Figure 4.2 and Dst index for December 2004 in Figure 4.3. It is good to be noted here that for the low solar activity, F10.7 is less than 150 s.f.u (Bruevich & Bruevich, 2013). Geomagnetic activity level is indicated by Kp, Ap and Dst indices. Gosling, McComas, Phillips, and Bame (1991) proposed a criterion based on 3-hours Kp index (0 = low, 9 = most intense storm). A “major” storm has Kp ≥ 8; a “large” storm has Kp ≤ 7. A “medium” storm has Kp ≥ 6 and “small” storm has Kp ≤ 5. Meanwhile, Gonzalez et al. (1994) suggested Dst index value ≤ -100 nT for the intense storm, -100 ≤ Dst ≤ -50 nT for the moderate storm and ≤ -30 nT for the small storm while Ap index is daily coverage level for geomagnetic activity. Geomagnetic storms are labelled G1 to G5. For a better understanding, definition for geomagnetic storms in Kp index values are G1 = Kp 5, G2 = Kp 6, G3 = Kp 7, G4 = Kp 8 and G5 = Kp 9.

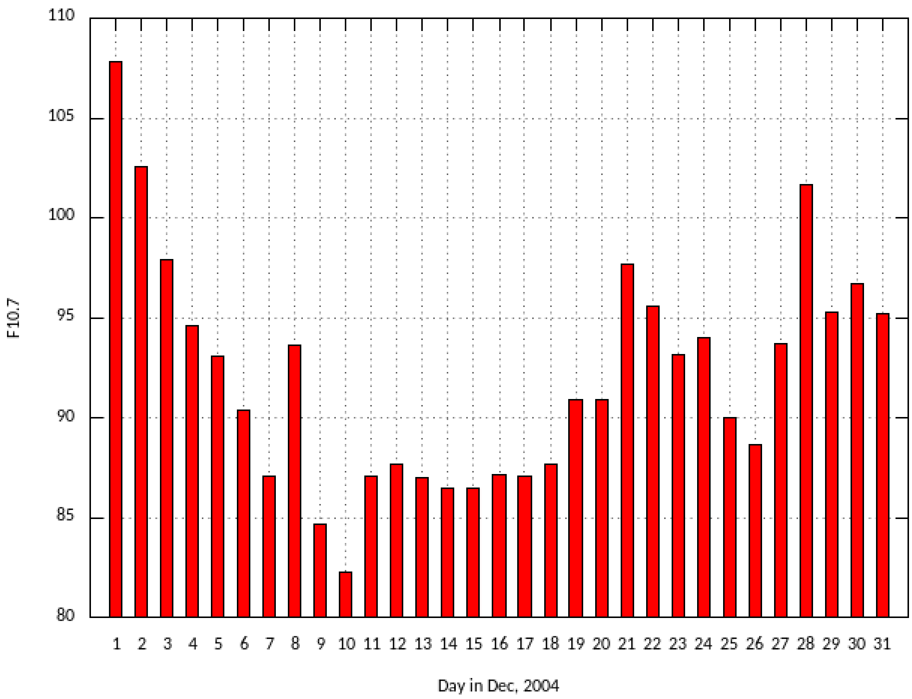

Figure 4.1 Solar flux F10.7 on December 2004

(Page URL: https://www.spaceweatherlive.com/en/archive , downloaded on 20th Jan 2018)

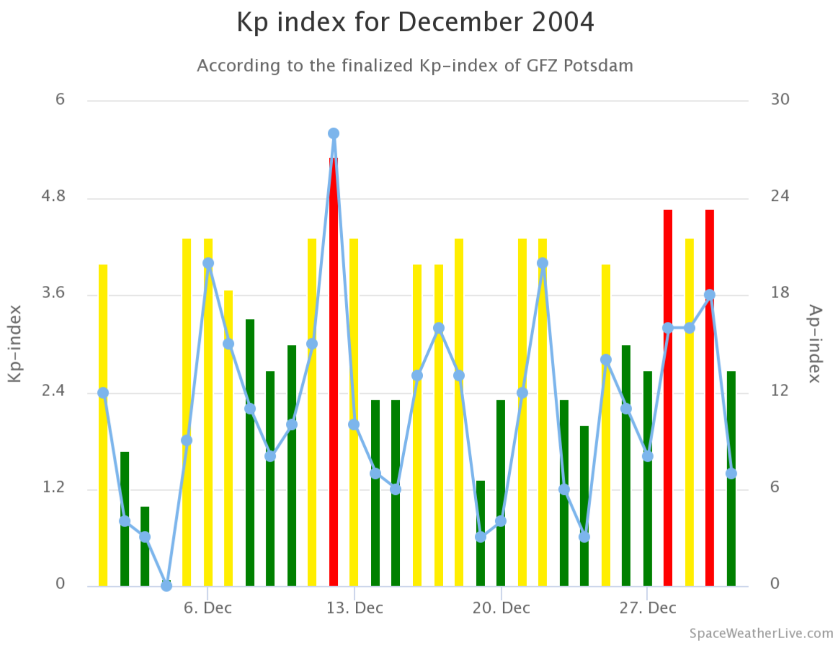

Figure 4.2 Kp index for December 2004

(Page URL: https://www.spaceweatherlive.com/en/archive , downloaded on 20th Jan 2018)

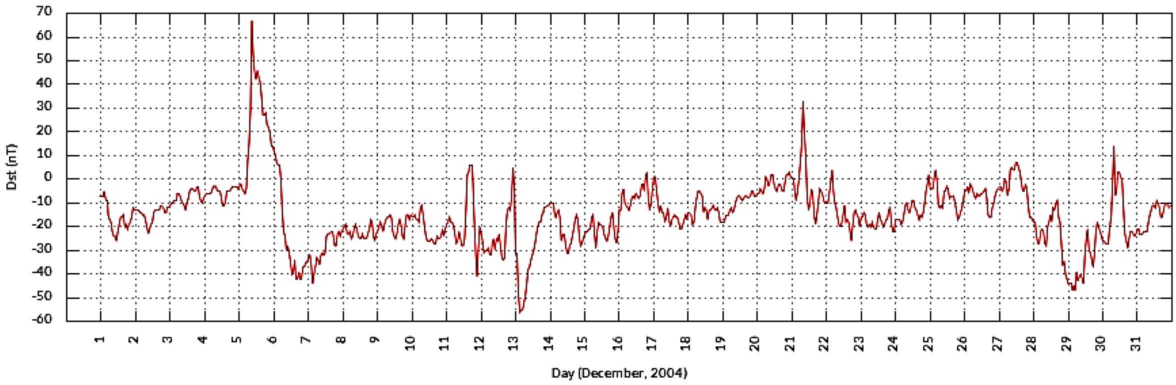

Figure 4.3 Dst index for December 2004

(Page URL: http://wdc.kugi.kyoto-u.ac.jp/dstdir/ , downloaded on 1st July 2018)

Two weeks before the earthquake event on 26th December 2004, the solar flux F10.7 reading was in between 85 to 100, while Kp index recorded a value of less than 5, which signifies only minor solar activity. Dst indices within these two weeks recorded a reading between +20 and -20 nT, which infers low geomagnetic storm activity. There are days in which the Dst index approached -30, but it is still considered a minor activity.

4.3 Observation on Electron Density Profile before the Sumatera-Aceh 2004 Earthquake

Ionosphere electron density, $N_e(h)$, collected from the CHAMP satellite database have been obtained and analysed. The data was collected between 23rd December 2004 until 29th December 2004 during day-time and night-time temporal intervals in the latitude range of -10° and 10° and longitude range of 80° and 110° east. The behaviour of the vertical electron density is found to depend on solar activity events during the day time.

Figure 4.4 shows the variation in the data of ionospheric electron density collected a few days before the major Indian Ocean earthquake, started 21st December to 24th December 2004.

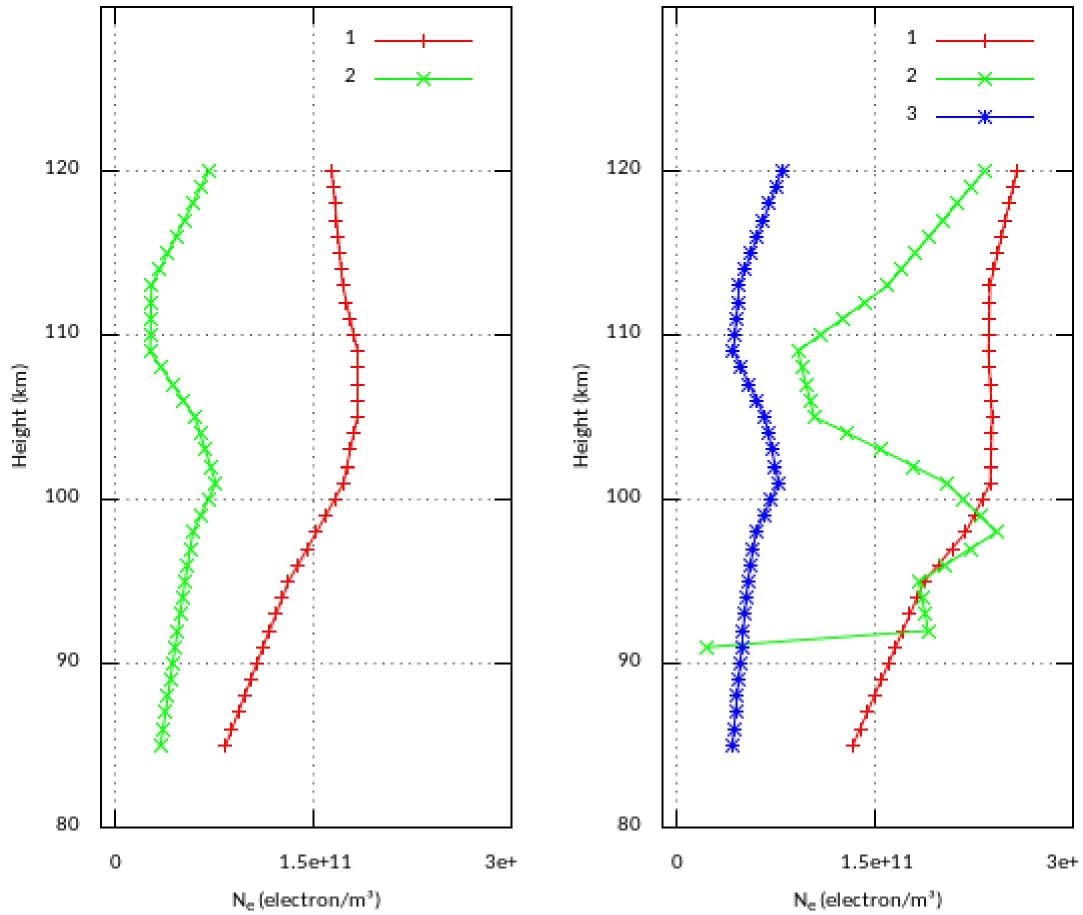

(a) (b)

Figure 4.4: Variations of the electron density a few days before the earthquake. (a) 21st December, 2004 at 13:03 LTC at label 1 and 22nd December, 2004 at 00:35 LTC at label 2, (b) 23rd December, 2004 at 11:00 LTC at label 1, 24th December, 2004 at 00:01 LTC at label 2 and 24th December, 2004 at 23:03 LTC at label 3.

The data collected on 21st December 2004 started on 13:03:35 LTC and end on 13:09:16 LTC at latitude between -1.62˚N and 6.27˚N, longitude 82.74˚E and 74.07˚E with F-layer critical frequency, f_0F2 between 3.1 MHz and 3.8 MHz. While, the data collected on 23rd December 2004, 3 days before the earthquake, started on 11:00:56 LTC and ended on 11:06:03 LTC. The location is in between -6.49˚N, 107.70˚E and 4.42˚N and 99.11˚E with F layer critical frequency, f_0F2 between 3.7 -4.5 MHz. During the local time 11:00, electron density peaked at 2.423 $\times$ 10^{11} $\mathrm{electron/m^3}$, the highest value recorded within a week before the earthquake occurs on 26th December 2004.

In addition, the data of electron density collected on 23rd December at 16:01:33 UTC or 24th December at 00:01 LTC with a frequency between 3.9 MHz to 4.1 MHz shows an distorted profile. This perturbation can be interpreted as one that was possibly seismically-induced due to the pre-earthquake preparation. The set of data labelled ‘3’ in Figure 4.4 (b), collected on 24th December 2004 at 23:03:19 LTC and ended on 23:08:53 LTC, was in quiet condition. The concurrent electron density was measured to be at an average value of 5.96 $\times 10^{10}$ $\mathrm{electron/m^3}$, which signifies an absence of observed disturbances.

Figure 4.5 shows the electron density in the ionosphere on 25th December 2004, a day before the earthquake. At 10:31 LTC, the electron density value was at an average of 1.42 $\times$ 10^{10} $\mathrm{electron/m^3}$and no significant variations were observed. However, at 15:29 UTC or 23:29 LTC, the electron density had increased sharply, reaching an almost maximum value. This was 8 hours and a half before the major earthquake destroyed Aceh that occurred on 26th December 2004 at 00:58 UTC or 08:58 LTC. The data label ‘3’ correspond to the electron density data on 26th December 2004 at 12:33 LTC. At 12:33 LTC, the value of the electron density increased gradually from 9.112×10^{10} electron/m^3 at 90 km to 2.09×10^{11} electron/m^3 at 120 km. This is 12 hours after the earthquake occurred. The lower values of the electron density in the ionospheric heights after the major earthquake suggest the ionosphere has returned into its normal condition.

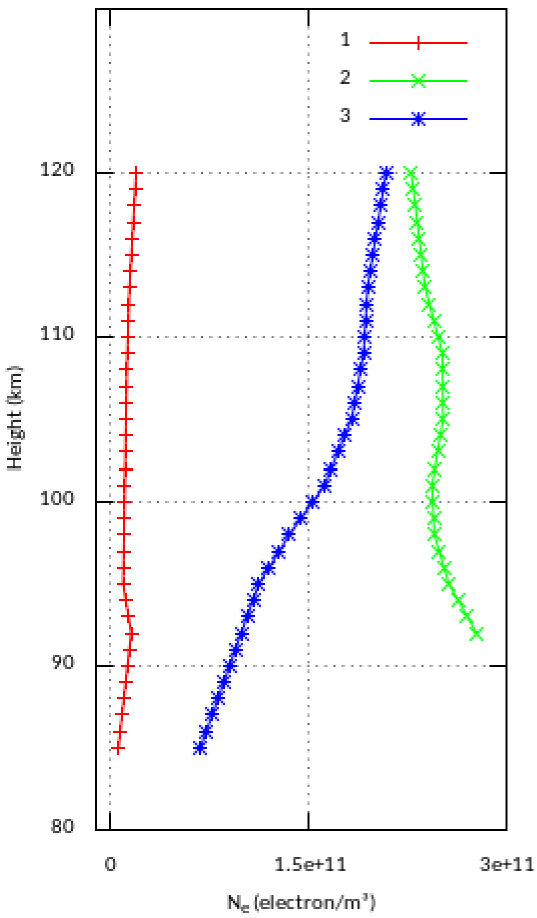

Figure 4.5: Variation in the electron density profile on (a) 25th December 2004 at 10:31 LTC on label 1, at 23:29 LTC on label 2 and 26th December 2004 at 12:33 LTC on label 3.

4.4 The Electron Density Profile from Satellite Source and the IRI Empirical Model

This subsection will report on the comparison between the electron density data collected by the CHAMP satellite (using the radio occultation technique) and that based on the International Reference Ionosphere (IRI) empirical model.

Figure 4.6 displays side-by-side the data of the electron density from the CHAMP satellite database and that from the IRI 2012 model, extracted from 21st December 2004 until 26th December 2004. Within this time span, quiet conditions can be recognized by visually inspecting the occurrence of rigorous variation in the geomagnetic storm and solar flux F10.7 index. From Figure 4.6, the IRI 2012 data shows the value of electron density for all time underestimates the experimental data from CHAMP. However, on 25th December at 10:31 LTC, the IRI 2012 data overestimates the experimental data with large differences.

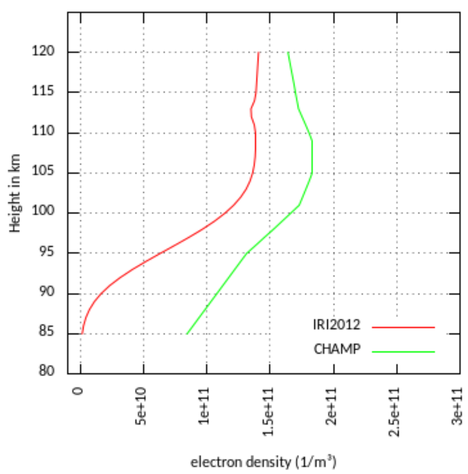

a) 21st Dec 2004, 13:03 LTC

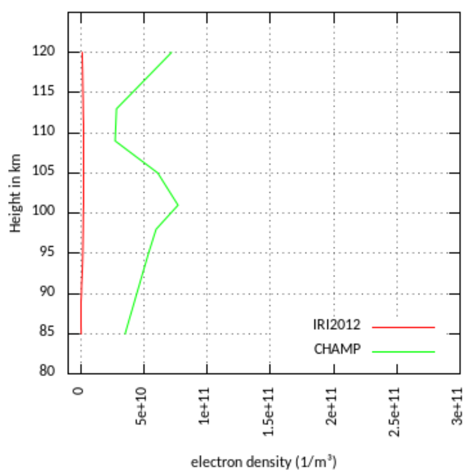

b) 22nd Dec 2004, 00:35 LTC

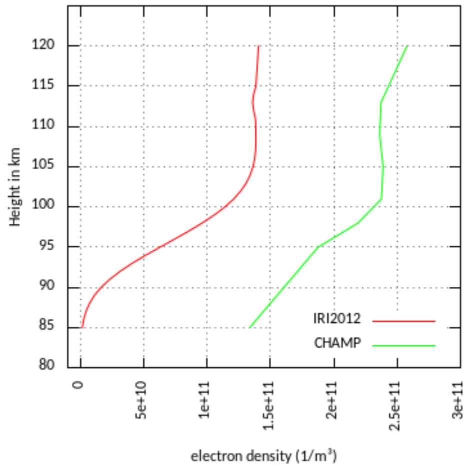

c) 23rd Dec 2004, 11:00 LTC

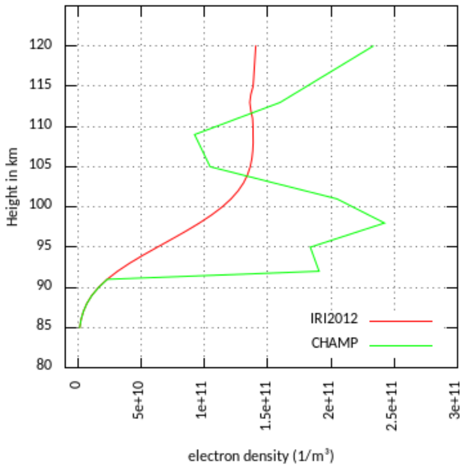

d) 24th Dec 2004, 00:01 LTC

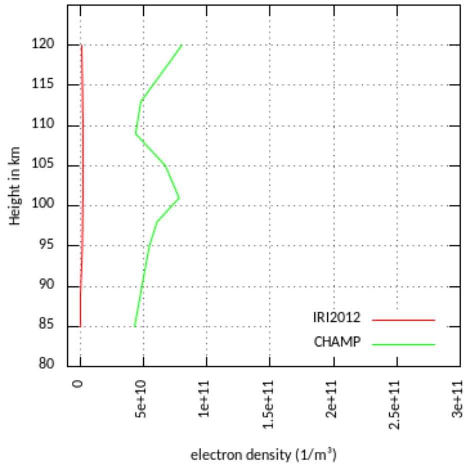

e) 24th Dec 2004, 23:03 LTC

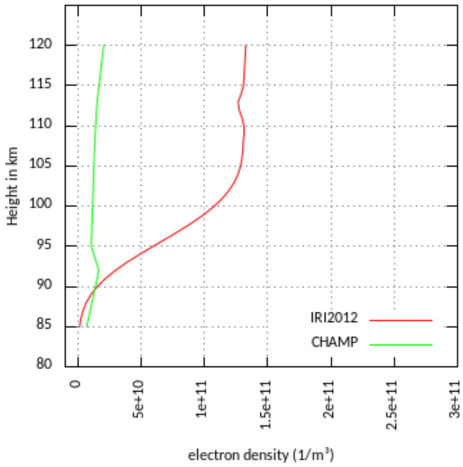

f) 25th Dec 2004, 10:31 LTC

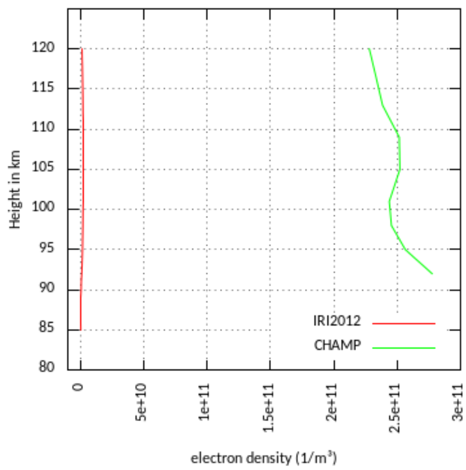

(g) 25th Dec 2004, 23:29 LTC

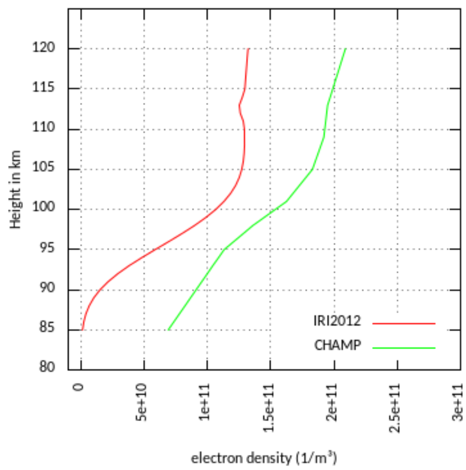

(h) 26th Dec 2004, 12:33 LTC

Figure 4.6: Comparison of the electron density profile by CHAMP satellite and IRI 2012 model.

4.5 Summary

The data for electron density profile was acquired based on the online CHAMP satellite database for 5 days covering the period before and during the event of the earthquake. There are 6 periods of data identified to have a high electron density reading 5 days before the earthquake. There is 1 data on 24th Dec, at 00:01 LTC, the N_e profile is irregular with two peak values. Since solar flux F10.7, Kp and Dst indices show low solar activity and minor geomagnetic storm, the anomalous N_e profile is reservedly interpreted to be closely linked to seismic activity solely and not to solar or geomagnetic activities. Admittedly, more satellite data during low solar activity and minor geomagnetic storm from earthquake events are required before establishing robustly such interpretation. This, however, is practically hindered by the limited availability of accessible satellite data, rendering a larger scale statistical analysis beyond the scope of this thesis. In any case, the present study assumes that the electron density anomaly as observed in the CHAMP data can serve as an input to the FDTD modelling of a proposed earthquake precursor, dubbed ΔQ_s.

The dataset has been compared with that acquired from the IRI 2012 empirical model database for ionosphere. Unfortunately, since the ionospheric data in the South East Asia region is scarce due to the lack of ground stations in this area, IRI2012 data does not supply sufficient data to be applied for the purpose of modelling desired in this thesis.

CHAPTER 5

FDTD ABSORBING BOUNDARY CONDITIONS IN IONOSPHERIC MEDIUM

5.1 Introduction

As mentioned in the last subsection in Chapter 3, implementation of the right ABC is essential in any FDTD simulation. A good ABC should produce as little reflection as possible when the simulated waves impinge onto the edges of boundaries in the simulation grid. In this thesis, the 2-D FDTD code was written in such a manner that an ABC subroutine could be incorporated in a plug-and-play manner. In this chapter, the analysis of the efficiency of the differential ABC and PML for the ionosphere's anisotropic medium as implemented in the FDTD code is reported. The simulations in the numerical experiments to access the efficiency of both ABC were both set to run up to a total of n =2000 iteration. It is to be noted again here that the index n used in the simulation is the time-equivalent variable. So, when one says 'at the time of n simulation step (or 'step') ', it is equivalent to saying 'at the time $t = n\Delta t$'. The active simulation grid dimension is 120 km in the y-direction (vertical) and 600 km in the x-direction (horizontal), with an interval of Δx = 1 km between any two adjacent grid points. The results are discussed as in follows.

5.2 Numerical Experiment with ABC

In the first part of the numerical experiment, the efficiently of ABC is accessed by propagating a 2D spherical wave from the point source located at the origin. The EM wave was time-stepped sequentially in the active simulation grid, and the value of the electric field component E_z was probed, i.e., numerically measured, at selected sites A, B, C, D, E and F, as mentioned in Chapter 3. The locations of the probing sites are A(i = 70, j = 100), B(i = 330, j = 100), C(i = 500, j = 100), D(i = 70, j = 70), E(i = 330, j = 70) and F(i = 500, j = 70), see Figure 3.5. Figure 5.1 visualises the pattern of the simulated EM wave at $n = 2000$ step.

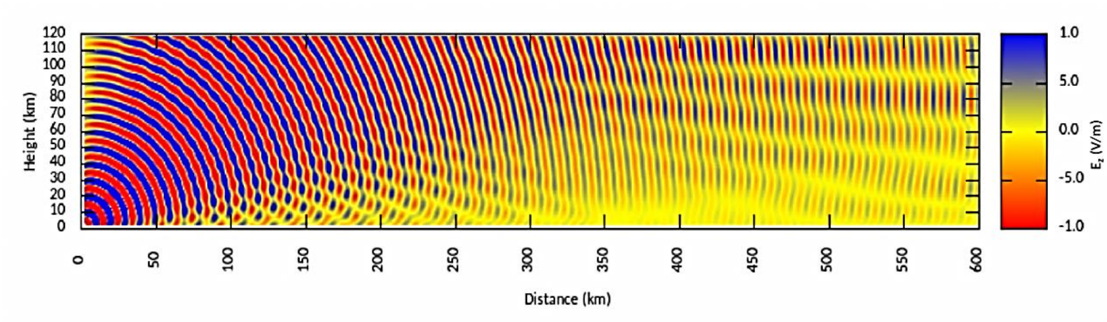

Figure 5.1 E_z field components for ABC after 2000 steps

The relative errors calculated at these points at a particular step n was calculated using Equation (3.38) following the methodology as described in Section 3.4. The results are shown in Figure 5.2, in which the variation in the relative error at each site progresses in simulation time is displayed. As a general observation, the relative errors recorded in Figures 5.2 are all suppressed below a numerical value of 1.00, as would be expected based on the understanding that reflected waves, after they hit the boundaries which are supposed to absorb them to a good extent, should be much suppressed than the incident ones. As EM waves pass through a site before any interference from reflected waves from the boundaries occur, the relative errors should remain zero and flat, which are also clearly displayed in each figure in Figure 5.2. Once reflected waves from the boundaries reach a particular site at some later times, interference with those waves originated from the source and those originated from the surrounding of the site would occur. This shall manifest itself in the forms of a deviation from the flat and zero trend in the relative error vs. step graphs. The first moment of deviation from the flat and zero trends in the relative error graph can be approximately taken as the instance that marks the arrival of non-absorbed waves reflected from the boundaries. For probing sites far away from the point source, EM waves from either the source or reflected from boundaries arrive at a much later stage after the launching of the simulation, resulting in the deviation from flat and zero trend to a much later time. As such, each site has a location-dependent 'on-set instance', some earlier while some later. All these features are expected for such a numerical experiment designed to probe the relative error that measures the inefficiency of the ABC in absorbing EM waves hitting the boundaries.

As a general behaviour in the relative error vs time graphs at all the probing sites measured, it is observed that the initial stage is zero and flat region, corresponding to the absence of interference due to the arrival of unabsorbed waves from the boundaries. When interference from the unabsorbed waves arrive, the graphs gradually deviates from the zero and flat region via a sort of short transition of roughly 50 – 150 simulation steps into what shall be dubbed as a 'steady state'. In this state, the relative error oscillates periodically at a frequency of the EM wave at amplitude that is more or less constant over an extended period. The amplitude may after some extended period undergo a transition to a larger or smaller value. In principle, one can measure the amplitude of the relative error in the steady state in every point in the simulation grid, but due to practical consideration, we can only measure these amplitudes at some representative sites, such as that being done here. The maximum amplitude of the relative error in the steady state throughout the simulation is a conservative indicator of the error in the accuracy of the current FDTD simulation of EM wave propagation in the ionosphere.

The relative error at site A reaches the periodically steady stage after 1350 steps, almost constant at below 4×10^{-1}. At site B, the relative error decreases after 950 simulation steps, constantly less than 2×10^{-1}. At site C, the amplitude of the relative error at the beginning is high, more than 4×10^{-1}. At a later time, i.e. after 1430 steps, the amplitude decreases to less than ~3×10^{-1}. The amplitude of the relative error at site D is similar to that in site A, but with a value of less than 3×10^{-1}, and reaches steady state condition after 1350 steps. The reflection errors in site E shows a profile where it increases at a late time, i.e., after 1470 steps, and the steady-state amplitude is below 4×10^{-1}. At site F, the error rise from zero after 1650 steps and the steady state amplitude is the highest among all sites, $\sim 4.6 \times 10^{-1}$.

Figure 5.2(g) displays collectively the relative error at sites A-F. To illustrate the difference of the interference effects at different sites, one can compare the relative error trend at site D (which is closest to the point source) to that for site C (the furthest from source, yet closer to the reflecting edges at the top right corner). It is observed that the relative error at site C is relatively larger because the reflection from the top right corner is more pronouncedly felt at site C than at site D.

This ABC absorbs the wave at the boundary without PML. We can observe that if we use Δt as in equation (3.23), since the field travels at the speed of light, c_0, in one time step the, field will travel only half a cell. This means that to entirely cross one cell, two time steps are necessary. In anisotropic condition and dielectric present, the speed of propagation is not equal to c_0. This is the reason major reflection observes and high relative error calculates.

The most important take-home information that is derived from the trends of the relative error graphs at these probing sites is that, the relative errors in the EM propagation simulation originating from the inefficiency of the ABC, despite being periodically oscillating, remains constant in amplitude (with a maximum value of less than ~0.5, see Figure 5.2(g)) throughout the entire simulation period, $n_{\max} = 2000.$ The relative errors appear to not grow beyond the critical value of 1.0 over time. This appears to be a desirable stable-state trend. We anticipate such benign trend to persist even for a larger value of $n_{\max}$. This implies that numerical errors in the present FDTD code for EM propagation in the ionosphere is capped and do not grow beyond an uncontrollable limit as the waves are stepped in time if the simulation period is of the order of $n_{\max}$ ~ a few 10^3 steps or smaller.

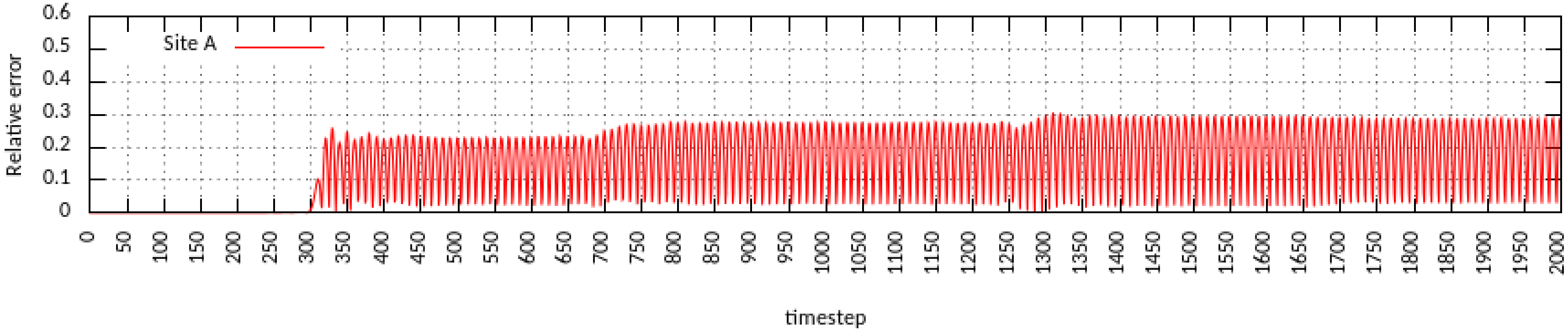

Figure 5.2(a) Relative errors at site A within 2000 time-steps using ABC

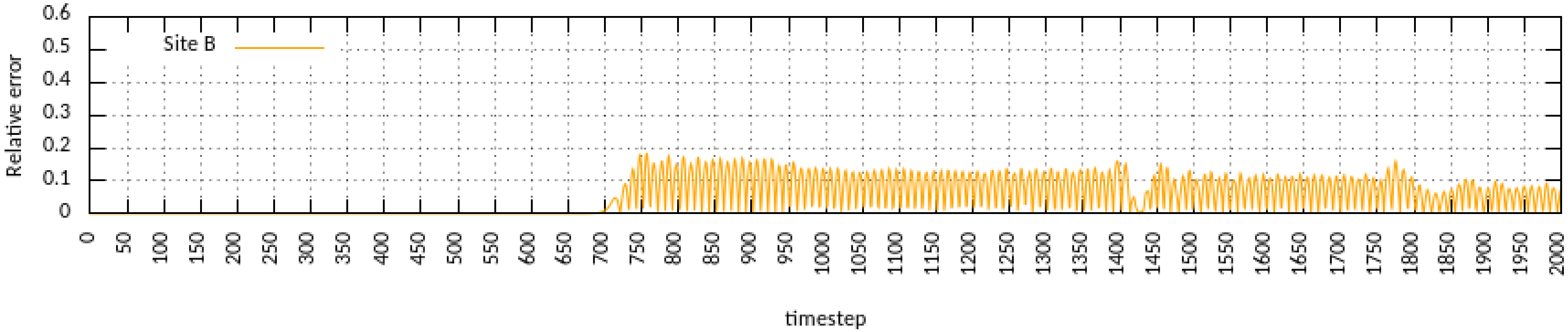

Figure 5.2(b) Relative errors at site B within 2000 time-steps using ABC

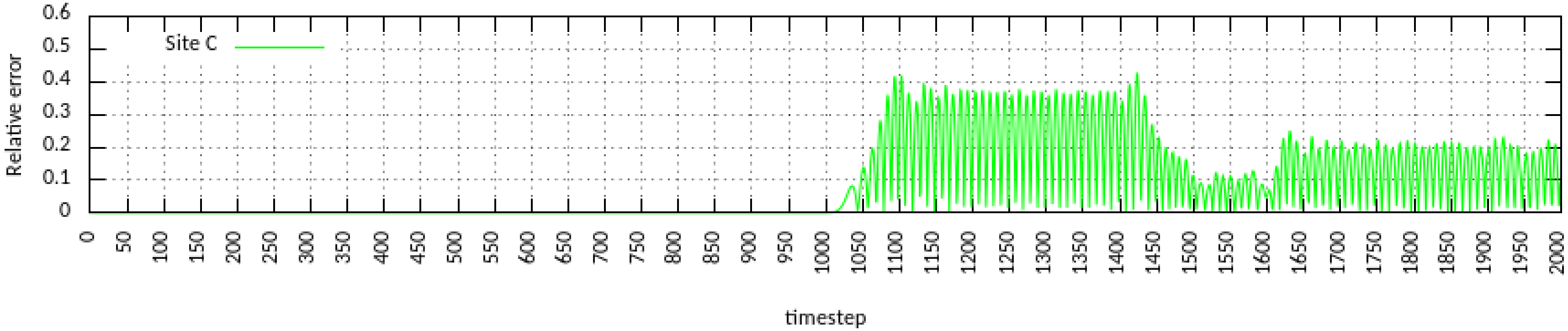

Figure 5.2(c) Relative errors at site C within 2000 time-steps using ABC

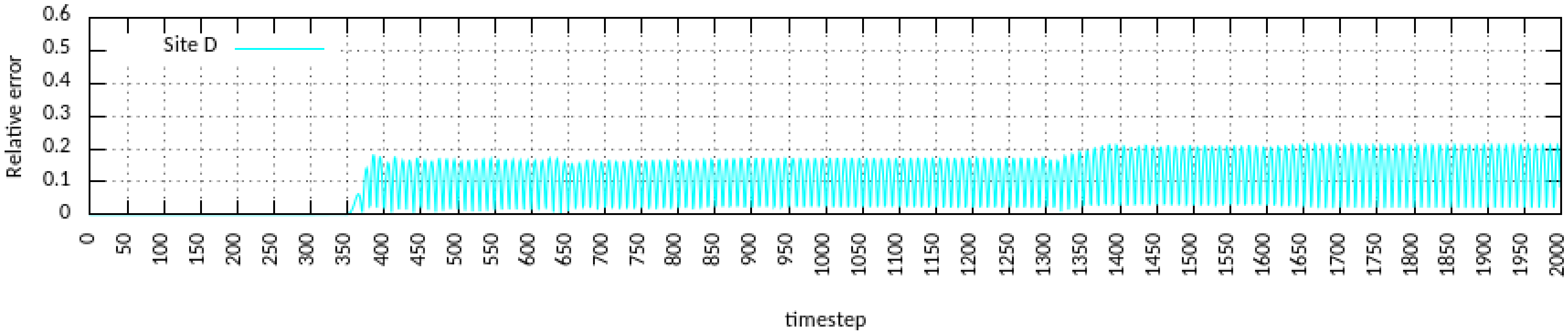

Figure 5.2(d) Relative errors at site D within 2000 time-steps using ABC

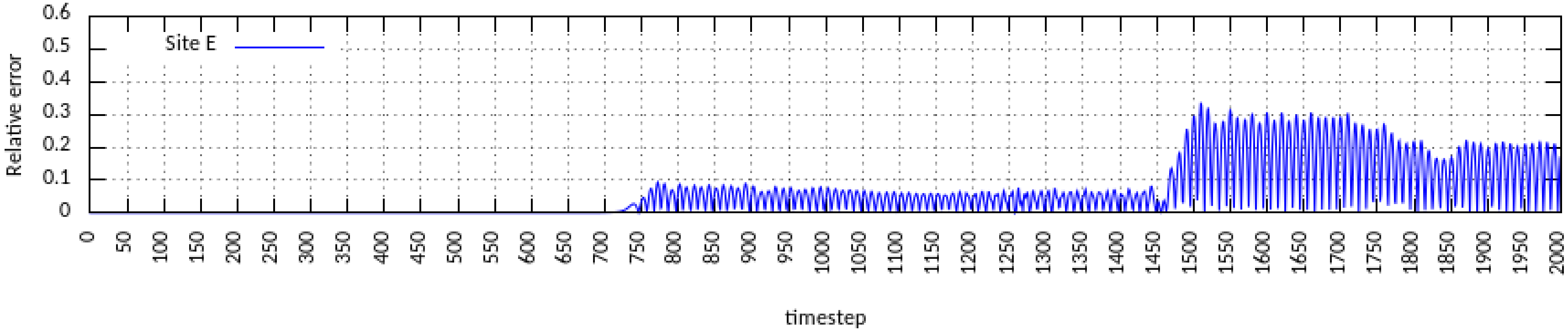

Figure 5.2(e) Relative errors at site E within 2000 time-steps using ABC

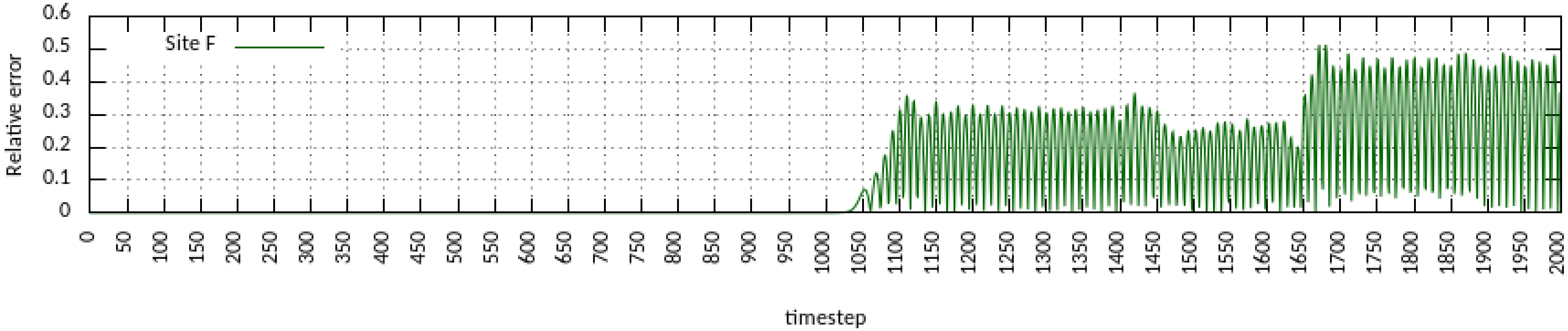

Figure 5.2(f) Relative errors at site F within 2000 time-steps using ABC

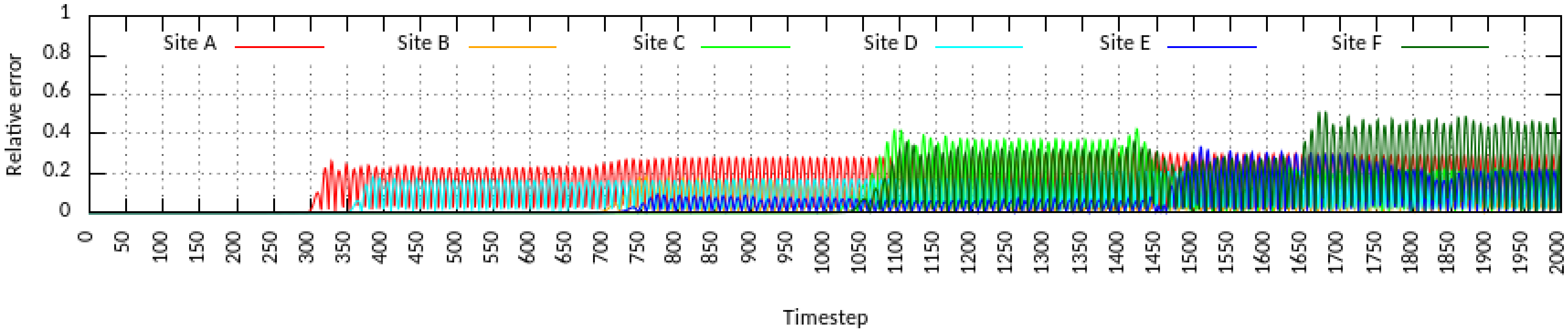

Figure 5.2(g) The grouping of all sites

5.3 Numerical Experiment with Perfectly Matched Layer (PML)

In this subsection, the results for the numerical experiment on the efficiency of the ABC based on the PML method by J.-P. Berenger (1994), as already introduced in Chapter 3, will be presented. The method shall be referred simply as 'PML' or just 'PML' hereafter.

The set-up of this experiment is the same as that for the differential ABC in the previous section. However, the outer perimeter of the active simulation grid in this experiment is now surrounded with a PML layer of width $\mathrm{w} = N_{\mathrm{PML}}\Delta x$, where dx is a spatial grid. The efficiency of the PML will be measured for varying thickness of the PML layer by adjusting N_{PML}.

As an illustration, Figure 5.3 visualises the pattern of the simulated EM wave at $n = 2000$ step for the case of PML with a layer thickness of $w = 25\Delta x$. Or in other words, this is a PML with a thickness of $N_{\mathrm{PML}} = 25$ cells.

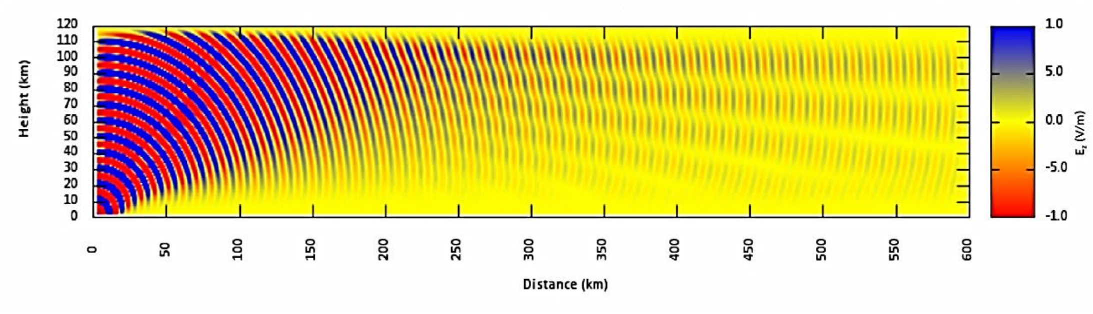

Figure 5.3 E_z field component for 25 cells of PML after n =2000 steps.

The relative errors for the field component E_z probed at the various sites for the case with a thickness $N_{\mathrm{PML}} = 25$ are shown in Figure 5.4(a-f). The immediate feature in Figures 5.4 is the extreme suppression of the relative error at sites A and D. Besides, similar to the previous numerical experiment for differential ABC; the relative errors are also observed to be less than the critical value of 1.00 in all cases. At the site B and E, the relative errors reach a steady state after 730 steps with a relative error less than 3×10^{-1}. At sites C and F, the steady-state relative errors reach a relatively higher value after 1070 time-steps, namely, $\sim 4.3 \times 10^{-1}$ and $\sim 5.5 \times 10^{-1}$ at sites C and F respectively. In fact, the relative error at site F is the highest among all sites in both experiments (differential ABC and PML with $N_{\mathrm{PML}} = 25$).

Figure 5.4(g) displays in a collective manner the relative errors at all sites for this case, i.e., PML with $N_{\mathrm{PML}} = 25$. Among all sites, site F displays the largest relative error, while the relative errors at sites A and D are the most suppressed, due to their locations that are situated furthest from the PML edges. There is no adjustable parameter that can be used to alter the performance of the differential ABC. However, in the case of PML, it is yet to see whether the relative error can be further suppressed in by varying the thickness of the PML layer, N_{MPL}. In the following section, the performance of PML as a function of N_{MPL} is reported.

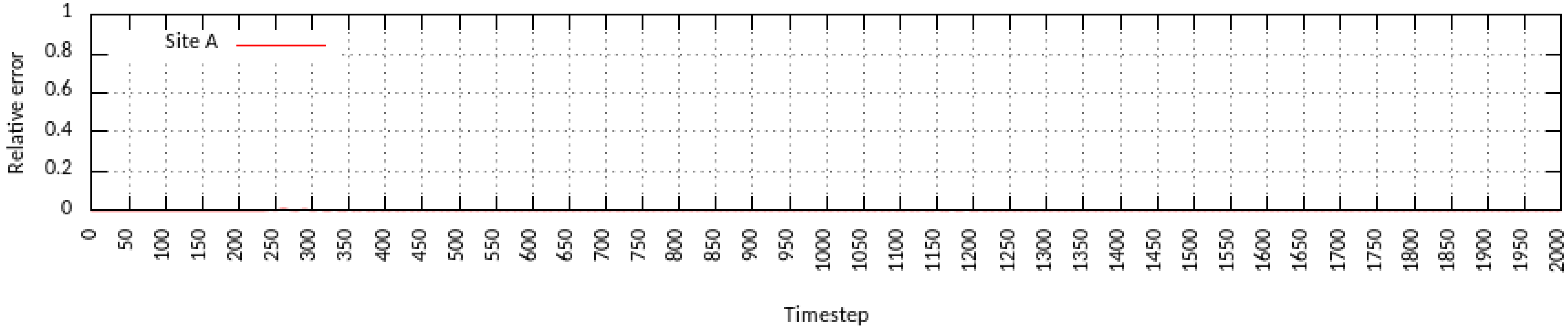

Figure 5.4(a) Relative error at site A within 2000 time-steps using Perfectly Matched Layer.

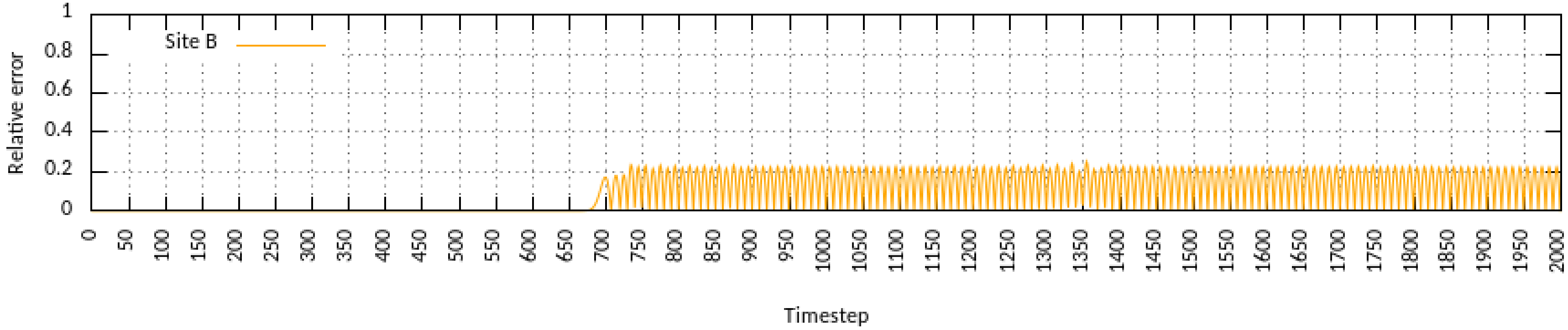

Figure 5.4(b) Relative error at site B within 2000 time-steps using Perfectly Matched Layer.

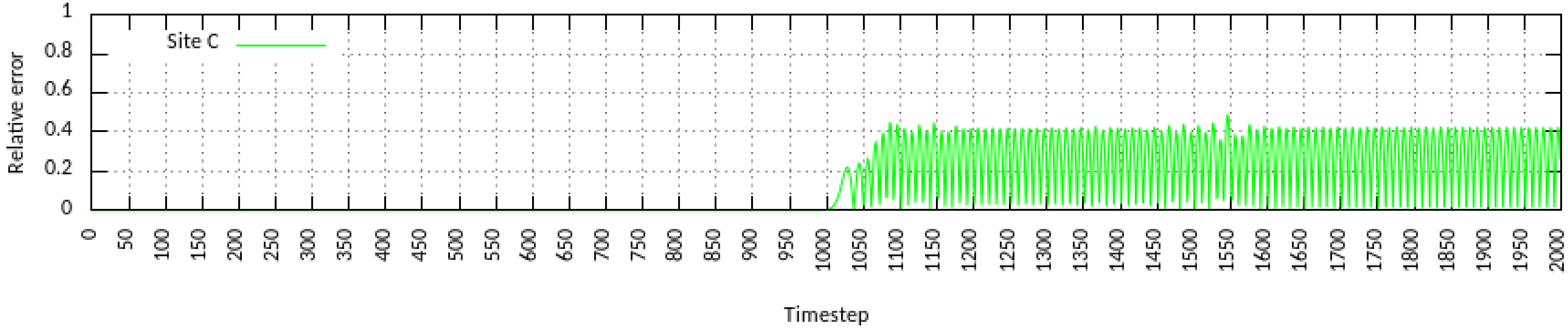

Figure 5.4(c) Relative error at site C within 2000 time-steps using Perfectly Matched Layer.

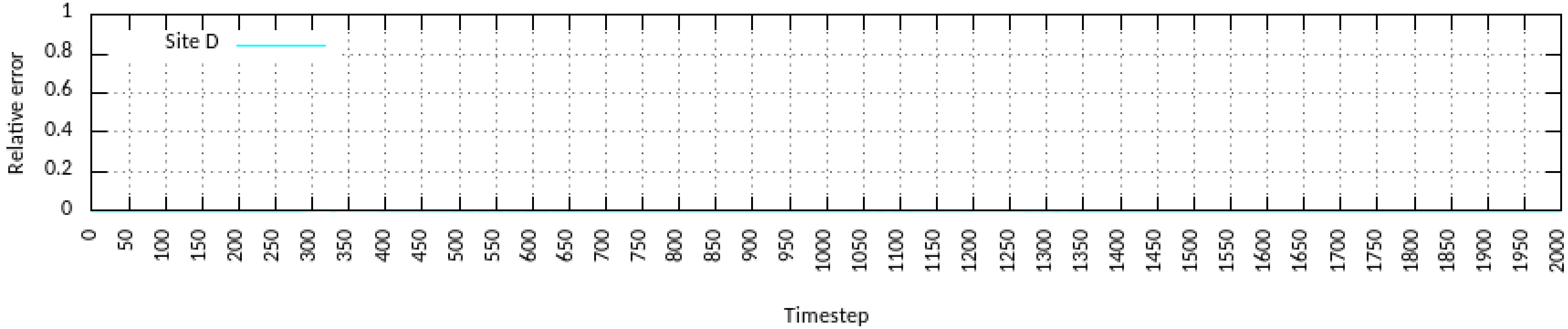

Figure 5.4(d) Relative error at site D within 2000 time-steps using Perfectly Matched Layer.

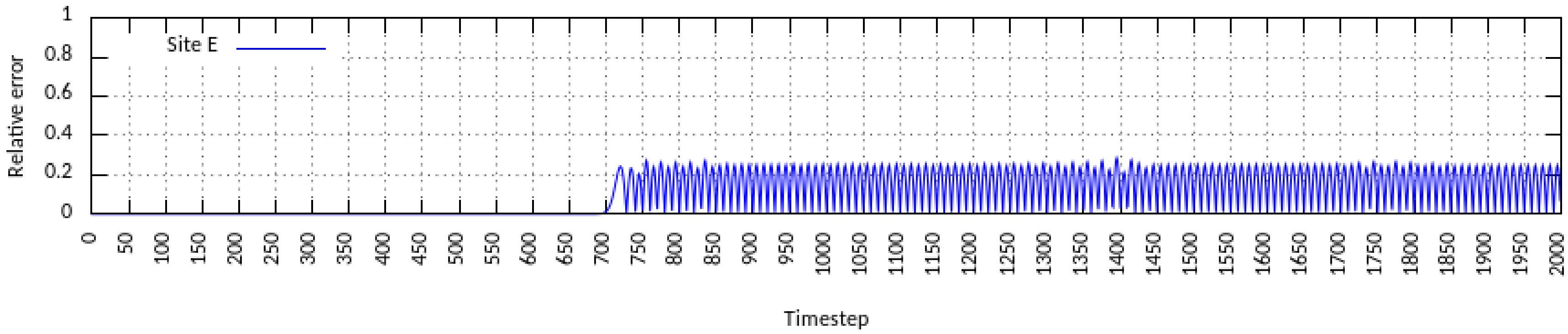

Figure 5.4(e) Relative error at site E within 2000 time-steps using Perfectly Matched Layer.

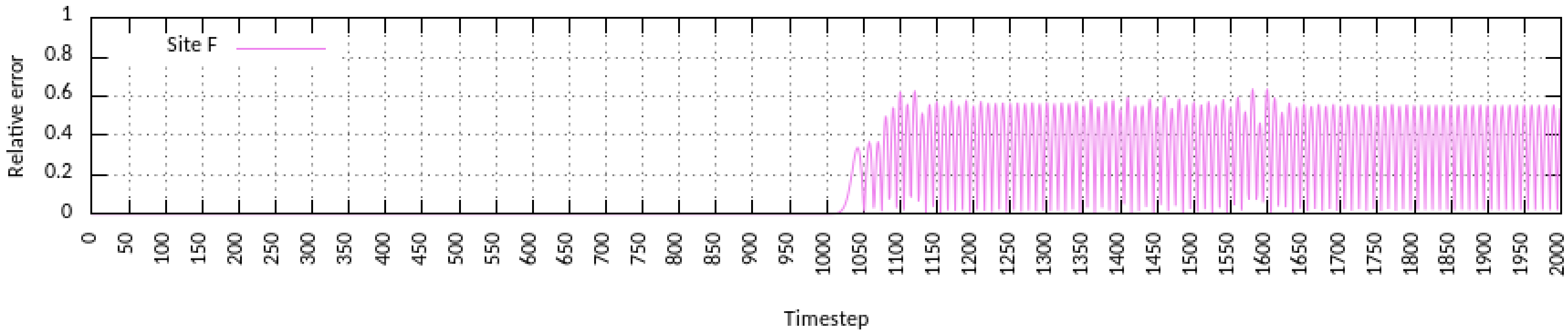

Figure 5.4(f) Relative error at site F within 2000 time-steps using Perfectly Matched Layer.

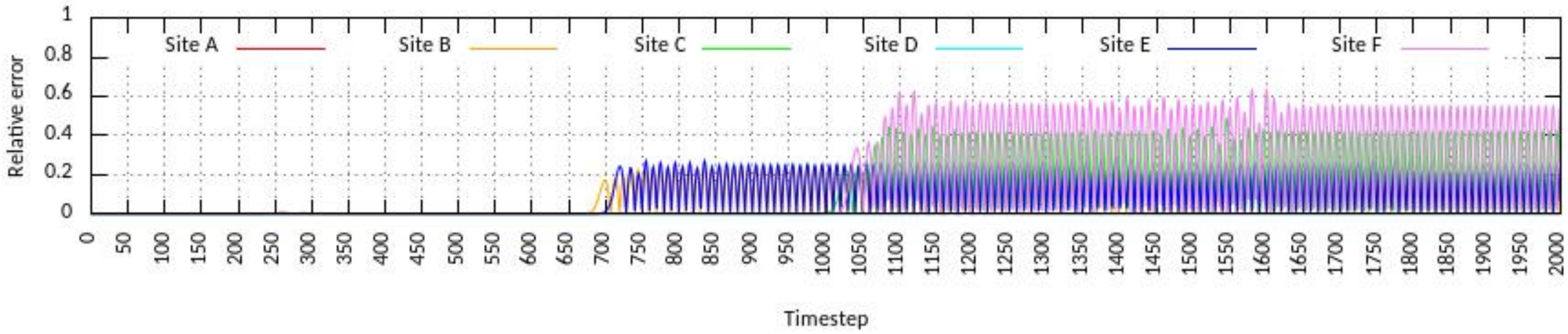

Figure 5.4(g) The grouping of all sites.

5.4 Performance of PML with Varying Thickness

In this subsection a numerical study on the variation of the efficiency of PML with different thickness $N_{\mathrm{PML}} = 5, 10, 15, 20, 25$ will be carried out. The purpose is to see whether increasing the thickness of the PML layer will lead to any desired improvement in the suppression of the relative error. The measurement of relative error of E_z will be carried out only at one selected site, i.e. site F (i = 500, j = 70). This site is chosen because the relative error was measured to be the largest among all sites in the numerical experiments for both ABC schemes. The relative error measured at site F is hence to be interpreted as the maximum possible error in the present FDTD code. The actual global relative error for the FDTD code should be lesser than the conservative error as measured at F. Figure 5.5 shows the relative error at site F for 5, 10, 15, 20 and 25 cells of PML at 2000 steps.

The relative error at site F for $N_{\mathrm{PML}} = 5$ at steady state condition after 1790 steps is ~ 1.2, as reported in the previous subsection. The relative error measured in the case for $N_{\mathrm{PML}} = 10$ at steady state condition, ~ 1, is reached after 1650 steps. The relative error for the $N_{\mathrm{PML}} = 15$ case is around $\sim 8 \times 10^{-1}$ in the steady state, whereas the values are $\sim 7 \times 10^{-1}$ and $\sim 6 \times 10^{-1}$ for the $N_{\mathrm{PML}} = 20$, 25 cases respectively.

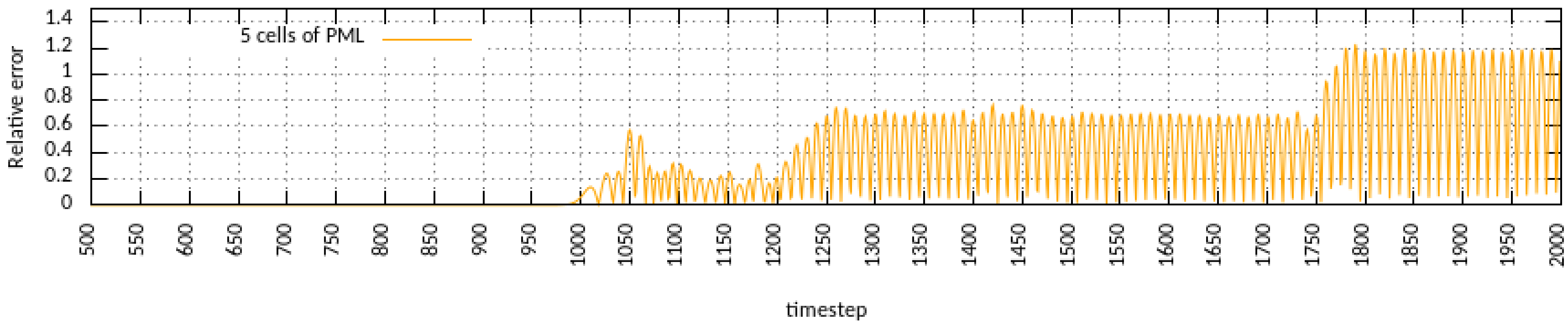

Figure 5.5(a) Relative errors at site F for 5 PML cells at 2000 time steps.

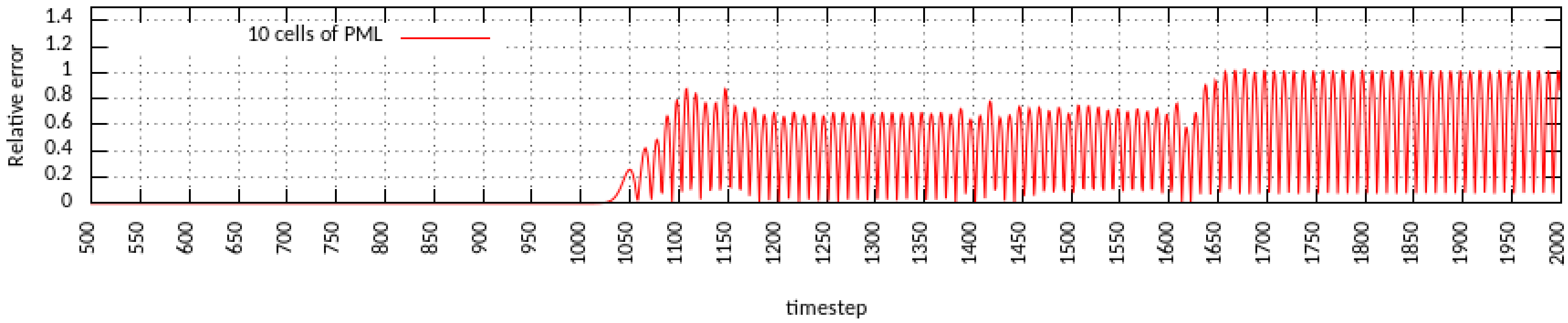

Figure 5.5(b) Relative errors at site F for 10 PML cells at 2000 time steps.

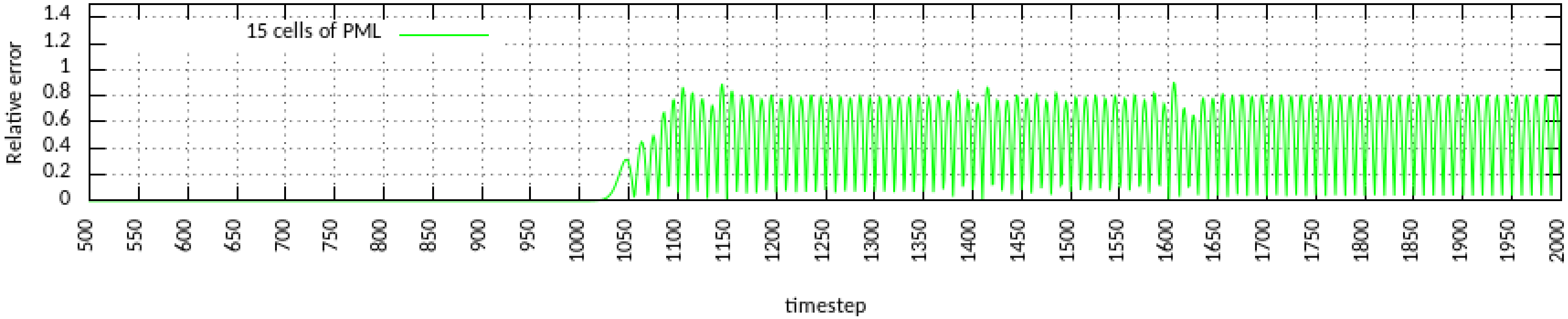

Figure 5.5(c) Relative errors at site F for 15 PML cells at 2000 time steps.

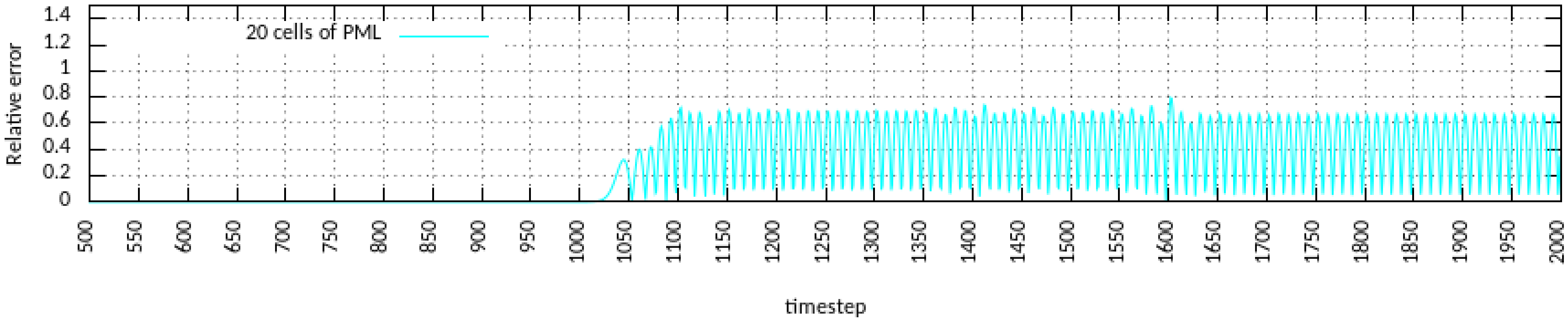

Figure 5.5(d) Relative errors at site F for 20 PML cells at 2000 time steps.

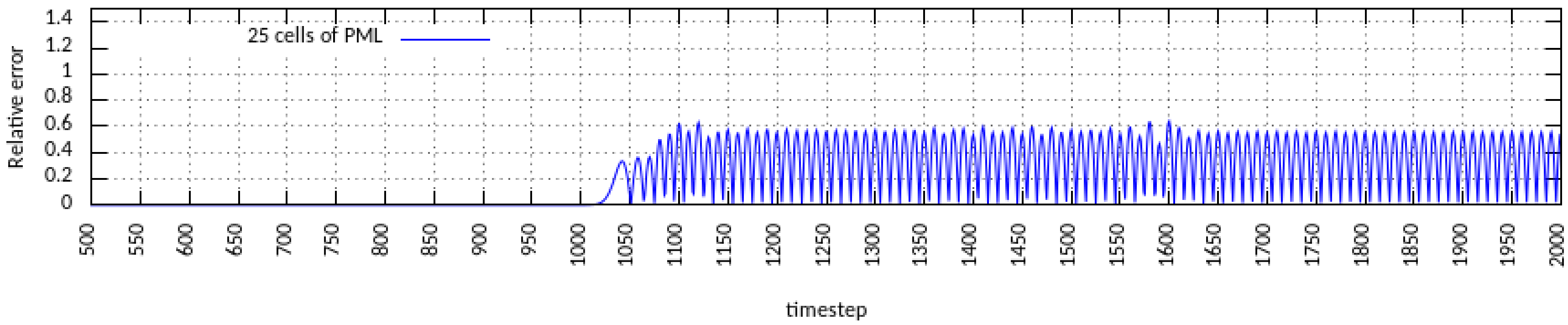

Figure 5.5(e) Relative errors at site F for 25 PML cells at 2000 time steps

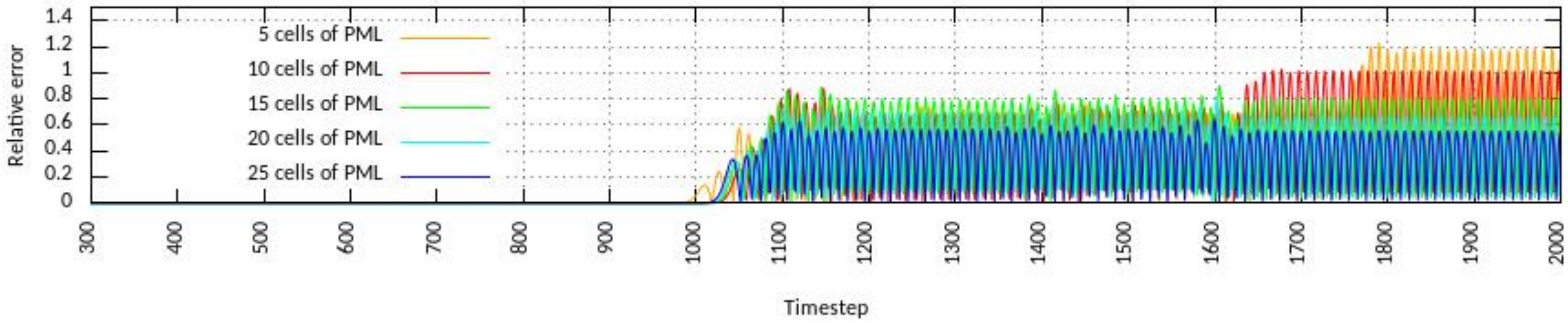

Figure 5.5(f) Grouping of all relative errors.

Figure 5.6 summarizes the performance of the FDTD code in error absorption using PML with different N_{PML} in the ionospheric medium. The trend on the plots shows that a slight reduction in the largest steady-state relative error is obtained as N_{PML} increases in general.

Comparatively speaking, the performance of the PML is almost the same as the differential ABC in terms of the largest steady-state amplitude at site F, namely, $\sim 6 \times 10^{-1}$. However, if averaging over all sites, the overall relative error in the PML would be lower than that of the differential ABC as there are sites in the PML case where the relative error is significantly suppressed, but no such site-specific suppression is measured in the differential ABC case. Taken into consideration of the site-selected error reduction, PML is considered better in error reduction as compared to differential ABC. However, to make a robust claim that the PML is in overall better than the differential ABC, it requires stronger evidence. This can only be obtained via a more thorough numerical measurement and analysis which are beyond the scope of this thesis. Ideally, the relative error should be suppressed to as much as it possibly can.

Unfortunately, based on the results from the numerical experiments conducted, the upper limit to the largest relative error is capped at $\sim 6 \times 10^{-1}$, which is not an impressive figure. Anyway, as long as the time-stepping of the FDTD code is not running for an excessive number of steps, i.e., not too much exceeding $n_{\max} \sim 2000$ steps, the error in the EM propagation simulations should be well contained. To assure that the error from the PML, which will be made the ABC of choice in simulating the EM wave propagation in the ionosphere in this thesis, is well under control, an independent verification test on the fidelity of the FDTD code shall be performed and reported in the following section.

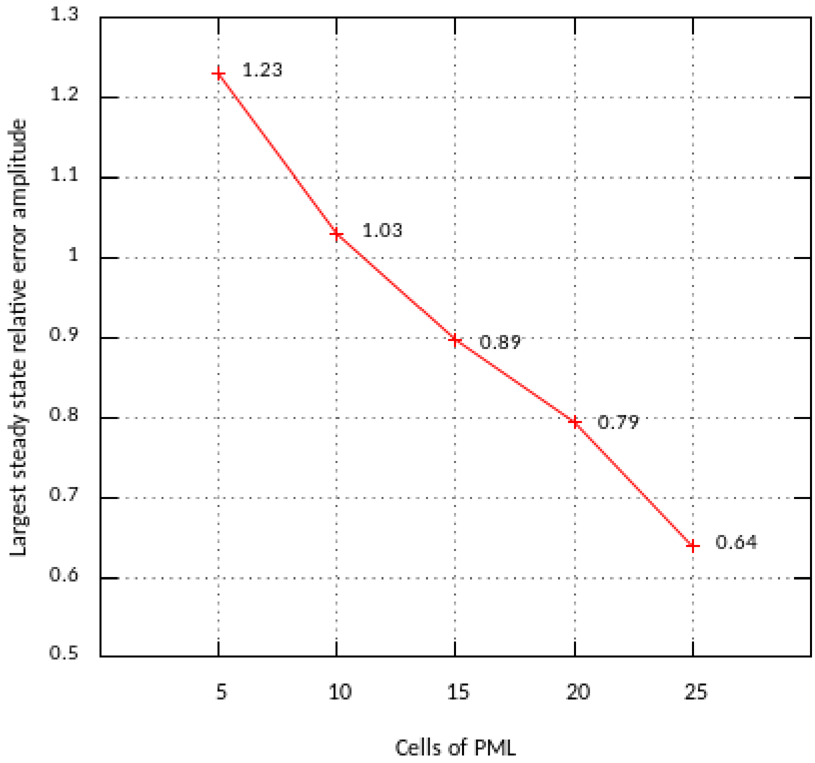

Figure 5.6 The values of relative error amplitude at a thickness $N_{\mathrm{PML}} = 5, 10, 15, 20, 25$ in the PML implemented in the anisotropic ionospheric medium at site F.

5.5 2D FDTD Code Verification

In this independent numerical experiment, a site at the site i = 500, j = 4, which is located near to the Earth surface, is chosen so that the FDTD simulated electric field is measured there. The EM waves at this site are measured in three separate medium environments. The first is a free space condition where no electron density profile enters the FDTD simulation. The second is a medium environment with electron density profile calculated from the theoretical Equation 3.4 as mentioned in Chapter 3. In the third experiment, the experimental (CHAMP satellite) electron density profile is used in the FDTD simulation. The data is from 21st December 2004 at 13:03 LTC. These numerical experiments are conducted with the intention to observe the sensitivity of the codes with and without the presence of electron density profile.

Figure 5.7 shows the plots obtained for these three experiments at the site i = 500, j = 4. Since from 0 to 1000 time steps the wavefront not reached the observation site yet, we can only observe the straight line. The measured wave in all three experiments oscillates sinusoidally as expected. The amplitude of electric field in free space is higher, in the range of 10^{-5} V/m while comparing with the anisotropic condition the range is of 10^{-7} V/m. This is an assuring feature as the EM wave in a dispersive medium such the ionosphere should dissipate energy from the EM waves. The time when the transient field arrives at the observation point is identified to the same, but the transient field for the respective electric field in free space and the anisotropic condition is not. The electric field in free space reaches steady states as early as n =1100 but for the anisotropic condition, it is n =1120. In addition, the magnitude for the electric field in anisotropic with theoretical electron density profile observed to be small compared to electron density profile from experimental. The behaviour of the electric field confirms that the FDTD code is sensitive to the change in electron density profile.

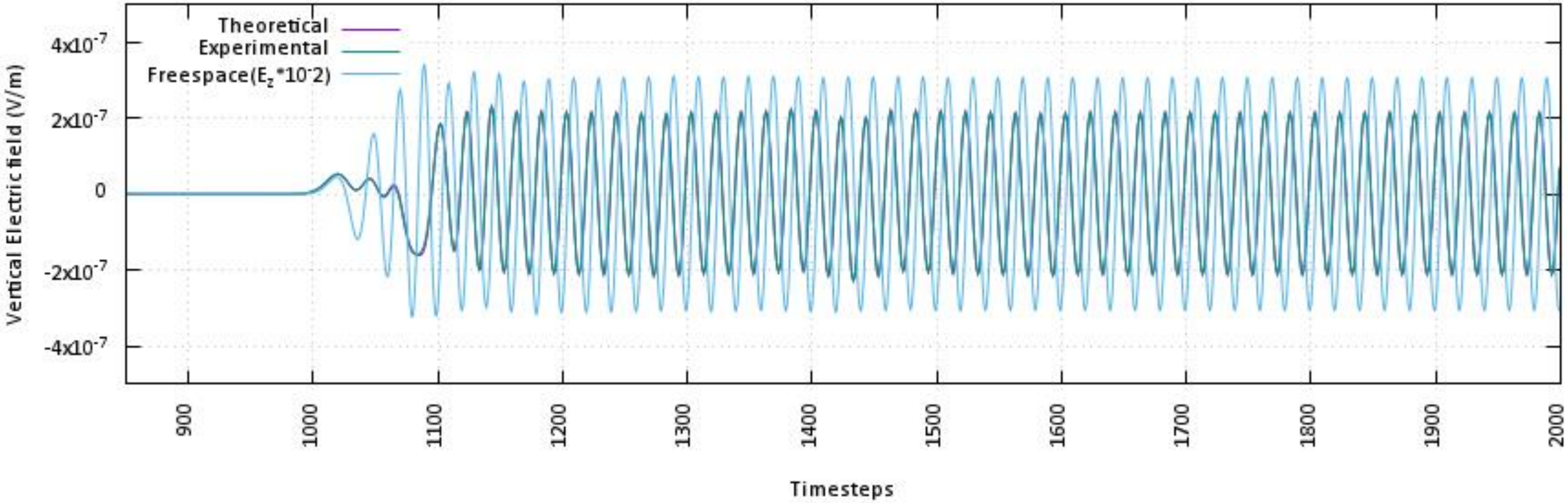

Figure 5.7 Vertical Electric field for free space and anisotropic condition probe at site 2 (i = 500,j = 4)

5.6 Summary

In this chapter, a numerical study to quantify two types of ABC, namely, for differential ABC and PML, implemented in the FDTD code developed for dispersive, anisotropic medium, have been conducted. The relative errors of the EM fields at a set of selected sites are measured. The largest relative error among the probing sites, which occurs at the site F, is found to be of the order 6×10^{-1}, albeit the overall averaged errors caused by the reflected waves could be smaller than this value. The relative error at site F measured using differential ABC and PML with different thickness has been compared. This is done by examining the variation of the PML efficiency as a function of thickness, $N_{\mathrm{PML}} = 5, 10, 15, 20, 25$. The results of the comparison shows that increasing the number of PML thickness generally suppresses the relative error by as much as 48% as compared the suppression efficiency of using only 5-cell PML. Finally, the numerical experiment to examine the sensitivity of the codes on electron density profile is carried out. The electric field in free space is observed to reach steady state earlier than the anisotropic, dispersive case. In addition, the magnitude for the electric field in anisotropic observed smaller than free space.

As a conclusion, the numerical experiments carried out in this chapter appear to display minimum absorption efficiency in both types of ABC, albeit not to an impressive extent. In addition, the 2D FDTD codes display the desired sensitivity on the electron density profile as expected. In this experiment, the propagation of EM fields is simulated using three different atmospheric media, namely, free space, space filled with $N_e(h)$ measured from the CHAMP data, and $N_e(h)$ calculated based on the theoretical equation defined in Equation (3.4). These numerical results establish the confidence to deploy the 2D FDTD code in a full-fledge simulation of the EM wave propagating through the ionosphere as a means to simulate an earthquake precursor. This will be reported in the next chapter.

CHAPTER 6

ELECTROMAGNETIC WAVES PROPAGATION IN LOCAL IONOSPHERE

6.1 Introduction

In this chapter, the electromagnetic waves, specifically the electric field component E_z are simulated using the 2D FDTD developed in this thesis based on the methodology as already discussed in Chapter 3. The FDTD implementation neglects the Earth curvature, which is a feasible approximation given the fact that the Earth's radius is of the order 4200 km. The active simulation grid has a dimension of 120 km × 600 km, in which a spatial resolution of $\Delta_x = \Delta_y = 1$ km was adopted. The ABC implemented is PML, with $N_{\text{PML}} = 25$. Time increment Δt is set to a value of 1.6×10^{-6} s and conforms to the Courant numerical stability requirement. The transient field of the reflection wave was numerically measured at three sites; site 1 (i = 30, j = 4), site 2 (i = 300, j = 4) and site 3 (i = 500, j = 4). The location for origin (i = 0, j = 0) is assumed to be in Indian Ocean earthquake 2004 epicentre which is 3.316° N, 95.854°E. All sites are sketched in Figure 6.1.

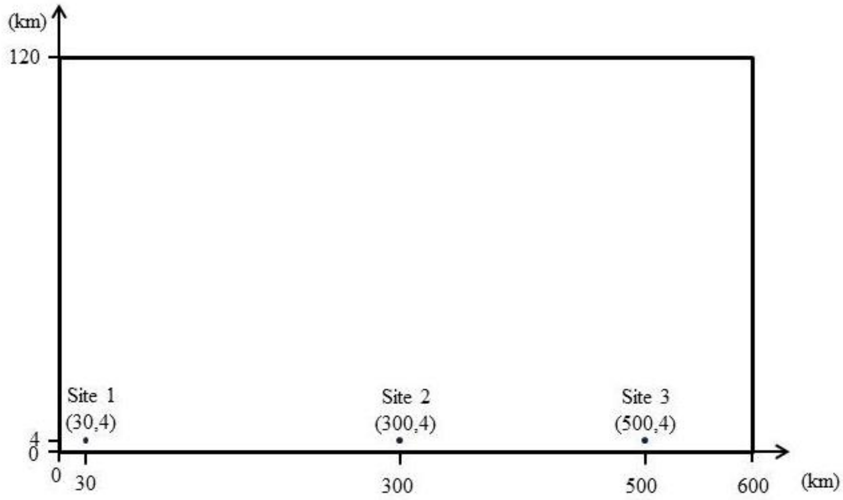

Figure 6.1 The location of sites 1, 2 and 3 in the computational grid.

These sites are selected to represent three locations near to the ground level that are at a distance of 30 km, 300 km and 500 km from the point source. The simulated results at these three observation sites mimic what a radar receiver would have recorded from an EM point source with a fixed frequency $f_0 = 30$ kHz. The transient EM waves at these sites arrive continuously and are 'recorded' in every single step n throughout a simulation run. Embedded in these recorded transient values are information about the histories of interactions the EM waves had gone through during the course of their propagation in the atmosphere, from the point source to the measurement sites. Since electron density in the ionosphere effect the electromagnetic propagation in a very profound manner, as per the governing rule of the Maxwell's equations for anisotropic, dispersive medium, one expects to observe certain deviation in the transient field when the electron density profile is drastically perturbed due to strong seismic activity. Comparing the simulated transient fields based on electron density data taken before, during and after the 2004 Indonesian earthquake, the presence of possible precursor effect is expected to manifest itself. The finding of such a precursor effect based on satellite data obtained during the 2004 earthquake, which is also the most important novelty of this thesis, is the main theme of this chapter.

6.2 Analysis of the Transient E_z Component in the Presence of N_e based on Satellite Data

As discussed in Chapter 4, the data of electron density were extracted from the CHAMP satellite database. Figure 6.2 depicts the transient E_z field in the free space condition. This will be later be used as a reference field for comparison purpose when interpreting the simulated results. Figure 6.3 (a) to Figure 6.3 (h) show the numerically measured transient E_z field in the present 2D FDTD simulation recorded at sites 1,2 and 3 at the date and time as indicated. Each of these figures displays some common features as follows. It is observed that the evolution of the EM field at a site can be approximately divided into three temporal stages. Before the EM waves arrive, the graphs in these figures remain flat. Upon the arrival of the EM wave, the graphs begin to deviate from the flat line to undergo a transition period of fluctuation before entering a steady state. At site 2, after 730 time steps, there is a deviation can be observed in all figures. This condition happened due to the interference with the medium and shows in the waves shape when reaching the observation sites. The same condition can be observed in sites 3 for all figures after 1070 time steps.

In the time domain approximately given by the condition $n\Delta t c_0 < 90$ km, the transient E_z component recorded at any given site is produced primarily by the point source. No contamination from reflected waves (which are bounced from the computational boundary) is expected in the active simulation grid region, as the EM waves have only travelled a distance much less than 120 km (i.e., the vertical distance from the source to the upper boundary of the simulation grid). Additionally, in this time domain, the altitude covered by the EM waves from the source is less than 90 km, where electron density in the atmosphere is very low. Reflection of the EM waves due to interactions with the medium at an altitude below 90 km hence is relatively weak as compared to the case at higher altitude. At higher altitude (90 – 120 km), transient E_z field component will be generated through stronger anisotropic and dispersive effects due to a high electron density in the atmospheric medium.

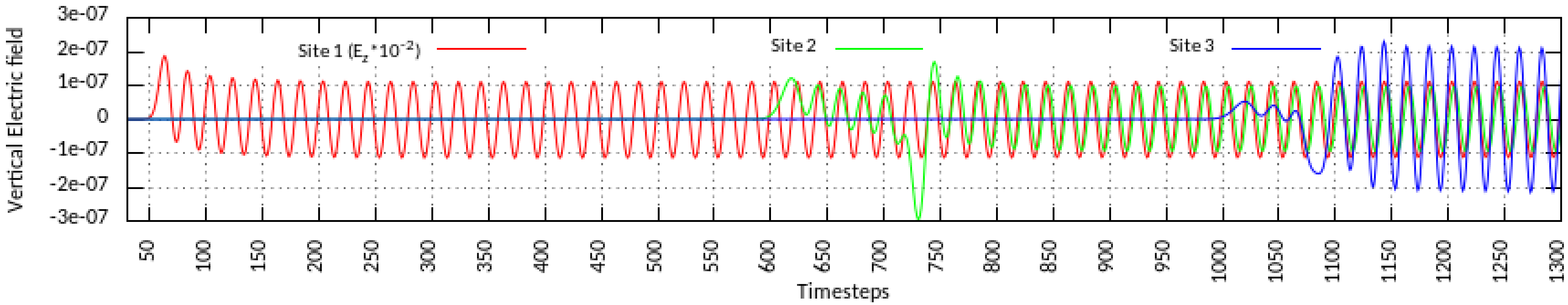

Figure 6.2 The transient E_z field component in free space condition at measured in sites 1, 2 and 3.

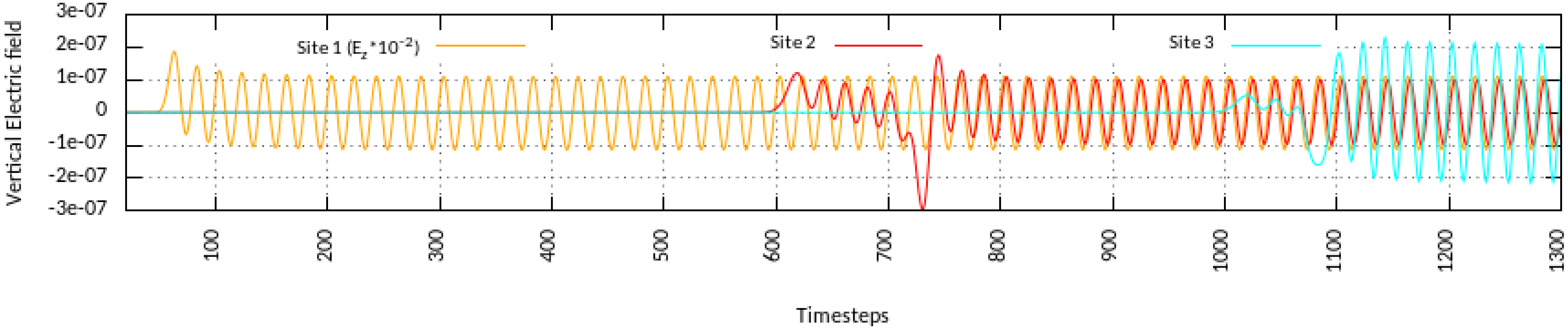

Figure 6.3 (a) The transient E_z field component collected on 21st Dec 2004, 13:03 LTC

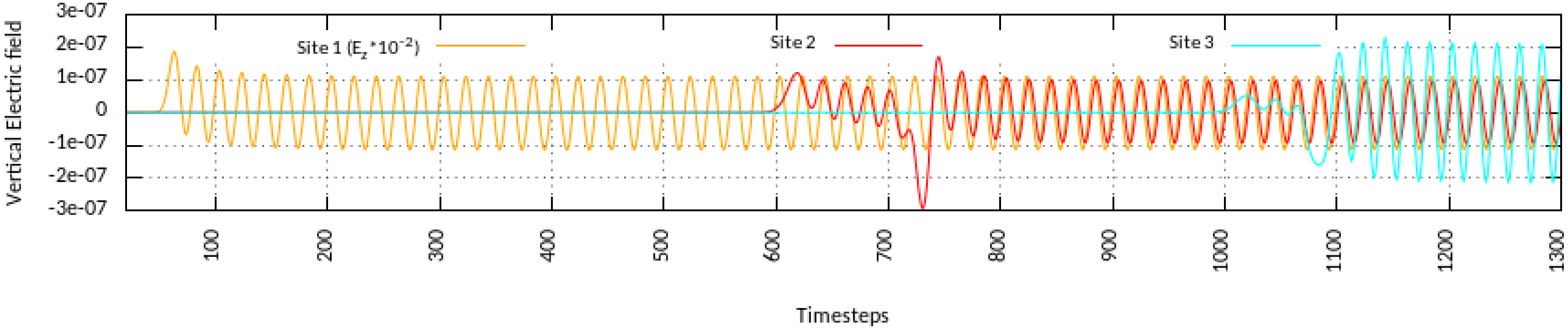

Figure 6.3(b) The transient E_z field component collected on 22nd Dec 2004, 00:35 LTC

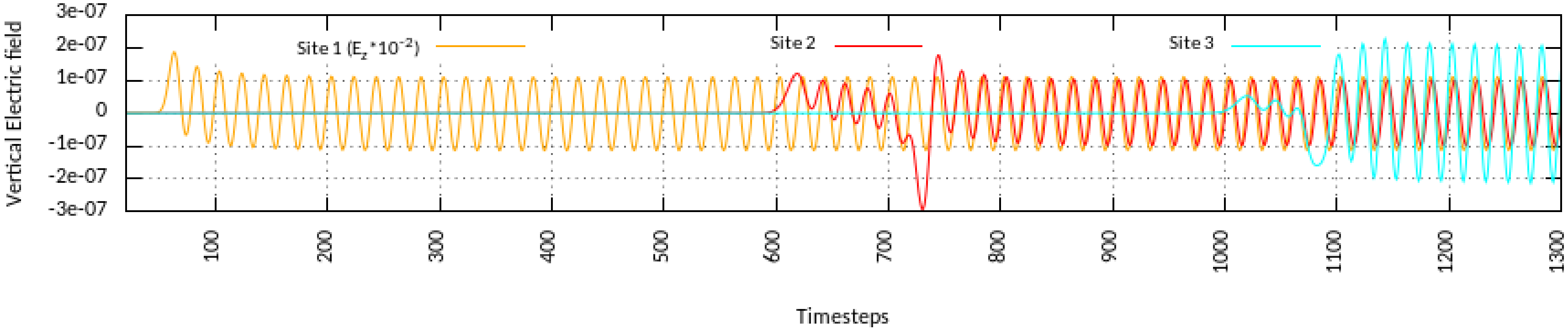

Figure 6.3(c) The transient E_z field component collected on 23rd Dec 2004, 11:00 LTC

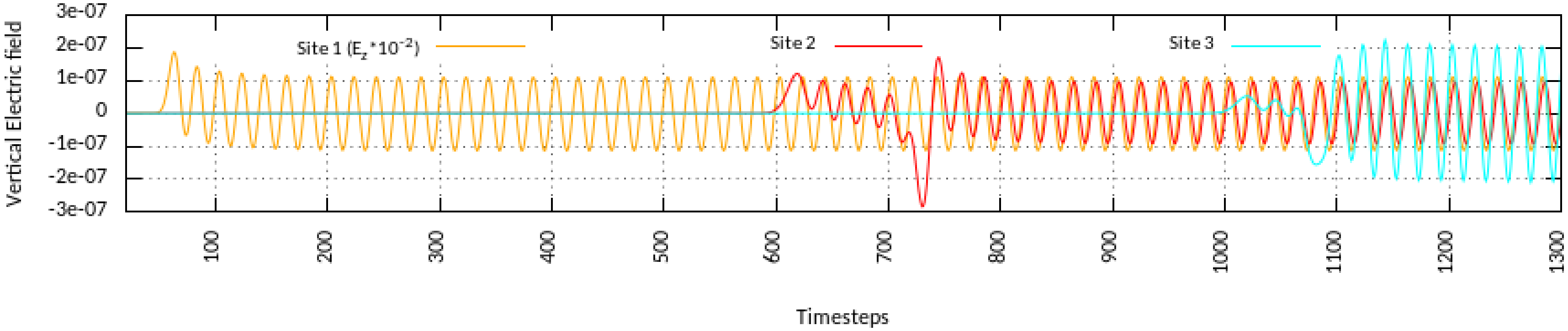

Figure 6.3(d) The transient E_z field component collected on 24th Dec 2004, 00:01 UTC

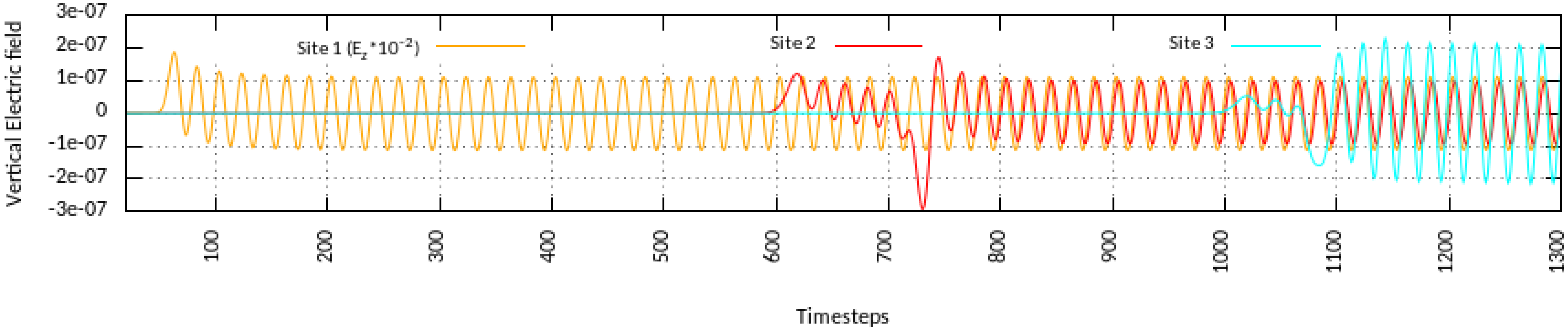

Figure 6.3(e) The transient E_z field component collected on 24th Dec 2004, 23:03 LTC

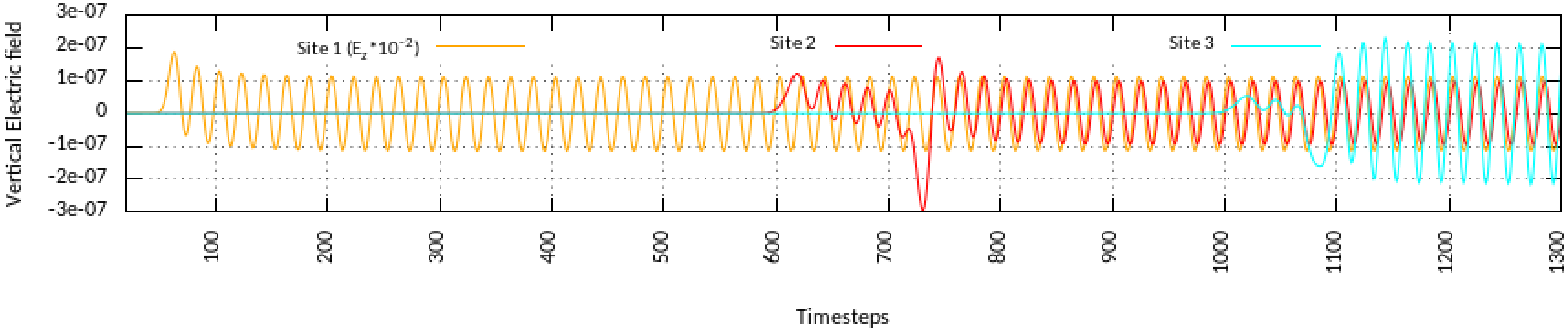

Figure 6.3(f) The transient E_z field component collected on 25th Dec 2004, 10:31 LTC

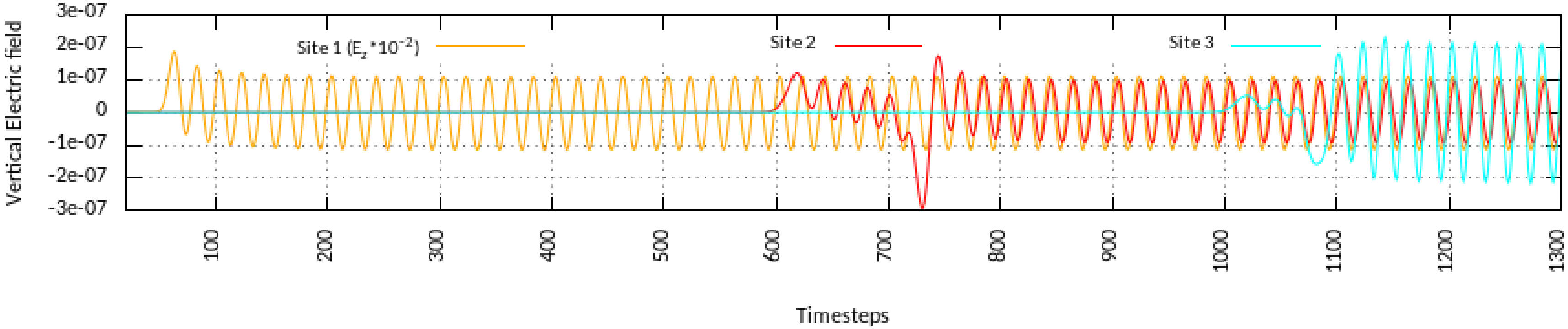

Figure 6.3(g) The transient E_z field component collected on 25th Dec 2004, 23:29 LTC

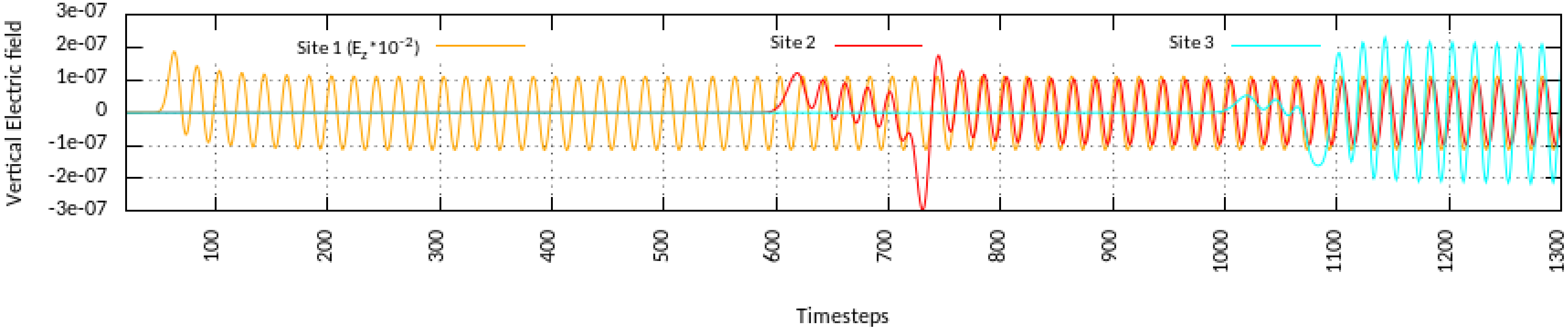

Figure 6.3(h) The transient E_z field component collected on 26th Dec 2004, 12:33 LTC

The transient E_z measured at all sites embed in them information regarding the physical conditions of the medium through which they have traversed. To the naked eye, all plots in Figure 6.3 appear identical to that of the free space condition in Figure 6.2. This is because the numerical difference in the amplitudes of the waves in each plot is indeed very small. An independent numerical analysis is required to quantify the numerical differences in the plots in Figure 6.2 and Figures 6.3(a-h). This will be reported in the following subsection.

6.3 Quantifying the Amplitude Difference in the Transient Electric Field E_z

The numerical study is conducted because of the plots in Figure 6.3 display numerical differences that are not visually discernible. To quantify these differences, calculations are performed to enumerate the difference in the amplitudes of the transient electric field in the free space and that in the anisotropic, dispersive condition for the duration of 200-time steps. Figures 6.4 depict the time domain in which these amplitude differences are calculated. Figure 6.4 (a) is a plot of the amplitudes at site 1 (i = 30, j = 4), (b) is that for site 2 (i = 300, j = 4) and (c) is that for site 3 (i = 500, j = 4). For site 1, the time domain spans from $n = 0 - 200$. For site 2, the time domain span is from $n = 600 - 800$, while for site 3, 1000 – 1200. The shaded region label '1' is for the free space while that labelled '2' is for anisotropic, dispersive condition. The amplitude for the transient E_z field measured at site 1 is relative large because less energy is dissipated by the medium. Compared to site 1, the amplitudes at site 2 and 3 are suppressed to an order of $\sim 10^{-2}$. The wave amplitude in both sites are suppressed due to the energy dissipation by the medium. In addition, at sites 2 and 3, due to their distant locations from the point source, the transient E_z field measured there are relatively influenced by the anisotropic, dispersive medium.

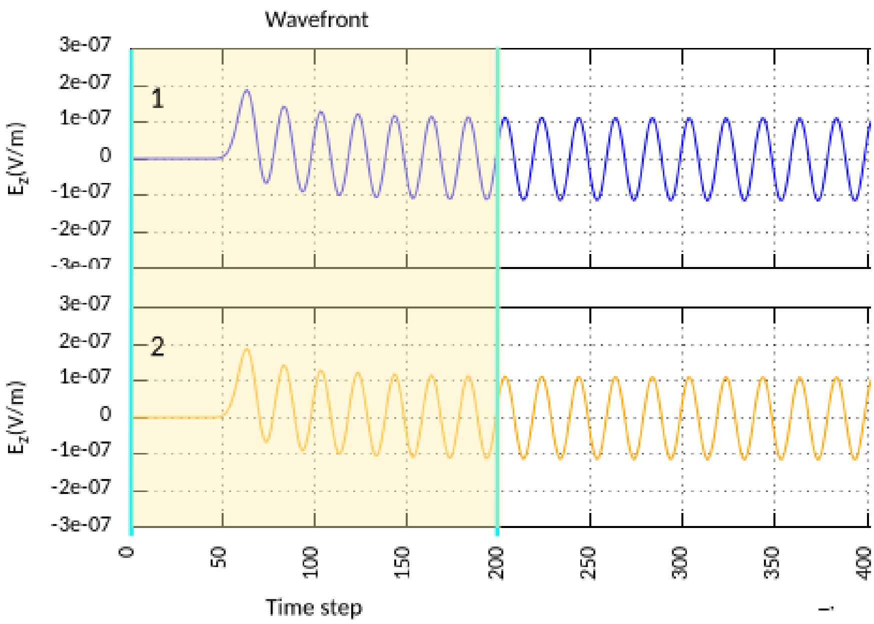

Figure 6.4 (a) Time domain in which the amplitudes of the transient electric field in free space (1) and anisotropic, dispersive medium (2) at site 1 is enumerated.

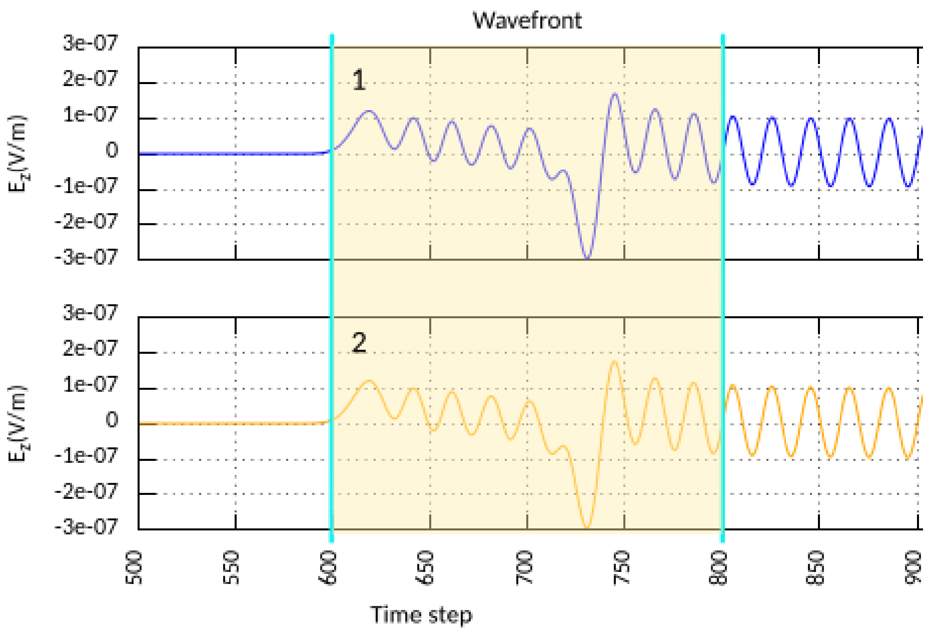

Figure 6.4 (b) Time domain in which the amplitudes of the transient electric field in free space (1) and anisotropic, dispersive medium (2) at site 2 is enumerated.

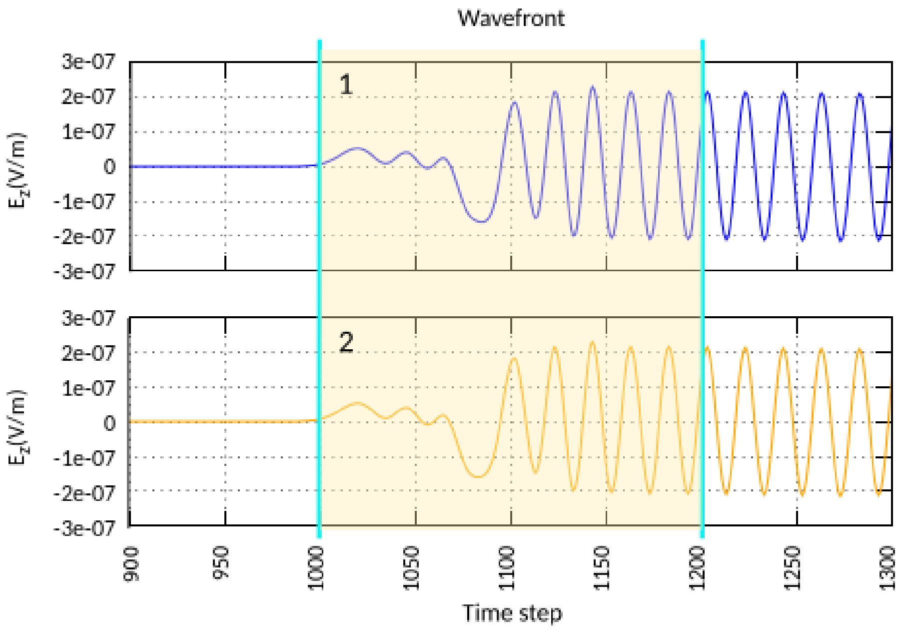

Figure 6.4 (c) Time domain in which the amplitudes of the transient electric field in free space (1) and anisotropic, dispersive medium (2) at site 3 is enumerated.

In Figures 6.5 (a-h), the left figures labelled '1' are the electron density profile N_e (data from CHAMP satellite) measured at the indicated date, while the right figures labelled '2' are the difference in transient field amplitudes at each site. It is to be noted that the figures labelled '2'in Figures 6.5 refer to the difference in field amplitudes instead of the field amplitude itself.

From the left figures (labelled '1') in Figures 6.5, it is observed that the value of electron density N_e is very low before the earthquake occurred, which are on 22nd Dec, 00:35 LTC, 24th Dec, 23:03 LTC and 25th Dec, 10:31 LTC. After the earthquake, the value of N_e consistently falls below $1.5 \times 10^{11}(\text{electrons/m}^3)$. The highest value of N_e (more than $1.5 \times 10^{11}(\text{electrons/m}^3)$) are identified on 21st Dec, 13:03 LTC, 23rd Dec, 11:00 LTC and 25th Dec, 23:29 LTC. On 24th Dec, 00: 01

LTC, a few peaks of the high value observed and the N_e profile during this time is distorted.

Referring to the right figures (labelled ‘2’) in Figure 6.5, the amplitude difference for site 1 shows no variance for all plots. This is because the location of the site 1 is very close to the source. The transient E_z field collected at this site originate from the source with the lowest interference from the medium. The difference in amplitude is almost zero. Thus, we can conclude the waves measured at site 1 are almost the same with the waves in the free space condition. Meanwhile, for site 2, the plots with low N_e values, the maximum and minimum range of the amplitude when reaching steady state fall consistently between 1.5×10^{-8} (V/m) and -1.58×10^{-8} (V/m). For the plots with high N_e values, the maximum and minimum range of the amplitude fall consistently between 2×10^{-8} (V/m) and -2×10^{-8} (V/m). On 24th Dec, 00:01 LTC where two peaks of high values in N_e profile were observed, the maximum and minimum range of the amplitude is 1.9×10^{-8} (V/m) and -2×10^{-8} (V/m). This range is slightly higher than the range for low N_e value plots, but still low compared to the high N_e value plots.

Meanwhile, for site 3, the same pattern is observed for all data. The plots with low N_e values, the maximum and minimum range of the amplitude when reaching steady state fall consistently between 1×10^{-8} (V/m) and -1×10^{-8} (V/m). For the plots with high N_e values, the maximum and minimum range of the amplitude is consistently between 1.7×10^{-8} (V/m) and -1.7×10^{-8} (V/m). On 24th Dec, 00:01 LTC, the maximum and minimum range of the amplitude is 4.14×10^{-8} (V/m) and -4.05×10^{-8} (V/m).

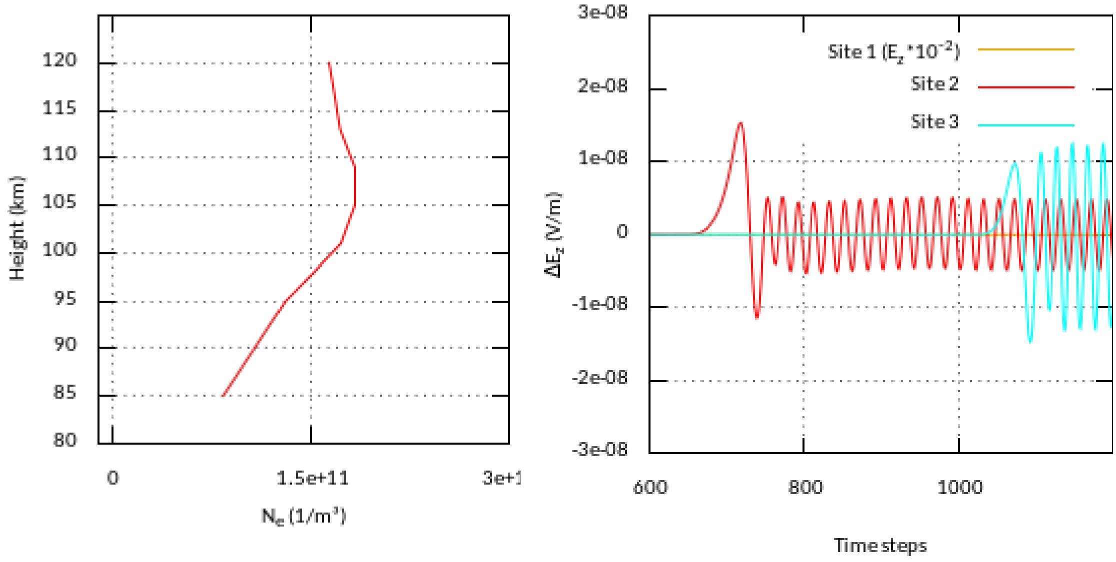

(1) (2)

Figure 6.5(a) (1) The electron density profile on 21st Dec 2004, 13:03 LTC (2) The amplitude difference at sites 1, 2 and 3.

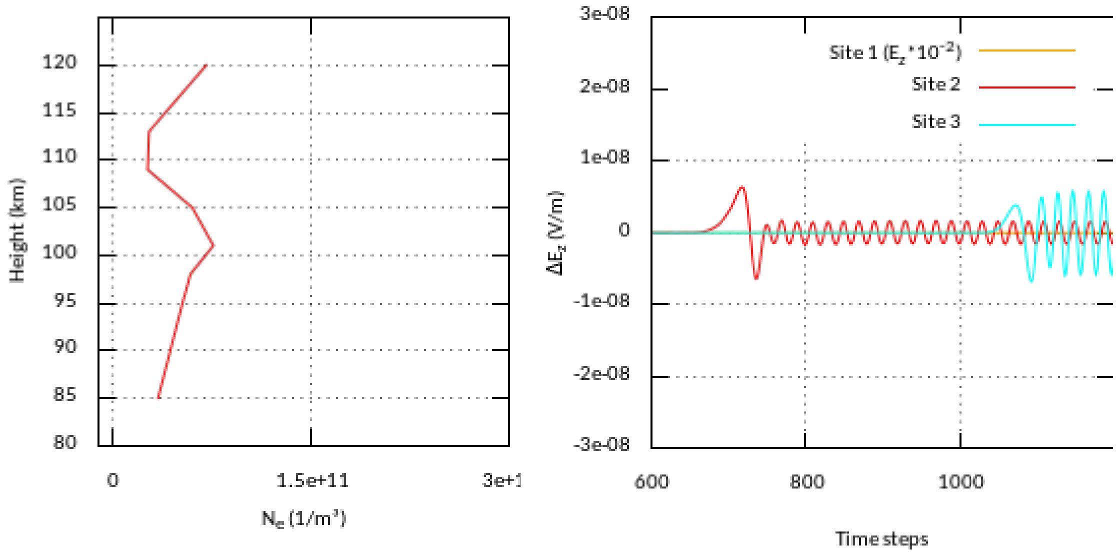

(1) (2)

Figure 6.5(b) (1) The electron density profile on 22nd Dec 2004, 00:35 LTC (2) The amplitude difference at sites 1, 2 and 3.

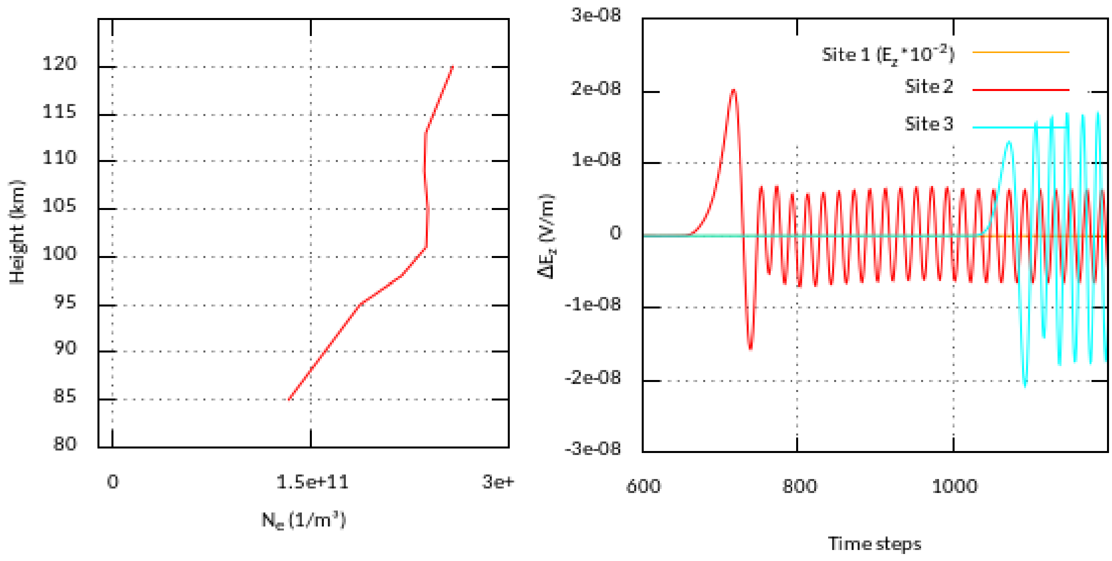

(1) (2)

Figure 6.5(c) (1) The electron density profile on 23rd Dec 2004, 11:00 LTC (2) The amplitude difference at sites 1, 2 and 3.

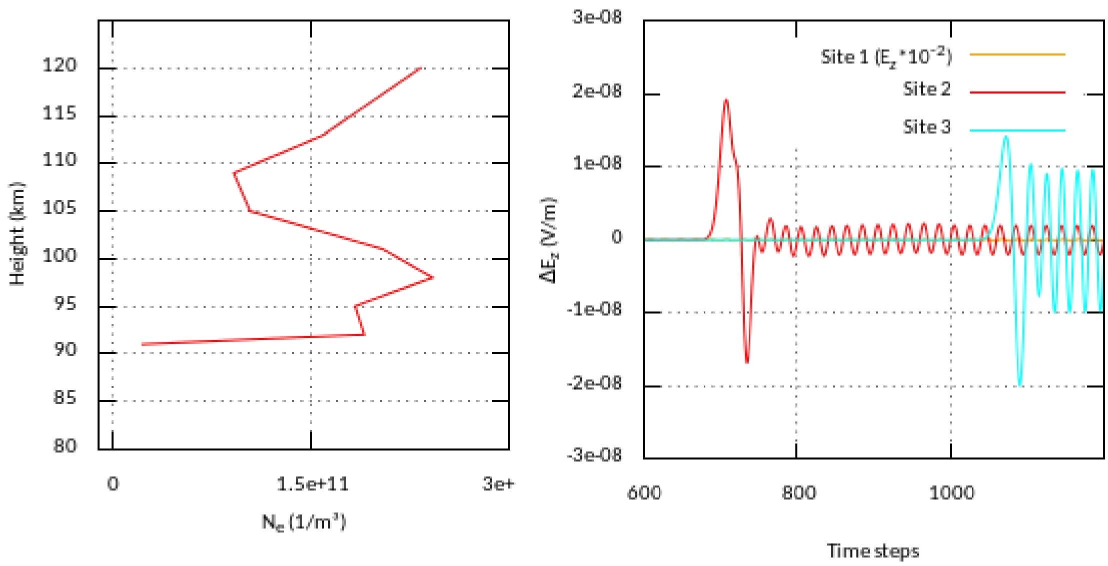

(1) (2)

Figure 6.5(d) (1) The electron density profile on 24th Dec 2004, 00:01 LTC (2) The amplitude difference at sites 1, 2 and 3.

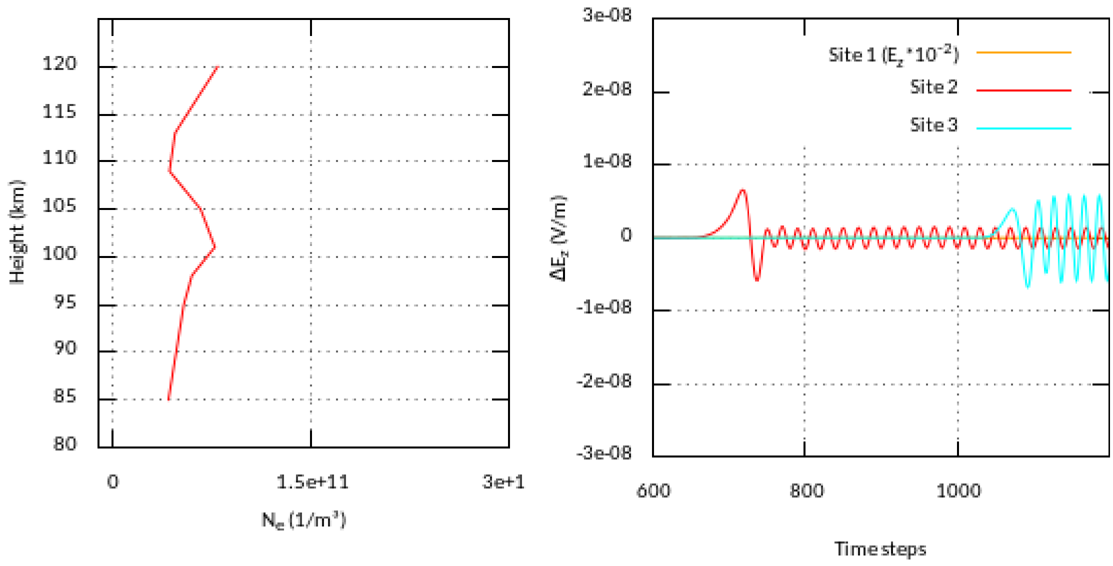

(1) (2)

Figure 6.5(e) (1) The electron density profile on 24th Dec 2004, 23:03 LTC (2) The amplitude difference at sites 1, 2 and 3.

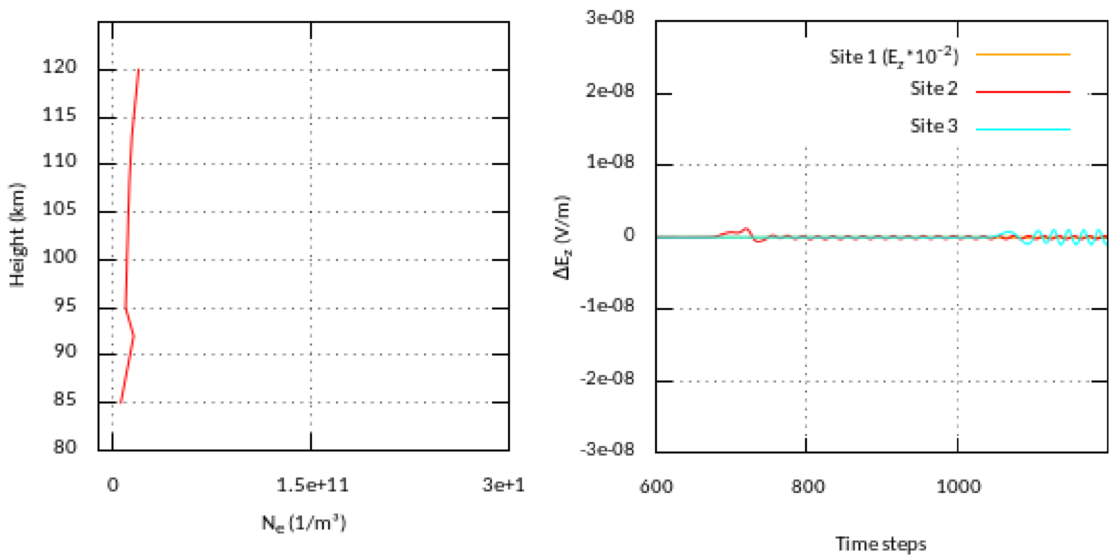

(1) (2)

Figure 6.5(f) (1) The electron density profile on 25th Dec 2004, 10:31 LTC (2) The amplitude difference at sites 1, 2 and 3.

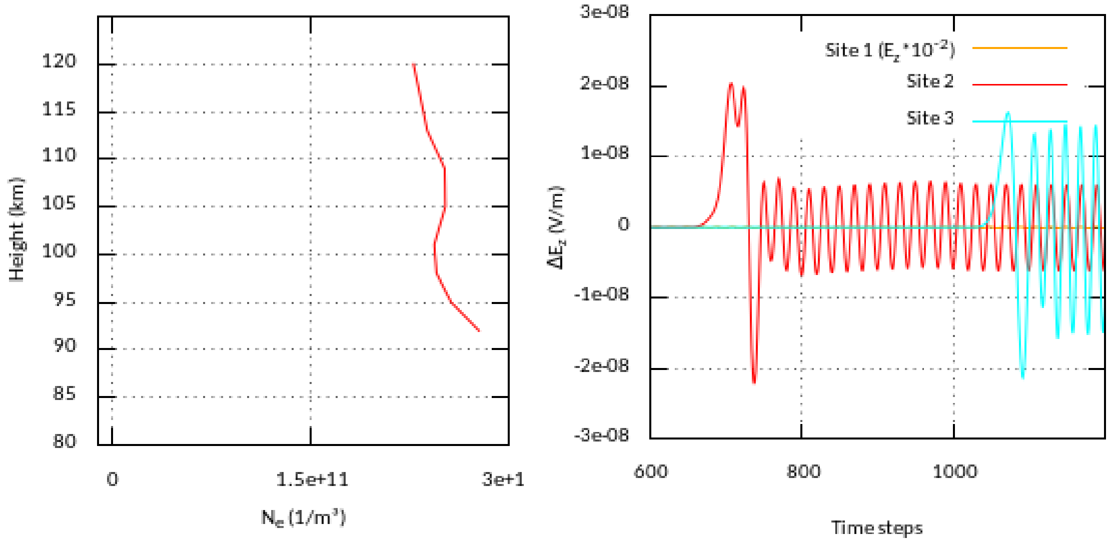

(1) (2)

Figure 6.5(g) (1) The electron density profile on 25th Dec 2004, 23:29 LTC (2) The amplitude difference at sites 1, 2 and 3.

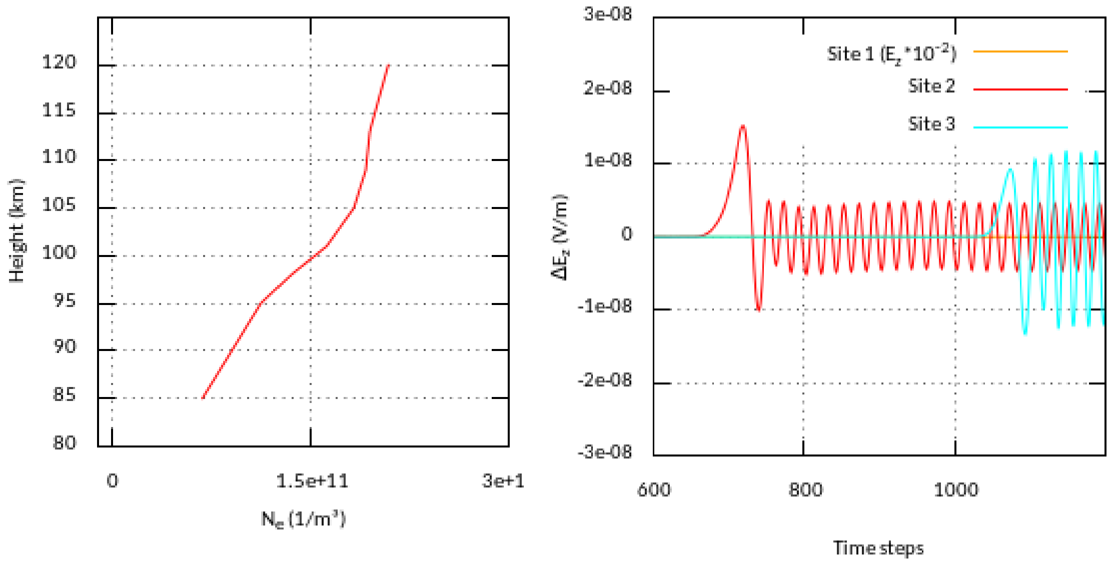

(1) (2)

Figure 6.5(h) (1) The electron density profile on 26th Dec 2004, 12:33 LTC (2) The amplitude difference at sites 1, 2 and 3.

6.4 ΔQ_s as an Earthquake Precursor

As an attempt to model an earthquake precursor using the FDTD simulation and the electron density from the satellite data, an empirical parameter is introduced, which is to be referred as ΔQ_s. ΔQ_s at a site s ($s = 1,2,3$) is defined as the root mean square of ΔE_z as shown in the right figures in Figure 6.5, spanning the corresponding time domain n a defined in Figure 6.4 for these sites. Specifically, ΔQ_s is calculated as per

$$\Delta Q_s = \sqrt{\frac{1}{N}\sum_{n=n_1}^{n_2}(\Delta E_z^n)^2}, \tag{6.1}$$

where $n_2 - n_1 = N = 200$ is the time span, $[n_1, n_2]$ are the time domain as defined in Figure 6.4 for each site s. For site $s = 2$, $[n_1, n_2] =$ [600, 800], while for site $s = 3$, $[n_1, n_2] = [1000,1200]$. $\Delta Q_{s=1}$ is not calculated since it is approximately zero throughout. $\Delta Q_{s=2}$ and $\Delta Q_{s=3}$ are plotted in Figure 6.6. The green line in the graph indicates the time when the Earthquake occurs.

The rationale to define ΔQ_s as a possible earthquake precursor is based on the feasible assumption that the simulated waves arriving at any site in the active simulation grid embed within them the historic experience (i.e., information regarding the physical properties of the medium) accumulated during the course of traversing through the ionospheric medium. As such, if anomalous variation in the $N_e(h)$ profile occurs in the ionosphere during an earthquake, such information will be implicitly recorded (embedded) in the history of the EM waves traversing through the medium, which net effect is in turn captured by the definition of ΔQ_s. In other words, measuring ΔQ_s at a site s can theoretically provide the instantaneous knowledge of the 'state' [i.e., $N_e(h)$] of the ionosphere using the simulated EM waves as a convenient 'probe'.

Before the earthquake event, specifically before 26th Dec, the magnitude range is between 9.2×10^{-8} and 8.8×10^{-8} for site 2 and between 1.14×10^{-7} and 1.10×10^{-7} for site 3. After the earthquake, specifically after 27th Dec, the magnitude range is between 9.12×10^{-8} and 8.9×10^{-8} for site 2 and between 1.145×10^{-7} and 1.13×10^{-7} for site 3. The gap in magnitude range before earthquake is 0.4 for site 2 and 0.04 for site 3, while the gap in magnitude range after the earthquake is 0.22 for site 2 and 0.015 for site3. In addition, the lowest magnitude values in both sites observed on 24th Dec, at 00:01 LTC. It is believed that the statistical fluctuation in the ΔQ_s before a major earthquake may contain predictive information if analysed in a more rigorous manner. This would be even more plausible if satellite data is available at a much higher frequency (e.g., once per hour). Unfortunately, due to the lack of satellite data (only a few data points are available in the case of the 2004 Indonesian earthquake), such in-depth statistical analyses on the fluctuation of ΔQ_s is not performed in this thesis and is delayed to future work.

The ΔQ_s plot as obtained at the site $s = 3$ appear to be lacking pronounce features expected for a definitive earthquake precursor. The $\Delta Q_{s=2}$ plot has a peak coincides with the time when the earthquake occurred, albeit the tell-tale signature is relatively fuzzy due to the presence of other peaks occurring also during the period before and after the earthquake.

Based on the $\Delta Q_{s=2}$ and $\Delta Q_{s=3}$ plots per se, it is difficult to claim the strong positive predictive power to have been achieved. The most major reason rendering the poor performance of ΔQ_s as a predictor is attributed to the bare minimum efficiency achieved by the PML. Should the PML delivers a higher absorption efficiency, e.g., a relative error suppressed to the order of, say $\sim 10^{-6}$, the quality of the simulations can be greatly enhanced. Unfortunately, achieving a highly effective ABC for the ionospheric medium in FDTD simulation is a hard-core task. Based on an exhaustive literature search, a robust and effective ABC for FDTD simulation of EM waves propagating in the ionospheric medium has never been reported as far as we are aware of. The level of performance achieved by this thesis using the PML is representing the best-effort performance at present.

Independent from the PML performance consideration, the predictive power of the ΔQ plot is also limited by the resolution, which is defined as how frequent in real time where satellite data of the electron density profile are available. Such a limitation is a pragmatic one, and could possibly be overcome if electron density profile data becomes available at a much higher frequency, say, once per hour. It is also possible to improve the predictive power of ΔQ_s by having more sites, s, so that a more comprehensive statistical analysis can be performed. A more efficient ABC beyond that was achieved by the present FDTD code is also expected to contribute positively to the predictive power of ΔQ_s. Unfortunately, however, due to the race to complete the thesis before the last-chance submission deadline, improving the quality of the measured data along these lines can only be carried out as a future work.

It is opined that the attempt to define ΔQ_s as an earthquake precursor, despite not an entire success, is a viable approach. The works reported in this thesis serve as an initial attempt to realise this idea.

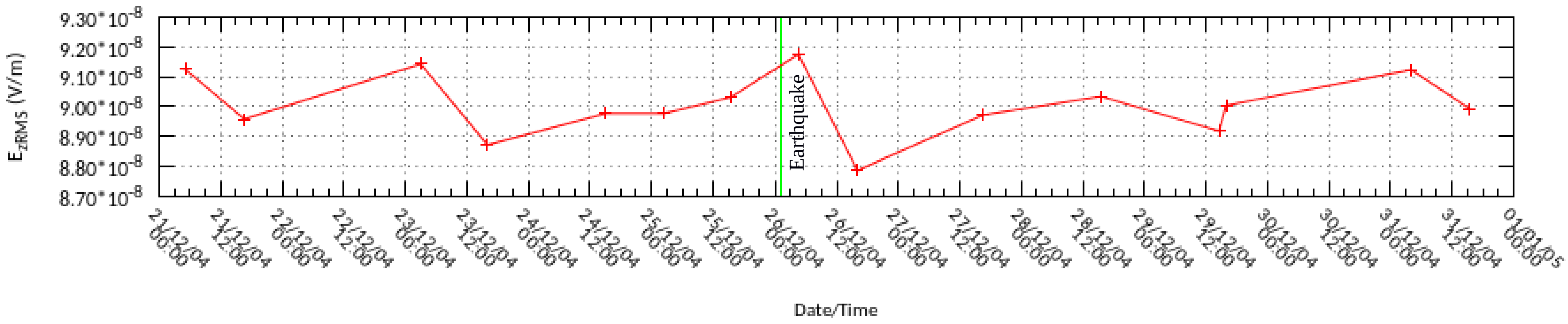

Figure 6.6 (a) $\Delta Q_{s=2}$ as a function of the date when electron density data were taken.

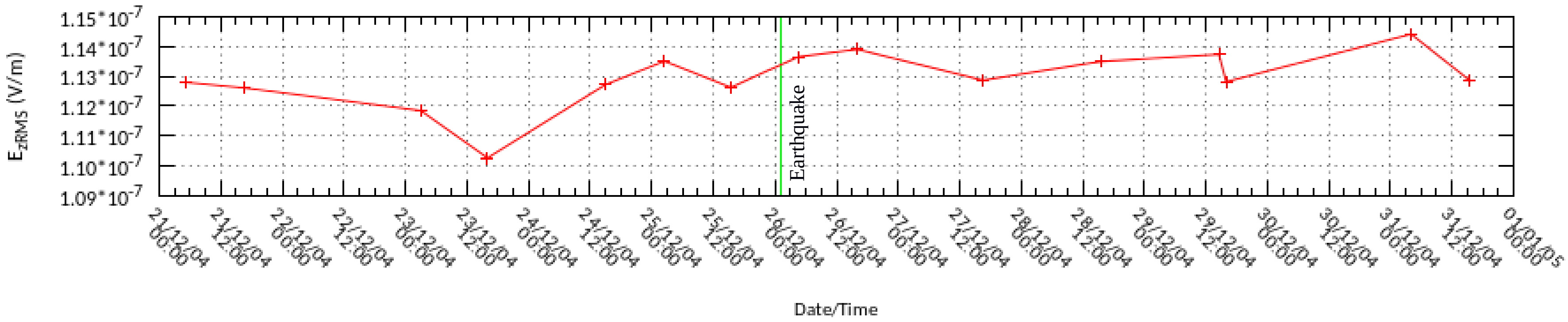

Figure 6.6 (b) $\Delta Q_{s=3}$ as a function of the date when electron density data were taken.

6.5 Summary

The implementation of experimental data from the CHAMP satellite in 2D FDTD modelling was studied. The full-fledged modelling of E_z propagation in ionosphere using the home-grown 2D FDTD codes are carried out. Three sites near to the Earth's surface are chosen to measure and analyse the transient E_z fields. To this end, the transient E_z fields in the free space (without N_e profile) and that with a non-zero N_e profile (satellite data from CHAMP) was enumerated as a function of step, n. It is observed that the transient field in the steady state displays a relatively larger amplitude in a medium with larger N_e than that with a smaller N_e. There are six data with a high value of N_e detected before the earthquake. Based on the data generated in the FDTD simulation, an attempt was made to simulate an earthquake precursor via the definition of ΔQ_s. It is basically the root mean square of E_z at site s taken over a temporal length of 200 steps after the waves arrives at the site. The rationale to define ΔQ_s as a possible earthquake precursor is based on the feasible assumption that the simulated waves arriving at any site in the active simulation grid embed within them the historic experience (i.e., information regarding the physical properties of the medium) accumulated during the course of traversing through the ionospheric medium. As such, if anomalous variation in the $N_e(h)$ profile occurs in the ionosphere during an earthquake, such information will be implicitly recorded (embedded) in the history of the EM waves traversing through the medium, which net effect is in turn captured by the definition of ΔQ_s. In other words, measuring ΔQ_s at a site s can theoretically provide the instantaneous knowledge of the 'state' [i.e., $N_e(h)$] of the ionosphere using the simulated EM waves as a convenient 'probe'. ΔQ_s were calculated and analysed for two selected sites, $s = 2, 3$. Statistical fluctuation in ΔQ_s before the occurrence of a major seismic event is believed to contain predictive information of the impending earthquake. However, due to the lack of satellite data such in-depth statistical analyses on the fluctuation of ΔQ_s is not performed in this thesis and is delayed to future work. Hence, there is no conclusive prediction that can be drawn from the statistical fluctuation of ΔQ_s due to the limited number of data points. However, based on the feature of the ΔQ_s plot alone, it is found that the $\Delta Q_{s=3}$ plot marginally hinted a coincidence of a dominate peak with the occurrence of the earthquake. The attempt to model ΔQ_s does not result in a definitive earthquake precursor for a few reasons, including the lack of high-frequency measured data of the electron density profile for the 2004 Indonesian earthquake, a non-optimal ABC in the FDTD simulation of inhomogeneous, dispersive and anisotropic ionospheric medium, and lastly the time constraint. Admittedly, the present attempt to model a precursor via the FDTD methodology still requires further refinement, validation and justification. In particular, a more comprehensive data collection and analyses for ΔQ_s should be carried out to cover more measuring sites s.

CHAPTER 7

CONCLUSIONS AND FUTURE WORKS

7.1 Conclusions and Findings

Overall, this thesis has attempted to (1) identify the variation in the atmospheric electron density profile near the epicentre region in the South East Asia during the 2004 Sumatra earthquake using CHAMP satellite data, (2) develop a home-grown 2D finite difference time domain (FDTD) code to simulate the propagation of electromagnetic wave in local Earth-ionosphere. The simulation grid extends vertically up to an altitude of 120 km above Earth's surface and horizontally over a distance of 600 km, and (3) applies FDTD simulation to propose a viable model of earthquake precursor.

To use the FDTD methodology to simulate the intended system as prieviously, a major ingredient required is the information of the atmosphere's electron density profile $N_e(h)$ as a function of altitude h. $N_e(h)$ at high altitude. At the (high) altitude range of ~ 90 km – 120 km, i.e., in the ionospheric region, $N_e(h)$ becomes significant. In this thesis, $N_e(h)$ is measured by the CHAMP satellite. The data from the CHAMP satellite were collected for a few days before and during the occurrence of the earthquake. Data of quiet and perturbed condition were analysed based on solar activity and geomagnetic storm indices.

Two absorbing boundary conditions, namely, differential ABC and PML have been implemented in the 2D FDTD code for the anisotropic, inhomogeneous and dispersive medium of the ionosphere. ABC is an integral ingredient in any FDTD code. It ensures the simulated EM propagation suffers a minimal amount of 'contamination' during the course of the simulation, i.e., interference originated from the reflection of the boundary, which is an undesirable numerical artefact not present in a realistic scenario. The simulated waves in these media are concurrently measured at selected sites and compared. The expected positive response has been observed, inferring that the FDTD codes do behave in a manner that it should.

Finally, the implementation of experimental data from the CHAMP satellite in 2D FDTD modelling was studied. The transient E_z field component for each electron density profile was analysed. The transient E_z reflected at three sites were monitored and measured. These transient E_z waves are plotted as a function of n. To quantify the effect of the electron density profile in the ionosphere during the earthquake to the transient field, the difference of the EM wave in free space and anisotropic, dispersive conditions are measured. ΔQ_S , which is a parameter introduced to act as an earthquake precursor, is calculated. The range of magnitude values before and after the earthquake is monitored. The expected feature of ΔQ_S protruding a prominent peak during the occurrence of the earthquake is not definitely distinctive due to poor resolution of the satellite data, a relatively large contamination from waves reflected from the boundaries, and the lack of time to sample more ΔQ_S plots to improve statistics quality. Nevertheless, the effort attempted in this thesis to use FDTD computational approach to simulate EM propagation through the ionosphere, and the introduction of ΔQ_S as an earthquake precursor should be viewed as a viable approach to monitor earthquake.

As a conclusive remark, it is technically and principally viable to couple realistic data from the satellite into computational electromagnetics modelling, as attempted in this thesis, to model an earthquake precursor. The research model in this thesis can be realistically implemented in practice if the insufficiencies mentioned above can be mitigated. This thesis has presented a novel attempt and proof of concept to a new approach in earthquake prediction research which is conceptually easy, computationally-doable, less costly.

7.2 Future Works

1. In-house development of Nano sat to collect ionosphere parameter for SEA region.

   The data for electron density is limited by the satellites sent to the space and active ionosonde on the ground. Some of them are not open-access. The high cost to launch a satellite with the complex sensor is one of the constraints for countries in South East Asia. In future, more satellite data will be used to verify the codes, such as DEMETER satellite. However, the DEMETER satellite is not functioning because of the lifetime is an end. There will be an advantage if we can launch our own satellite to collect data in ionosphere. The data form this satellite can be utilized not only in earthquake study but other natural disaster monitoring as well.

2. The improvement of PML in this code to obtain value of relative error as low as possible. The increasing of cells number for PML layers is not effective since thE-layer will suppress the energy of the wave. A few numerical experiments should be conducted to increase the performance of PML. This experiment is to define the most efficient PML for the inhomogeneous condition. In FDTD modelling, a current task only developed 2D code which is sufficient to support the objective to model a localize ionosphere. In future,

a 3D model may necessary to study the effect of the ionospheric perturbation in the wide range.

3. The validation and verification of modelling data by cross-checking with experimental data taken from ground sensors.

   This suggestion provides a better understanding of the relationship between ground sensor data, satellite data, and modelling data. In this case, the FDTD code needs fine-tuning to increase the efficiency and decrease loss at the boundary.

4. A mechanism to predict electromagnetic signal behaviour in the ionosphere.

   It is possible to develop a procedural algorithm to observe the time shift during the quiet profile and disturbed profile. This algorithm also should be applicable to calculate the amplitude shift. This will be an alternative mechanism to fulfil the gap in the earthquake precursor study. Figure 7.1 summarises the proposed mechanism. This mechanism comprises of multicomponent segments, of which the present work is an integral part of it.

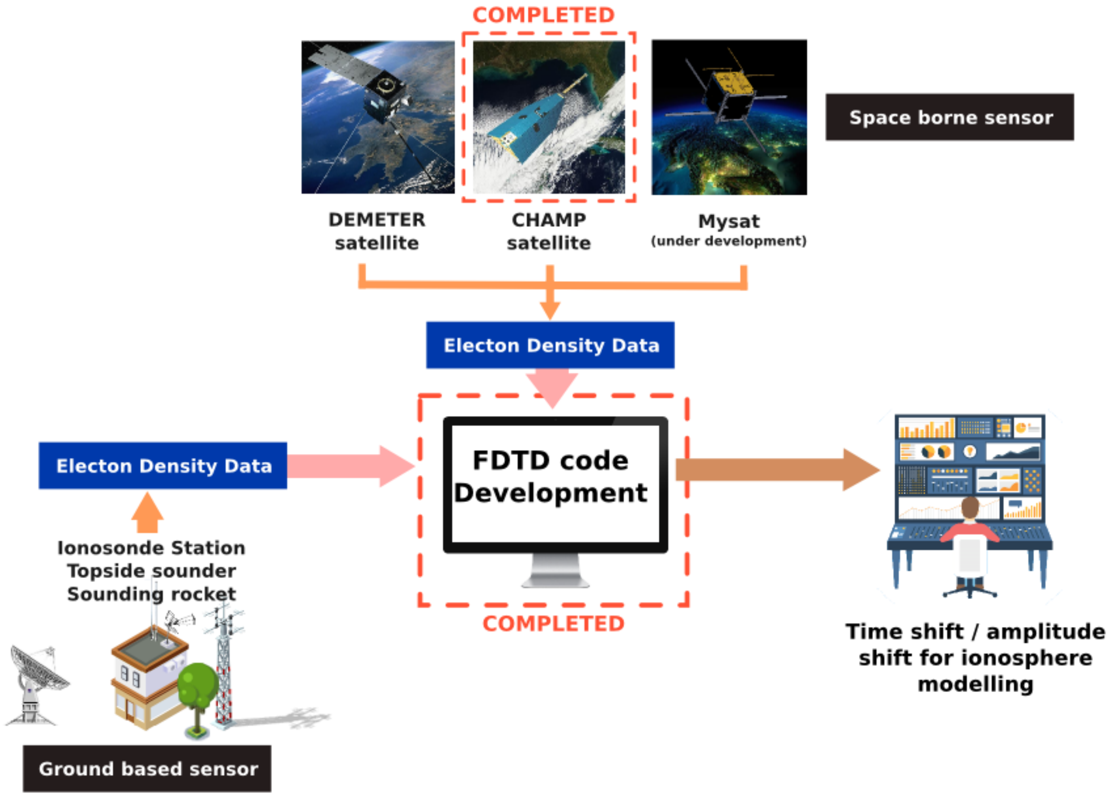

Figure 7.1 The FDTD development and future tasks.

REFERENCES

Afraimovich, E., Perevalova, N., Plotnikov, A., & Uralov, A. (2000). The shock-acoustic waves generated by earthquakes. *arXiv preprint physics/0007041*.

Al-Jabr, A. A., Alsunaidi, M. A., Tien, N., & Ooi, B. S. (2013). A Simple FDTD Algorithm for Simulating EM-Wave Propagation in General Dispersive Anisotropic Material. *Antennas and Propagation, IEEE Transactions on, 61*(3), 1321-1326. doi: 10.1109/tap.2012.2227447

Anthes, R. (2011). Exploring Earth's atmosphere with radio occultation: Contributions to weather, climate and space weather. *Atmos. Meas. Tech, 4*, 1077-1103.

Antselevich, M. (1971). The influence of Tashkent earthquake on the earth's magnetic field and the ionosphere, Tashkent earthquake 26 April 1966. *FAN Publ*, 187-188.

Appleton, E. (1927). The existence of more than one ionised layer in the upper atmosphere. *Nature, 120*, 330.

Artru, J., Farges, T., & Lognonné, P. (2004). Acoustic waves generated from seismic surface waves: propagation properties determined from Doppler sounding observations and normal-mode modelling. *Geophysical Journal International, 158*(3), 1067-1077.

Azadifar, M., Li, D., Rachidi, F., Rubinstein, M., Diendorfer, G., Pichler, H., . . . Pavanello, D. (2016). *Simultaneous Current and Distant Electric Field Waveforms from Upward Lightning: Effect of Ionospheric Reflection.* Paper presented at the 24th International Lightning Detection Conference (ILDC).

Bagiya, M. S., Kherani, E. A., Sunil, P. S., Sunil, A. S., Sunda, S., & Ramesh, D. S. (2017). Origin of the ahead of tsunami traveling ionospheric disturbances during Sumatra tsunami and offshore forecasting. *Journal of Geophysical Research: Space Physics, 122*(7), 7742-7749. doi: 10.1002/2017ja023971

Berenger, J.-P. (1994). A perfectly matched layer for the absorption of electromagnetic waves. *Journal of Computational Physics, 114*(2), 185-200. doi: http://dx.doi.org/10.1006/jcph.1994.1159

Bérenger, J.-P. (2002). FDTD computation of vlf-lf propagation in the Earth-ionosphere waveguide. *Annales Des Télécommunications, 57*(11-12), 1059-1090. doi: 10.1007/bf02999454

Berenger, J. P. (2006, 9-14 July 2006). *Use of the FDTD method for computing the VLF-LF propagation in the Earth-Ionosphere waveguide.* Paper presented at the Antennas and Propagation Society International Symposium 2006, IEEE.

Bhattacharya, S., Sarkar, S., Gwal, A., & Parrot, M. (2009). Electric and magnetic field perturbations recorded by DEMETER satellite before seismic events of the 17th July 2006 M 7.7 earthquake in Indonesia. *Journal of Asian Earth Sciences, 34*(5), 634-644.

Bickel, J., Ferguson, J., & Stanley, G. (1970). Experimental observation of magnetic field effects on VLF propagation at night. *Radio Science, 5*(1), 19-25.

Bilitza, D., Altadill, D., Zhang, Y., Mertens, C., Truhlik, V., Richards, P., . . . Reinisch, B. (2014). The International Reference Ionosphere 2012–a model of international collaboration. *Journal of Space Weather and Space Climate, 4*, A07.

Błęçki, J., Parrot, M., & Wronowski, R. (2010). Studies of the electromagnetic field variations in ELF frequency range registered by DEMETER over the Sichuan region prior to the 12 May 2008 earthquake. *International Journal of Remote Sensing, 31*(13), 3615-3629.

Bruevich, E., & Bruevich, V. (2013). Correlation study of some solar activity indices in the cycles 21-23. *arXiv preprint arXiv:1304.4545*.

Budden, K. G. (1985). *The Propagation of Radio Waves: The Theory of Radio Waves of Low Power in the Ionosphere and Magnetosphere*. Cambridge: Cambridge University Press.

Buresova, D., McKinnell, L. A., Lastovicka, J., & Boska, J. (2011, 13-20 Aug. 2011). *Ionospheric F2 layer behavior during prolonged solar minimum*. Paper presented at the 2011 XXXth URSI General Assembly and Scientific Symposium.

Carlson, H., & Gordon, W. (1966). Radar spectrographic estimates of ionic composition from 225 to 1400 kilometers for solar minimum winter and summer conditions. *Journal of Geophysical Research, 71*(23), 5573-5578.

Cela, C. J. (2012). FDTD Retrieved 10 July 2017, from http://www.ece.utah.edu/~ece6340/LECTURES/lecture%2014/FDTD.pdf

Chakraborty, S., Sasmal, S., Chakrabarti, S. K., & Bhattacharya, A. (2018). Observational signatures of unusual outgoing longwave radiation (OLR) and atmospheric gravity waves (AGW) as precursory effects of May 2015 Nepal earthquakes. *Journal of Geodynamics, 113*, 43-51.

Chapman, S. (1931). The absorption and dissociative or ionizing effect of monochromatic radiation in an atmosphere on a rotating earth. *Proceedings of the Physical Society, 43*(1), 26.

Chmyrev, V., Smith, A., Kataria, D., Nesterov, B., Owen, C., Sammonds, P., . . . Vallianatos, F. (2013). Detection and monitoring of earthquake precursors: TwinSat, a Russia–UK satellite project. *Advances in Space Research, 52*(6), 1135-1145.

Chum, J., Liu, J.-Y., Laštovička, J., Fišer, J., Mošna, Z., Baše, J., & Sun, Y.-Y. (2016). Ionospheric signatures of the April 25, 2015 Nepal earthquake and the relative role of compression and advection for Doppler sounding of infrasound in the ionosphere. *Earth, planets and space, 68*(1), 24.

Clilverd, M. A., Clark, T. D. G., Clarke, E., & Rishbeth, H. (1998). Increased magnetic storm activity from 1868 to 1995. *Journal of Atmospheric and Solar-Terrestrial Physics, 60*(10), 1047-1056. doi: https://doi.org/10.1016/S1364-6826(98)00049-2

Courant, R., Friedrichs, K., & Lewy, H. (1967). On the Partial Difference Equations of Mathematical Physics. *IBM Journal of Research and Development, 11*(2), 215-234. doi: 10.1147/rd.112.0215

Cummer, S. A. (2000). Modeling electromagnetic propagation in the Earth-ionosphere waveguide. *Antennas and Propagation, IEEE Transactions on, 48*(9), 1420-1429. doi: 10.1109/8.898776

Davies, K., & Baker, D. M. (1965). Ionospheric effects observed around the time of the Alaskan earthquake of March 28, 1964. *Journal of Geophysical Research, 70*(9), 2251-2253.

Depueva, A. (2012). Peculiarities of low-latitude and equatorial ionosphere prior to strong earthquakes. *Geomatics, Natural Hazards and Risk, 3*(3), 207-224. doi: 10.1080/19475705.2011.619206

Devi, M., Medhi, A., Sarma, A. J. D. S., & Barbara, A. K. (2013). Growth and inhibition of equatorial anomaly prior to an earthquake (EQ): case studies with total electron content (TEC) data for major EQs of Japan 2011 and Indonesia 2012. *Positioning, 2013*.

Devi, M., Patgiri, S., Barbara, A. K., Oyama, K.-I., Ryu, K., Depuev, V., & Depueva, A. (2018). Role of Equatorial Anomaly in Earthquake time precursive features: A few strong events over West Pacific Zone. *Advances in Space Research*. doi: https://doi.org/10.1016/j.asr.2018.01.003

Ding, J., Zhao, Z., Yang, Y., Liu, Y., & Nie, Z.-P. (2017). An Optimized PLRC-FDTD Model of Wave Propagation in Anisotropic Magnetized Plasma. *Progress In Electromagnetics Research, 59*, 25-31.

Duan, X., Yang, H., Liu, H., & An, L. (2009). Auxiliary Differential Equation FDTD Method of Plasma in Parallel Environment. *Journal of Infrared, Millimeter, and Terahertz Waves, 30*(8), 860-867. doi: 10.1007/s10762-009-9498-2

Eftaxias, K., Kapiris, P., Polygiannakis, J., Peratzakis, A., Kopanas, J., Antonopoulos, G., & Rigas, D. (2003). Experience of short term earthquake precursors with VLF? VHF electromagnetic emissions. *Natural Hazards and Earth System Science, 3*(3/4), 217-228.

Engquist, B., & Majda, A. (1977). Absorbing boundary conditions for numerical simulation of waves. *Proceedings of the National Academy of Sciences, 74*(5), 1765-1766.

Fang, Y., Xi, X.-L., Wu, J.-M., Liu, J.-F., & Pu, Y.-R. (2016). A JE collocated WLP-FDTD model of wave propagation in isotropic cold plasma. *IEEE Transactions on Microwave Theory and Techniques, 64*(7), 1957-1965.

Forbes, J. M. (1981). The equatorial electrojet. *Reviews of Geophysics, 19*(3), 469-504. doi: 10.1029/RG019i003p00469

Forbes, J. M., Zhang, X., Palo, S., Russell, J., Mertens, C. J., & Mlynczak, M. (2008). Tidal variability in the ionospheric dynamo region. *Journal of Geophysical Research: Space Physics, 113*(A2), n/a-n/a. doi: 10.1029/2007ja012737

Golubkov, G., Golubkov, M., Ivanov, G., Bychkov, V., & Nikitin, A. (2010). The Atmosphere and Ionosphere: Dynamics, Processes and Monitoring: by VL Bychkov, GV Golubkov, and AI Nikitin (Springer, New York, 2010).

Gonzalez, W. D., Joselyn, J. A., Kamide, Y., Kroehl, H. W., Rostoker, G., Tsurutani, B. T., & Vasyliunas, V. M. (1994). What is a geomagnetic storm? *Journal of Geophysical Research: Space Physics, 99*(A4), 5771-5792. doi: 10.1029/93ja02867

Gosling, J. T., McComas, D. J., Phillips, J. L., & Bame, S. J. (1991). Geomagnetic activity associated with earth passage of interplanetary shock disturbances and coronal mass ejections. *Journal of Geophysical Research: Space Physics, 96*(A5), 7831-7839. doi: 10.1029/91ja00316

Guyer, S., & Can, Z. (2013, 12-14 June 2013). *Solar flare effects on the ionosphere.* Paper presented at the 2013 6th International Conference on Recent Advances in Space Technologies (RAST).

Gwal, A., Jain, S. K., Panda, G., & Gujar, Y. (2011). Study of ionospheric perturbations during strong seismic activity by correlation analysis method. *Asian Journal of Earth Sciences, 4*(4), 214.

Hamzah S.Z., H. M. J. (2018). Effect of Geomagnetic Storms on Fluctuations of Total Electron Content at an Equatorial Station. In A. M. Suparta W., Ismail M. (Ed.), *Space Science and Communication for Sustainability* (pp. 97-107): Springer, Singapore.

Harrison, R. G., Aplin, K., & Rycroft, M. (2010). Atmospheric electricity coupling between earthquake regions and the ionosphere. *Journal of Atmospheric and Solar-Terrestrial Physics, 72*(5), 376-381.

Hasbi, A. M., Mohd Ali, M. A., & Misran, N. (2011). Ionospheric variations before some large earthquakes over Sumatra. *Nat. Hazards Earth Syst. Sci., 11*(2), 597-611. doi: 10.5194/nhess-11-597-2011

Hasbi, A. M., Momani, M. A., Mohd Ali, M. A., Misran, N., Shiokawa, K., Otsuka, Y., & Yumoto, K. (2009). Ionospheric and geomagnetic disturbances during the 2005 Sumatran earthquakes. *Journal of Atmospheric and Solar-Terrestrial Physics, 71*(17–18), 1992-2005. doi: http://dx.doi.org/10.1016/j.jastp.2009.09.004

Hayakawa, M., Hobara, Y., Yasuda, Y., Yamaguchi, H., Ohta, K., Izutsu, J., & Nakamura, T. (2012). *Possible precursor to the March 11, 2011, Japan earthquake: ionospheric perturbations as seen by subionospheric very low frequency/low frequency propagation* (Vol. 55).

Heki, K., Otsuka, Y., Choosakul, N., Hemmakorn, N., Komolmis, T., & Maruyama, T. (2006). Detection of ruptures of Andaman fault segments in the 2004 great Sumatra earthquake with coseismic ionospheric disturbances. *Journal of Geophysical Research: Solid Earth, 111*(B9).

Ho, Y.-Y., Jhuang, H.-K., Su, Y.-C., & Liu, J.-Y. (2013). Seismo-ionospheric anomalies in total electron content of the GIM and electron density of DEMETER before the 27 February 2010 M8. 8 Chile earthquake. *Advances in Space Research, 51*(12), 2309-2315.

Huang, S. J., & Li, F. (2004). FDTD simulation of electromagnetic propagation in magnetized plasma using Z transforms. *International Journal of Infrared and Millimeter Waves, 25*(5), 815-825.

Ibanga, J., Akpan, A., George, N., Ekanem, A., & George, A. (2017). Unusual ionospheric variations before the strong Auckland Islands, New Zealand earthquake of 30th September, 2007. *NRIAG Journal of Astronomy and Geophysics*.

Itoh, H., Ando, Y., & Hayakawa, M. (2013). Simplified analysis techniques for VLF wave propagation in the earth–ionosphere waveguide. *Electrical Engineering in Japan, 183*(1), 25-31. doi: 10.1002/eej.22302

Jakowski, N., Borries, C., & Wilken, V. (2012). Introducing a disturbance ionosphere index. *Radio Science, 47*(4). doi: doi:10.1029/2011RS004939

Jakowski, N., Wehrenpfennig, A., Heise, S., Reigber, C., Lühr, H., Grunwaldt, L., & Meehan, T. (2002). GPS radio occultation measurements of the ionosphere from CHAMP: Early results. *Geophysical Research Letters, 29*(10), 95-91-95-94.

Janert, P. K. (2010). *Gnuplot in action: understanding data with graphs*: Manning.

Jianxiong, L., Luhong, M., Jinghong, M., & Jing, X. (2009, 3-6 Nov. 2009). *Unsplit-field formulations for the higher-order PML*. Paper presented at the 2009 International Conference on Microwave Technology and Computational Electromagnetics (ICMTCE 2009).

Kaladze, T. D., Tsamalashvili, L. V., & Kaladze, D. T. (2011). Electromagnetic internal gravity waves in the Earth’s ionospheric E-layer. *Physics Letters A, 376*(2), 123-124. doi: https://doi.org/10.1016/j.physleta.2011.10.044

Kane, Y. (1966). Numerical solution of initial boundary value problems involving maxwell's equations in isotropic media. *Antennas and Propagation, IEEE Transactions on, 14*(3), 302-307. doi: 10.1109/tap.1966.1138693

Kathuria, S., Grover, B., Ray, P. C., & Sharma, G. (2017). *Ionospheric TEC Monitoring Using Ground Based GNSS Observations for Earthquake Precursor Studies.* Paper presented at the 79th EAGE Conference and Exhibition 2017.

Kelley, M. C. (2009). *The Earth's Ionosphere: Plasma Physics & Electrodynamics* (Vol. 96): Academic press.

Kherani, E. A., Lognonne, P., Hébert, H., Rolland, L., Astafyeva, E., Occhipinti, G., . . . De Paula, E. (2012). Modelling of the total electronic content and magnetic field anomalies generated by the 2011 Tohoku-Oki tsunami and associated acoustic-gravity waves. *Geophysical Journal International, 191*(3), 1049-1066.

Kherani, E. A., Lognonné, P., Kamath, N., Crespon, F., & Garcia, R. (2009). Response of the ionosphere to the seismic trigerred acoustic waves: electron density and electromagnetic fluctuations. *Geophysical Journal International, 176*(1), 1-13.

Klimenko, M., Klimenko, V., Zakharenkova, I., & Pulinets, S. (2012). Variations of equatorial electrojet as possible seismo-ionospheric precursor at the occurrence of TEC anomalies before strong earthquake. *Advances in Space Research, 49*(3), 509-517.

Kon, S., Nishihashi, M., & Hattori, K. (2011). Ionospheric anomalies possibly associated with M⩾ 6.0 earthquakes in the Japan area during 1998–2010: Case studies and statistical study. *Journal of Asian Earth Sciences, 41*(4), 410-420.

Koshevaya, S., Makarets, N., Grimalsky, V., Kotsarenko, A., & Enríquez, R. P. (2005). Spectrum of the seismic-electromagnetic and acoustic waves caused by seismic and volcano activity. *Natural Hazards and Earth System Science, 5*(2), 203-209.

Kumar, V. V., & Parkinson, M. L. (2017). A global scale picture of ionospheric peak electron density changes during geomagnetic storms. *Space Weather, 15*(4), 637-652. doi: 10.1002/2016sw001573

Laštovička, J. (1996). Effects of geomagnetic storms in the lower ionosphere, middle atmosphere and troposphere. *Journal of Atmospheric and Terrestrial Physics, 58*(7), 831-843. doi: https://doi.org/10.1016/0021-9169(95)00106-9

Leonard, R. S., & Barnes, R. (1965). Observation of ionospheric disturbances following the Alaska earthquake. *Journal of Geophysical Research, 70*(5), 1250-1253.

Lijun, X., Jinjun, M., & Naichang, Y. (2005, 4-7 Dec. 2005). *FDTD method for 2D anisotropic magnetized plasma.* Paper presented at the Microwave Conference Proceedings, 2005. APMC 2005. Asia-Pacific Conference Proceedings.

Lijun, X., & Naichang, Y. (2005). JEC-FDTD for 2-D conducting cylinder coated by anisotropic magnetized plasma. *IEEE Microwave and Wireless Components Letters, 15*(12), 892-894. doi: 10.1109/lmwc.2005.859970

Liu, J., Chen, C., Chen, Y., Yang, W., Oyama, K., & Kuo, K. (2010). A statistical study of ionospheric earthquake precursors monitored by using equatorial ionization anomaly of GPS TEC in Taiwan during 2001–2007. *Journal of Asian Earth Sciences, 39*(1), 76-80.

Liu, J., Chen, Y., Pulinets, S., Tsai, Y., & Chuo, Y. (2000). Seismo-ionospheric signatures prior to M≥ 6.0 Taiwan earthquakes. *Geophysical Research Letters, 27*(19), 3113-3116.

Liu, J., Tsai, Y., Chen, S., Lee, C., Chen, Y., Yen, H., . . . Liu, C. (2006). Giant ionospheric disturbances excited by the M9. 3 Sumatra earthquake of 26 December 2004. *Geophysical Research Letters, 33*(2).

Liu, S., Liu, M., & Hong, W. (2008). Modified piecewise linear current density recursive convolution finite-difference time-domain method for anisotropic magnetised plasmas. *IET microwaves, antennas & propagation, 2*(7), 677-685.

Liu, S., Mo, J., & Yuan, N. (2004). Piecewise linear current density recursive convolution FDTD implementation for anisotropic magnetized plasmas. *IEEE Microwave and Wireless Components Letters, 14*(5), 222-224.

Maruyama, T., Tsugawa, T., Kato, H., Ishii, M., & Nishioka, M. (2012). Rayleigh wave signature in ionograms induced by strong earthquakes. *Journal of Geophysical Research: Space Physics, 117*(A8).

Maruyama, T., Yusupov, K., & Akchurin, A. (2016). Ionosonde tracking of infrasound wavefronts in the thermosphere launched by seismic waves after the 2010 M8. 8 Chile earthquake. *Journal of Geophysical Research: Space Physics, 121*(3), 2683-2692.

Miklavčić, I., Radolić, V., Vuković, B., Poje, M., Varga, M., Stanić, D., & Planinić, J. (2008). Radon anomaly in soil gas as an earthquake precursor. *Applied radiation and isotopes, 66*(10), 1459-1466.

Molchanov, O., Fedorov, E., Schekotov, A., Gordeev, E., Chebrov, V., Surkov, V., . . . Biagi, P. F. (2004). Lithosphere-atmosphere-ionosphere coupling as governing mechanism for preseismic short-term events in atmosphere and ionosphere. *Nat. Hazards Earth Syst. Sci., 4*(5/6), 757-767. doi: 10.5194/nhess-4-757-2004

Mounirh, K., Adraoui, S. E., Charif, M., Yaich, M. I., & Khalladi, M. (2015). Modeling of anisotropic magnetized plasma media using PLCDRC-TLM method. *Optik - International Journal for Light and Electron Optics, 126*(15), 1479-1482. doi: https://doi.org/10.1016/j.ijleo.2015.04.032

Mur, G. (1981). Absorbing boundary conditions for the finite-difference approximation of the time-domain electromagnetic-field equations. *Electromagnetic Compatibility, IEEE Transactions on*(4), 377-382.

Naidu, P. P., Latha, T. M., Rao, D. M., & Devi, M. I. (2017). Anomalous behavior of the ionosphere before strong earthquakes. *Indian Journal of Physics, 91*(12), 1467-1476.

Nguyen, B. T., Furse, C., & Simpson, J. J. (2015). A 3-D stochastic FDTD model of electromagnetic wave propagation in magnetized ionosphere plasma. *IEEE transactions on antennas and propagation, 63*(1), 304-313.

Nickisch, L. J., & Franke, P. M. (1992). Finite-difference time-domain solution of Maxwell's equations for the dispersive ionosphere. *Antennas and Propagation Magazine, IEEE, 34*(5), 33-39. doi: 10.1109/74.163808

Nicolet, M. (1953). The collision frequency of electrons in the ionosphere. *Journal of Atmospheric and Terrestrial Physics, 3*(4), 200-211.

Ondoh, T. (2009). Investigation of precursory phenomena in the ionosphere, atmosphere and groundwater before large earthquakes of M>6.5. *Advances in Space Research, 43*(2), 214-223. doi: https://doi.org/10.1016/j.asr.2008.04.003
Ono, Y., Ida, Y., Kasahara, Y., Hobara, Y., Hayakawa, M., Rozhnoi, A., . . . Ohta, K. (2012). *Ionospheric perturbations associated with two huge earthquakes in Japan, using principal component analysis for multiple subionospheric VLF/LF propagation paths* (Vol. 55).
Oyama, K.-I., Devi, M., Ryu, K., Chen, C., Liu, J., Liu, H., . . . Kodama, T. (2016). Modifications of the ionosphere prior to large earthquakes: report from the Ionosphere Precursor Study Group. *Geoscience Letters, 3*(1), 1.
Polekh, N., Zolotukhina, N., Kurkin, V., Zherebtsov, G., Shi, J., Wang, G., & Wang, Z. (2017). Dynamics of ionospheric disturbances during the 17–19 March 2015 geomagnetic storm over East Asia. *Advances in Space Research, 60*(11), 2464-2476. doi: https://doi.org/10.1016/j.asr.2017.09.030
Potirakis, S. M., Contoyiannis, Y., Asano, T., & Hayakawa, M. (2018). Intermittency-induced criticality in the lower ionosphere prior to the 2016 Kumamoto earthquakes as embedded in the VLF propagation data observed at multiple stations. *Tectonophysics, 722*, 422-431.
Pulinets, S. (2004). Ionospheric precursors of earthquakes; recent advances in theory and practical applications. *Terrestrial Atmospheric and Oceanic Sciences, 15*(3), 413-436.
Pulinets, S., & Boyarchuk, K. (2004). *Ionospheric precursors of earthquakes*: Springer Science & Business Media.
Pulinets, S. A., & Legen'ka, A. D. (2003). Spatial–Temporal Characteristics of Large Scale Disturbances of Electron Density Observed in the Ionospheric F-Region before Strong Earthquakes. *Cosmic Research, 41*(3), 221-230. doi: 10.1023/a:1024046814173
Pundhir, D., Singh, B., Singh, O., & Gupta, S. K. (2017). A morphological study of low latitude ionosphere and its implication in identifying earthquake precursors. *J. Ind. Geophys. Union (May 2017), 21*(3), 214-222.
Qing, C., Katsurai, M., & Aoyagi, P. H. (1998). An FDTD formulation for dispersive media using a current density. *Antennas and Propagation, IEEE Transactions on, 46*(11), 1739-1746. doi: 10.1109/8.736632
Rees, D. (1995). Observations and modelling of ionospheric and thermospheric disturbances during major geomagnetic storms: a review. *Journal of Atmospheric and Terrestrial Physics, 57*(12), 1433-1457.
Rickard, Y. S., & Georgieva, N. K. (2003). Problem-independent enhancement of PML ABC for the FDTD method. *IEEE transactions on antennas and propagation, 51*(10), 3002-3006. doi: 10.1109/tap.2003.818000
Roh, Y.-S. (2013). Reconstruction of the Electron Density Profile in O-mode Ultrashort Pulse Reflectometry using a Two-dimensional Finite Difference Time Domain. *Journal of the Korean Institute of Illuminating and Electrical Installation Engineers, 27*(7), 52-58.
Rostoker, G. (1972). Geomagnetic indices. *Reviews of Geophysics, 10*(4), 935-950.
Row, R. V. (1966). Evidence of long-period acoustic-gravity waves launched into the F region by the Alaskan earthquake of March 28, 1964. *Journal of Geophysical Research, 71*(1), 343-345.
Ryu, K., Oyama, K.-I., Bankov, L., Chen, C.-H., Devi, M., Liu, H., & Liu, J.-Y. (2016). Precursory enhancement of EIA in the morning sector: Contribution

from mid-latitude large earthquakes in the north-east Asian region. *Advances in Space Research, 57*(1), 268-280.

Samimi, A., & Simpson, J. J. (2015). An efficient 3-D FDTD model of electromagnetic wave propagation in magnetized plasma. *IEEE transactions on antennas and propagation, 63*(1), 269-279.

Santosa, H., Hobara, Y., & Munir, A. (2014). Modeling and Numerical Analysis of Seismo-Electromagnetics Perturbation Using FDTD Method. *International Journal on Electrical Engineering and Informatics, 6*(2), 255.

Sarkar, S., Choudhary, S., Sonakia, A., Vishwakarma, A., & Gwal, A. (2012). Ionospheric anomalies associated with the Haiti earthquake of 12 January 2010 observed by DEMETER satellite. *Natural Hazards and Earth System Sciences, 12*(3), 671.

Schmidtke, G. (1976). EUV indices for solar-terrestrial relations. *Geophysical Research Letters, 3*(10), 573-576.

Schunk, R., & Nagy, A. (2009). *Ionospheres: physics, plasma physics, and chemistry*: Cambridge university press.

Sergeenko, N. P., Rogova, M. V., & Sazanov, A. V. (2009, 28-30 April 2009). *Seismic traveling ionosphere irregularities at F2-region in time of heliogeophysic disturbances on data of distance sounding.* Paper presented at the The Institution of Engineering and Technology 11th International Conference on Ionospheric radio Systems and Techniques (IRST 2009).

Shaobin, L., Naichang, Y., & Jinjun, M. (2003). A novel FDTD formulation for dispersive media. *Microwave and Wireless Components Letters, IEEE, 13*(5), 187-189. doi: 10.1109/lmwc.2003.811663

Shinagawa, H., Iyemori, T., Saito, S., & Maruyama, T. (2007). A numerical simulation of ionospheric and atmospheric variations associated with the Sumatra earthquake on December 26, 2004. *Earth, planets and space, 59*(9), 1015-1026.

Shubitidze, P., Jobava, R., Beria, R., Shamatava, I., Zaridze, R., & Karkashadze, D. (1999, 1999). *Application of FDTD to dispersive media.* Paper presented at the DIPED - 99. Direct and Inverse Problems of Electromagnetic and Acoustic Wave Theory. Proceedings of 4th International Seminar/Workshop (IEEE Cat. No.99TH8402).

Shubitidze, P., Jobava, R., Beria, R., Shamatava, I., Zaridze, R., & Karkashadze, D. (1999). *Application of FDTD to dispersive media.* Paper presented at the Direct and Inverse Problems of Electromagnetic and Acoustic Wave Theory, 1999. Proceedings of IVth International Seminar/Workshop.

Simões, F., Rycroft, M., Renno, N., Yair, Y., Aplin, K., & Takahashi, Y. (2008). Schumann resonances as a means of investigating the electromagnetic environment in the solar system. *Space Science Reviews, 137*(1-4), 455-471.

Simpson, J. J., & Taflove, A. (2005). Electrokinetic effect of the Loma Prieta earthquake calculated by an entire-Earth FDTD solution of Maxwell's equations. *Geophysical Research Letters, 32*(9), n/a-n/a. doi: 10.1029/2005gl022601

Simpson, J. J., & Taflove, A. (2006a). ELF Radar System Proposed for Localized D-Region Ionospheric Anomalies. *Geoscience and Remote Sensing Letters, IEEE, 3*(4), 500-503. doi: 10.1109/lgrs.2006.878443

Simpson, J. J., & Taflove, A. (2006b). A novel ELF radar for major oil deposits. *Geoscience and Remote Sensing Letters, IEEE, 3*(1), 36-39. doi: 10.1109/lgrs.2005.856118

Simpson, J. J., & Taflove, A. (2007). A Review of Progress in FDTD Maxwell's Equations Modeling of Impulsive Subionospheric Propagation Below 300 kHz. *Antennas and Propagation, IEEE Transactions on, 55*(6), 1582-1590. doi: 10.1109/tap.2007.897138

Singh, D., Singh, B., & Pundhir, D. (2017). Ionospheric perturbations due to earthquakes as determined from VLF and GPS-TEC data analysis at Agra, India. *Advances in Space Research*.

Soriano, A., Navarro, E., Morente, J., & Portí, J. (2007). A numerical study of the Schumann resonances in Mars with the FDTD method. *Journal of Geophysical Research: Space Physics (1978–2012), 112*(A6).

Sorokin, V., Yashchenko, A., & Hayakawa, M. (2007). Electric field perturbation caused by an increase in conductivity related to seismicity-induced atmospheric radioactivity growth. *Russian Journal of Physical Chemistry B, 1*(6), 644-648.

Sullivan, D. M. (1992). Frequency-dependent FDTD methods using Z transforms. *IEEE transactions on antennas and propagation, 40*(10), 1223-1230.

Sullivan, D. M. (1996). A simplified PML for use with the FDTD method. *IEEE Microwave and Guided Wave Letters, 6*(2), 97. doi: 10.1109/75.482001

Sun, Y. Y., Liu, J. Y., Lin, C. Y., Tsai, H. F., Chang, L. C., Chen, C. Y., & Chen, C. H. (2016). Ionospheric F2 region perturbed by the 25 April 2015 Nepal earthquake. *Journal of Geophysical Research: Space Physics*.

Taflove, A. (1980). Application of the finite-difference time-domain method to sinusoidal steady-state electromagnetic-penetration problems. *Electromagnetic Compatibility, IEEE Transactions on*(3), 191-202.

Taflove, A., & Hagness, S. C. (2005). *Computational electrodynamics*: Artech house.

Takayama, Y., & Klaus, W. (2002). Reinterpretation of the auxiliary differential equation method for FDTD. *IEEE Microwave and Wireless Components Letters, 12*(3), 102-104. doi: 10.1109/7260.989865

Tao, D., Cao, J., Battiston, R., Li, L., Ma, Y., Liu, W., . . . Dunlop, M. W. (2017). *Seismo-ionospheric anomalies in ionospheric TEC and plasma density before the 17 July 2006 M7. 7 south of Java earthquake.* Paper presented at the Annales Geophysicae.

Tapping, K. (2013). The 10.7 cm solar radio flux (F10. 7). *Space Weather, 11*(7), 394-406.

Thevenot, M., Berenger, J.-P., MonediÈre, T., & Jecko, F. (1999). A FDTD scheme for the computation of VLF-LF propagation in the anisotropic earth-ionosphere waveguide. *Annales Des Télécommunications, 54*(5-6), 297-310. doi: 10.1007/bf02995540

Thomson, N. (1993). Experimental daytime VLF ionospheric parameters. *Journal of Atmospheric and Terrestrial Physics, 55*(2), 173-184.

Titheridge, J. E. (1972). Determination of ionospheric electron content from the Faraday rotation of geostationary satellite signals. *Planetary and Space Science, 20*(3), 353-369. doi: https://doi.org/10.1016/0032-0633(72)90034-7

Vita, A. N., Putra, S. Y. S., Subakti, H., & Muslim, B. (2017). *Identification of ionospheric GPS TEC anomalies prior to earthquake in Sumatra between 2007-2012 using correlation technique.* Paper presented at the AIP Conference Proceedings.

Ware, R., Rocken, C., Solheim, F., Exner, M., Schreiner, W., Anthes, R., . . . Sokolovskiy, S. (1996). GPS sounding of the atmosphere from low Earth orbit: Preliminary results. *Bulletin of the American Meteorological Society, 77*(1), 19-40.

Weedon, W. H., & Rappaport, C. M. (1997). A general method for FDTD modeling of wave propagation in arbitrary frequency-dispersive media. *IEEE transactions on antennas and propagation, 45*(3), 401-410. doi: 10.1109/8.558655

Wenyi, H., & Cummer, S. A. (2006). An FDTD model for low and high altitude lightning-generated EM fields. *Antennas and Propagation, IEEE Transactions on, 54*(5), 1513-1522. doi: 10.1109/tap.2006.874336

Whitehead, J. (1961). The formation of the sporadic-E-layer in the temperate zones. *Journal of Atmospheric and Terrestrial Physics, 20*(1), 49-58.

Wiesemann, K. (2014). A Short Introduction to Plasma Physics. *arXiv preprint arXiv:1404.0509*.

Wu, C.-C., Liou, K., Shan, S.-J., & Tseng, C. L. (2008). Variation of ionospheric total electron content in Taiwan region of the equatorial anomaly from 1994 to 2003. *Advances in Space Research, 41*(4), 611-616. doi: http://dx.doi.org/10.1016/j.asr.2007.06.013

Yang, L., Xie, Y., & Yu, P. (2011). Study of bandgap characteristics of 2D magnetoplasma photonic crystal by using M-FDTD method. *Microwave and Optical Technology Letters, 53*(8), 1778-1784. doi: 10.1002/mop.26143

Yu, Y., & Simpson, J. J. (2009). *A new 3-D FDTD model of magnetized cold plasma for modeling electromagnetic wave propagation in the earth-ionosphere waveguide.* Paper presented at the Antennas and Propagation Society International Symposium, 2009. APSURSI'09. IEEE.

Zakharenkova, I., Krankowski, A., & Shagimuratov, I. (2006). Modification of the low-latitude ionosphere before the 26 December 2004 Indonesian earthquake. *Natural Hazards and Earth System Science, 6*(5), 817-823.

Zeng, Z. C., Zhang, B., Fang, G. Y., Wang, D. F., & Yin, H. J. (2009). An analysis of ionospheric variations before the Wenchuan earthquake with DEMETER data. *Chinese Journal of Geophysics, 52*(1), 13-22.

Zhao, S., Zhang, X., Zhao, Z., & Shen, X. (2014). The numerical simulation on ionospheric perturbations in electric field before large earthquakes. *Ann. Geophys, 32*, 1487-1493.

Zhou, Y., Wang, Y., & Cao, Q. (2015). *2-D local ionosphere propagation model using an implicit ADE FDTD method combined with a layer smoothing technique.* Paper presented at the Microwave Conference (APMC), 2015 Asia-Pacific.

Zolesi, B., & Cander, L. R. (2014). *Ionospheric prediction and forecasting*: Springer.

APPENDIX

The FDTD codes using Fortran90.

```
!//////////////////////////////////////////////////////////////////////////////////////////
!2d fdtd tmz
!pml
!anisotropic
!created by Siti Harwani Yusoff
!//////////////////////////////////////////////////////////////////////////////////////////
module data_module
implicit none

real,parameter     :: f0 = 30.0e3    !original
!real,parameter     :: f0 = 3.0e3
real,parameter     :: A0= 10.0
real,parameter     :: c = 3.e8
real,parameter     :: pi = 3.14159265
real,parameter     :: eps0 = 8.8e-12,miu0 =  4*pi*1e-7
real,parameter     :: lamda = c/f0, omega = 2*pi*f0
real,parameter     :: dx = lamda/10,dy = dx
real               :: dt
real               :: ca, cb

integer            :: g_order
integer            :: i,j,h,x,y
integer            :: n,hp,k,nx,ny
integer,parameter  :: nt = 2000
integer, parameter :: PML = 50
!integer,parameter  :: is = 1,ie = 120,js = 1,je = 120
integer,parameter  :: is = 1,ie = 600,js = 1,je = 120
!integer,parameter  :: is = 0,ie = 620,js = 0,je = 140
!integer,parameter  :: is = 1,ie = 50,js = 1,je = 11      !model size, f = 30kHz
!integer,parameter  :: xl1 = is+5,xl2 = ie-5,yl1 = js+5,yl2 = je-5
integer,parameter  :: ic = ie/2,jc = je/2
real               :: miur,epsr,refcoef,sigmamax

real               :: beta,b0,wb
!real              :: b0(is:ie,js:je)
real               :: wp2(is:ie,js:je),wp(is:ie,js:je),ve(is:ie,js:je)
real               :: Ne(is:ie,js:je)
real               :: Ga(is:ie,js:je),Gb(is:ie,js:je)
real,parameter     :: ec = 1.602e-19        ! electron charge
real,parameter     :: me = 9.109e-31        ! electron mass

real,dimension(-2000:2000,-2000:2000) :: Ez,Hx,Hy
real,dimension(2000,2000)             :: Jz
real,dimension(-2000:2000,-2000:2000) :: Cax,Cbx,Dax,Dbx, Day, Dby
real,dimension(-2000:2000,-2000:2000) :: miu,eps
real,dimension(-2000:2000,-2000:2000) :: boundf1, boundf2, boundf3, boundf4
real,dimension(-2000:2000,-2000:2000) :: epsHx,epsHy
!real,dimension(-2000:2000) ::sigmax,sigmay,sigmatx, sigmaty
real,dimension(-2000:2000,-2000:2000) ::sigmax,sigmay,sigmatx, sigmaty
 double precision   :: n_core, n_clad,ny0,r,w0,triw,xshift,nxshift,Rf,angle
```

```
end module data_module
!/////////////////////////////////////////////////////////////////////////////////////////////////
subroutine modeltmz
use data_module
implicit none

character(len=20)               :: filename

print*, 'see me?'

 dt = dx/(2*c)
 print *, 'dx=',dx,'dt=',dt

 !pml thickness
 n_core = 2.915d0
 n_clad = 1.0d0
 ny0 = 1d-6/dy+PML
 r = 3D-6
 w0 = 0.3D-6
 triw = 0.5D-6
 xshift = 0 !-W0/2D0 !2.6D-6
 nxshift = xshift/dx

!initialize Ez, Hx,Hy to zero at t=0
do i = 1,ie
 do j = 1,je
   Hx(i,j) = 0.0
   Hy(i,j) = 0.0
   Ez(i,j) = 0.0
   Jz(i,j) = 0.0
 end do
end do

! do j = 1,je
!   sigmay(j) = 0.0
! end do

! do i = 1,ie
!   sigmax(i) = 0.0
! end do

!**************************
! medium 1 properties
 miur = 1.0
 epsr = 1.0

! initialize permittivity and permeability
 do i = is,ie
  do j = js,je
   eps(i,j) = epsr*eps0
   miu(i,j) = miur*miu0
  end do
 end do
```

```
!****************************************
 i = is
 x = i*dx+dx/2D0
  do while(i.LE.ie-1)
    j = js
    y = j*dy
    do while(j.LE.je)
      epsHx(i,j) = eps0*n_clad**2
      j = j+1
      y = j*dy
    end do

   i = i+1
   x = i*dx+dx/2D0
  end do

 i = is
 x = i*dx
   do while(i.LE.ie)
    j = js
    y = j*dy+dy/2D0
      do while(j.LE.je-1)
             epsHy(i,j) = eps0*n_clad**2
             j = j+1
             y = j*dy+dy/2D0
      end do
    i = i+1
    x = i*dx
   end do

!*******

 h = 4 !N
 angle = 1*pi/180
 Rf = 5e-5
 sigmamax = -(h+1)*log(Rf)*c*eps0/(2.0D0*(PML*dx))

  !i = ie
 do i = is,ie
  do j = js,je
    sigmax(i,j) = 0D0
     if(i.LT.is+PML)then
      sigmax(i,j) = sigmamax*(real(i-(is+PML))/real(PML))**h
     else if(i.GT.ie-PML)then
      sigmax(i,j) = sigmamax*(real(i-(ie-PML))/real(PML))**h
     end if

  end do
 end do

  !j = je
 do j = js,je
  do i = is,ie
    sigmay(i,j) = 0D0
```

```
    if(j.LT.js+PML)then
     sigmay(i,j) = sigmamax*(real(j-(js+PML))/real(PML))**h
    else if(j.GT.je-PML)then
     sigmay(i,j) = sigmamax*(real(j-(je-PML))/real(PML))**h
    end if
 end do
end do

!_________

do i = is,ie
 do j = js,je
   sigmay(i,j) = 0D0
    if(i.LT.is+PML)then
     sigmay(i,j) = sigmamax*(real(i-(is+PML))/real(PML))**h
    else if(i.GT.ie-PML)then
     sigmay(i,j) = sigmamax*(real(i-(ie-PML))/real(PML))**h
    end if
   !i = i+1
  !print *,i,j, 'sigmax=',sigmax(i,j)
  !end do
 end do
end do

 !j = je
do j = js,je
 do i = is,ie
   sigmax(i,j) = 0D0
    if(j.LT.js+PML)then
     sigmax(i,j) = sigmamax*(real(j-(js+PML))/real(PML))**h
    else if(j.GT.je-PML)then
     sigmax(i,j) = sigmamax*(real(j-(je-PML))/real(PML))**h
    end if
   !j = j+1
  !end do
  !print *,i,j, 'sigmax=',sigmax(i,j)
 end do
end do

!**************************************************************

do i = is,ie
 do j = js,je
  sigmatx(i,j) = (sigmax(i,j)*miu(i,j))/eps(i,j)
 end do
end do

do i = is,ie
 do j = js,je
  sigmaty(i,j) = (sigmay(i,j)*miu(i,j))/eps(i,j)
 end do
end do

! initialize electric conductivity & magnetic conductivity
do i = is,ie-1
```

```
 do j = js,je-1

   Cax(i,j) = ((eps0-0.5*dt*sigmax(i,j)))/(eps0+0.5*dt*sigmax(i,j))
   Cbx(i,j) = (dt/dx)/(eps0+0.5*dt*sigmax(i,j))
   Dax(i,j) = ((miu0-0.5*dt*sigmatx(i,j))/(miu0+0.5*dt*sigmatx(i,j)))
   Dbx(i,j) = (dt/dx)/(miu0+0.5*dt*sigmatx(i,j))
   Day(i,j) = ((miu0-0.5*dt*sigmaty(i,j))/(miu0+0.5*dt*sigmaty(i,j)))
   Dby(i,j) = (dt/dy)/(miu0+0.5*dt*sigmaty(i,j))

   !print*, i,j,'Cax(i,j)=',Cax(i,j),'Cbx(i,j)=',Cbx(i,j),'Dax(i,j)=',Dax(i,j),'Dbx(i,j)=',Dbx(i,j)
  end do
 end do


!**********************************************************************
!medium's properties
!**********************************************************************

!! daytime
 hp = 72
 beta = 0.3

!calculate parameters

 i = ie
 do j = 1,je

   Ne(1,j) = (1.43e7*exp(-0.15*hp)*exp((beta-0.15)*(j-hp)))*1e+6
   print *, j,Ne(1,j)

   !Ne(1,j) = 0.0

!calculate parameters
   wp(1,j) = (((ec**2*Ne(1,j))/(eps0*me))**0.5)/(2*pi)
   wp2(1,j) = wp(1,j)**2                ! plasma frequency
   !wp2(1,j) = 0.0
   ve(1,j) = 1.816e11*exp(-0.15*j)       ! collision frequency(Hz)
   !ve(1,j) = 0.0


   Ga(i,j) = exp(-ve(1,j)*dt)
   Gb(i,j) = eps0*wp2(1,j)*dt*exp(-ve(1,j)*dt/2)
   !Gb(i,j) = ((Ne(1,j)*(ec**2)*dt)/me)
   !print *,'Ga(i,j)=',Ga(i,j), 'Gb=',Gb(i,j),'wp2(1,j)=',wp2(1,j)

 end do


!**********************************************************************
***
!time steps begin
!**********************************************************************

 do n = 1,nt
```

```
  write (filename, "('data',I5.5,'.dat')") n
  open (unit=130,file=filename)


!initiate sinusoidal wavepulse

  Ez(is+1,js+1) = A0*sin(2*pi*f0*n*dt)
  !print *, 'Ez(3,3)=',Ez(3,3)

!************************************************************************
***
! calculate electric-field

  do i = is+1,ie-1
   do j = js+1,je-1
    Ez(i,j) = Cax(i,j)*(Ez(i,j)-Jz(i,j)) + Cbx(i,j)*(Hy(i,j)-Hy(i-1,j) - Hx(i,j) + Hx(i,j-1))
    write (130,*) i,j,Ez(i,j)
    if (j == je-1) write (130,*) ' '
    !print *,'i=',i,'j=',j,'Jz(i,j)=',Jz(i,j)
   end do
  end do

!************************************************************************
***
! calculate current density

  do i = is+1,ie-1
   do j = js+1,je-1

     Jz(i,j) = Ga(ie,j)*Jz(i,j) + Gb(ie,j)*Ez(i,j)
     !write (130,*) i,j,Jz(i,j)
     !if (j == je-1) write (130,*) ' '
    !print *,'i=',i,'j=',j,'Jz(i,j)=',Jz(i,j)
    !print *,'i=',i,'j=',j,'Gb(ie,j)=',Gb(ie,j)
   end do
  end do


!************************************************************************
***
! calculate magneticc-field

 do j = js,je-1
  do i = is,ie-1
   Hx(i,j) = Dax(i,j)*Hx(i,j) - Dbx(i,j)*(Ez(i,j+1)-Ez(i,j))
   !print *,'i=',i,'j=',j,'Hx(i,j)=',Hx(i,j)
  end do
 end do

 do j = js,je-1
  do i = is,ie-1
   Hy(i,j) = Day(i,j)*Hy(i,j) + Dby(i,j)*(Ez(i+1,j)-Ez(i,j))
  end do
 end do
```

```
 close (unit = 130)
! close (unit = 120)

 end do !n


end subroutine modeltmz



!/////////////////////////////////////////////////////////////////////////////////////////////////
```

LIST OF PUBLICATIONS

Journal article

S. H. Md. Yusoff, H. S. Lim, T. L. Yoon (2017), Observation On Vertical Electron Density Profile In E-Layer Ionosphere Before Indian-Ocean Earthquake On December 2004 Using Champ Satellite, Journal of the Earth and Space Physics, 42/4:4, 43-47.

Chapter in an edited book

Md Yusoff., SH. (2017). Ionosphere Perturbation Modelling in Equatorial Region By Electromagnetic Wave Propagation. In *Advances in Aerospace Science and Technology* (pp. 211-234). Nova Science Publications.